

**MASTER**

**Penetrated circular hollow section X-joints in steel**

Nijenhuis, Marc

*Award date:*  
2021

[Link to publication](#)

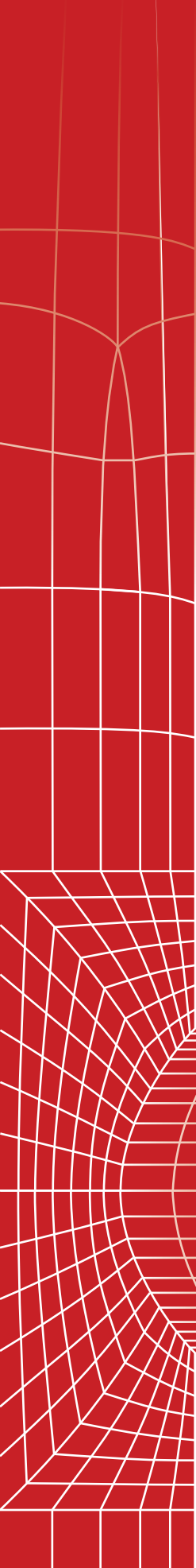
**Disclaimer**

This document contains a student thesis (bachelor's or master's), as authored by a student at Eindhoven University of Technology. Student theses are made available in the TU/e repository upon obtaining the required degree. The grade received is not published on the document as presented in the repository. The required complexity or quality of research of student theses may vary by program, and the required minimum study period may vary in duration.

**General rights**

Copyright and moral rights for the publications made accessible in the public portal are retained by the authors and/or other copyright owners and it is a condition of accessing publications that users recognise and abide by the legal requirements associated with these rights.

- Users may download and print one copy of any publication from the public portal for the purpose of private study or research.
- You may not further distribute the material or use it for any profit-making activity or commercial gain



# Penetrated Circular Hollow Section X-joints in Steel

M. Nijenhuis

29-01-2021



# Penetrated Circular Hollow Section X-joints in Steel

## Master's Thesis

Date January 29, 2021

## Educational institution

University Eindhoven University of Technology  
Department Built Environment  
Master program Architecture, Building and Planning  
Unit Structural Engineering and Design  
Chair Steel and Aluminum Structures (SAS)

## Author

Name Marc Nijenhuis  
Student number 1264311  
Email m.nijenhuis@student.tue.nl  
nijenhuis1995@gmail.com

## Graduation supervision committee

Chairman	Prof. ir.	H.H. (Bert) Snijder	(TU/e)
2 <sup>nd</sup> supervisor	Dr. ir.	P.A. (Paul) Teeuwen	(W+B)
3 <sup>rd</sup> supervisor	Dr. ir.	H. (Hèrm) Hofmeyer	(TU/e)
4 <sup>th</sup> supervisor	Dr. ir.	D. (Davide) Leonetti	(TU/e)





## ABSTRACT

Steel circular hollow sections (CHS) are widely used for structures in the civil industry, such as mooring and off-shore structures. A common joint in these structures is the X-joint, in which two coaxial braces are connected to either side of the chord, the main structural element. In most cases, the braces are welded to the chord, without penetrating it at the intersection. However, in civil structures, another type of X-joint for circular hollow sections is frequently used. These joints are referred to as penetrated CHS X-joints in which the brace passes through the chord. Although penetrated CHS X-joints are frequently applied by Dutch engineering firms in civil structures and extensive guidelines and rules are available for non-penetrated X-joints, there are no specific design rules available for penetrated CHS X-joints and available research into these joints is limited.

This research focused on gaining insight into and predicting the behavior of penetrated CHS X-joints. Since very limited research has been done into this type of CHS X-joints, literature and existing research into a comparable penetrated connection, plate-to-structural hollow sections (SHS), has been studied. Analogous to the penetrated CHS X-joints and their non-penetrated equivalents, the behavior of through plate joints is compared with their corresponding branched plate equivalents. It has been found that the former has a capacity of more than double till even three times the capacity of their equivalent branched plate joints.

A similar increase in capacity is expected for penetrated CHS X-joints. To gain insight into the structural behavior of the penetrated joints and the possible differences with respect to their non-penetrated equivalents, a parameter study consisting of 388 finite element (FE) analyses is conducted in which applied loads and geometrical dimensions are varied. For this purpose a FE model is created using a python script. The script is imported in the FE software ABAQUS, which is used to perform a geometrical and material non-linear FE analysis. An elastic-plastic material model with linear strain hardening, as provided in Eurocode (EC) EN 1993-1-5 is adopted.

In the parameter study for several load cases the geometrical parameters, the brace width-to-chord width ratio  $\beta$ , the chord diameter to thickness ratio  $2\gamma$ , and the brace diameter to thickness ratio  $2\delta$  are varied within a certain range that is common for applications in civil structures. The parameter study is performed for penetrated, as well as for non-penetrated, CHS X-joints. Initially only the boundary values of the geometrical parameters are simulated to identify the critical areas for which the current set of design rules insufficiently describe the behavior of the joint and the capacity of the penetrated CHS X-joint is underestimated significantly. Based on these results, additional parameter configurations have been evaluated using finite element analysis (FEA). The parameter study is performed for the load cases "Double-sided compression and tension ( $F_x$ )", "Single-sided compression and tension ( $F_x$ )", "Bending moment about the Y-axis ( $M_y$ )", "Bending moment about the Z-axis ( $M_z$ )", "Shear  $F_y$  (chord bending moment)", and "Shear  $F_z$  (chord torsional moment)".

It appears that for several load cases, the design rules for non-penetrated CHS X-joints, as provided in the EN 1993-1-8, do not suffice for penetrated CHS X-joints in those critical areas. The critical areas are identified and evaluated and based on the FEA results, improved and new design rules for penetrated joints are created for the load cases for which this is required: "Single-sided compression and tension ( $F_x$ )", "Shear in the Y-direction ( $F_y$ )", and "Shear in the Z-direction ( $F_z$ ). For the load cases "Double-sided compression and tension ( $F_x$ )" and "Bending moment about the Y- ( $M_y$ ) and Z-axis ( $M_z$ )" the behavior can be approximated accurately with the basic cross-section design rules from the EC, and therefore, the EC design rules for non-penetrated joint failures should for penetrated geometries in these load cases, be omitted while calculating the governing failure mechanisms and the corresponding plastic design resistances. The new sets of design rules for penetrated CHS X-joints are evaluated and the behavior of penetrated CHS X-joints subjected to the aforementioned failure mechanisms can be described well. Additionally, the application of the new design rules for penetrated CHS X-joints is validated for combined load cases. The research is concluded with a clear and uniform set of design rules that can be used for the calculation of penetrated CHS X-joints.



## PREFACE

---

The presented thesis is the result of my graduation research on penetrated circular hollow section X-joints in steel, to complete the master Architecture, Building and Planning with a specialization in Structural Engineering and Design at the Eindhoven University of Technology.

I would like to express my thanks and appreciation to the members of my graduation supervision committee, Prof. ir. Bert Snijder, Professor of Steel Structures at the Eindhoven University of Technology, Dr. ir. Paul Teeuwen, Structural Engineer at Witteveen+Bos, Dr. ir. Hèrm Hofmeyer, Associate Professor of Applied Mechanics at the Eindhoven University of Technology, and Dr. ir. Davide Leonetti, Assistant Professor of in Steel Structures and Structural Health Monitoring at the Eindhoven University of Technology. I am grateful for their time, guidance and support over the past year. Special thanks to Bert Snijder, who, despite the very busy period due to corona, was always willing to help and schedule an extra digital meeting, and to Paul Teeuwen as an external supervisor, for providing the research topic. I wish to express my gratitude to my supervisors for contributing to the successful completion of this master thesis.

Furthermore, I would like to thank the other graduation members from our graduation studio, with whom I have participated in the graduation meetings, which allowed me to learn a lot from their researches as well. Special thanks go to Wim Broeks, Ivo Geurts and Britt Cordewener who were always willing to discuss and spar on a topic and helped me through the difficult choices within the graduation project.

Finally, I would like to thank my family and friends for their support throughout my graduation research.

Marc Nijenhuis

Eindhoven, January 2021



## NOMENCLATURE

---

### ACRONYMS

B bm	brace bending moment
B cs	brace cross-section
C bm	chord bending moment
C ff	chord face failure
C ps	chord punching shear
C tm	chord torsional moment
C T+S	combination of a torsional moment and shear
CHS	circular hollow section
EC	eurocode
FE	finite element
FEA	finite element analysis
FEM	finite element method
NP	non-penetrated
P	penetrated
RR	resistance ratio, which is the ratio between the FEA plastic capacity and the plastic design resistance according to corresponding design rule ( $\chi_{FEA}/\chi_{design\ rule}$ )
SHS	structural hollow section
UC	unity check

### GREEK SYMBOLS

$\alpha$	chord length parameter
$\beta$	chord diameter to brace diameter ratio
$\gamma$	chord diameter to twice the wall thickness ratio
$\gamma_M$	partial safety factor
$\delta$	brace diameter to twice the wall thickness ratio
$\varepsilon$	strain
$\eta$	longitudinal plate depth-to-HSS width ratio
$\theta$	angle between chord and brace member
$\sigma$	stress
$\sigma_p$	stress value excluding the stress due to the components parallel to the chord axis
$\tau$	shear
$\nu$	poisson's ratio

### ROMAN SYMBOLS

$A_v$	shear area
$I_p$	polar moment of inertia
$W_t$	torsional modulus
$f_{\beta;\gamma;\delta}$	factor for ( $\beta$ , $\gamma$ , or $\delta$ )
$k_p$	reduction factor to take into account the compression stress in the chord member
$n_p$	ratio design value to yield strength
$A$	cross sectional area
$E$	elastic modulus
$F$	force
$I$	moment of area
$L$	length
$M$	bending moment
$N$	axial force
$RF$	reaction force

## ROMAN SYMBOLS (CONTINUED)

<i>S</i>	stress
<i>T</i>	torsional
<i>V</i>	shear force
<i>W</i>	section modulus
<i>b</i>	width
<i>d</i>	diameter
<i>e</i>	eccentricity
<i>f</i>	strength
<i>r</i>	radius
<i>t</i>	thickness

## SUPERSCRIPTS

'	effective
---	-----------

## SUBSCRIPTS

0	chord member
1	brace member
<i>Ed</i>	design value
<i>FEA</i>	finite element analysis
<i>N</i>	reduced by the normal force
<i>Rd</i>	design resistance
<i>el</i>	elastic
<i>eng</i>	engineering
<i>i</i>	relevant brace member
<i>pl</i>	plastic
<i>true</i>	true
<i>u</i>	ultimate
<i>x</i>	X-direction
<i>y</i>	Y-direction
<i>y</i>	yield value
<i>z</i>	Z-direction
$\tau$	reduced by shear

# CONTENTS

1	Introduction .....	2
2	Literature study.....	4
2.1	Design rules for hollow section joints.....	4
2.1.1	Failure modes for hollow section joints.....	4
2.1.2	Design resistance .....	5
2.2	Penetrated hollow structural section .....	8
2.2.1	Through plate-to-hollow structural section joint .....	8
2.2.2	Design resistance by deformation limit .....	8
2.2.3	Finite element modeling.....	8
2.2.4	Parametric study .....	10
2.2.5	Conclusions and recommendations .....	10
3	finite element model for CHS X-joints .....	12
3.1	Finite element model .....	12
3.1.1	Geometry.....	12
3.1.2	Material model.....	13
3.1.3	Mesh settings and element types .....	14
3.1.4	Loads and boundary conditions .....	17
3.1.5	Finite element analysis (FEA).....	18
3.1.6	Output.....	18
3.2	Validation of the finite element model .....	20
3.2.1	Experimental test .....	20
3.2.2	FE model .....	22
3.2.3	Results.....	24
3.2.4	Conclusion .....	25
4	Parameter study.....	26
4.1	Parameter study .....	26
4.2	Failure mechanisms.....	27
4.3	Processing results .....	29
4.3.1	Penetrated double-sided compression $\beta$ 0.8 – $2\gamma$ 10 – $2\delta$ 30.....	29
4.3.2	Penetrated single-sided compression $\beta$ 0.2 – $2\gamma$ 50 – $2\delta$ 10.....	30
4.4	Double-sided compression and tension ( $F_x$ ).....	31
4.4.1	Penetrated CHS X-joint FEA results.....	31
4.4.2	Comparison penetrated and non-penetrated results.....	32
4.4.3	Conclusion double-sided compression and tension.....	33
4.5	Single-sided compression and tension ( $F_x$ ).....	33
4.5.1	Penetrated CHS X-joint FEA results.....	33
4.5.2	Comparison penetrated and non-penetrated results.....	33
4.5.3	Conclusion single-sided compression and tension.....	35
4.6	Bending moment about the Y- ( $M_y$ ) and Z- ( $M_z$ ) axis.....	36
4.6.1	Penetrated CHS X-joint FEA results.....	36
4.6.2	Comparison non-penetrated and penetrated results.....	36
4.6.3	Conclusion bending moment about the Y- ( $M_y$ ) and Z- ( $M_z$ ) axis .....	37
4.7	Shear $F_y$ (chord bending moment).....	37
4.7.1	Penetrated CHS X-joint FEA results.....	37
4.7.2	Comparison non-penetrated and penetrated results.....	38
4.7.3	Conclusion shear $F_y$ (chord bending moment) .....	38
4.8	Shear $F_z$ (chord torsional moment).....	39
4.8.1	Penetrated CHS X-joint FEA results.....	39

4.8.2	Comparison non-penetrated and penetrated results .....	40
4.8.3	Conclusion shear $F_z$ (chord torsional moment) .....	40
4.9	Conclusion parameter study .....	41
5	Design rules .....	42
5.1	Introduction .....	42
5.2	Single-sided compression and tension ( $F_x$ ).....	42
5.2.1	Non-penetrated X-joints .....	42
5.2.2	Penetrated CHS X-joints.....	46
5.3	Shear $F_y$ (chord bending moment).....	53
5.3.1	Additional simulations .....	53
5.3.2	Design rule .....	53
5.3.3	Verification of the governing failure mechanism .....	55
5.3.4	Conclusion design rule Shear $F_y$ .....	55
5.4	Shear $F_z$ (chord torsional moment).....	56
5.4.1	Additional simulations .....	56
5.4.2	Design rules .....	56
5.4.3	Verification of the failure mechanisms .....	58
5.4.4	Conclusion design rule shear $F_z$ .....	58
5.5	Combination of load cases .....	59
5.5.1	Introduction.....	59
5.5.2	Combination of Shear $F_y$ and Shear $F_z$ .....	59
5.5.3	Combination of Tension ( $F_x$ ), Shear $F_y$ and Shear $F_z$ .....	61
5.5.4	Conclusion combined load cases.....	62
5.6	Penetrated CHS X-joint design checks .....	63
5.6.1	Introduction.....	63
5.6.2	Penetrated CHS X-joint calculation sheet .....	63
5.6.3	Combination design rule torsional moment and shear .....	65
5.6.4	Case study   Mooring bollard Witteveen+Bos .....	68
5.7	Summary and conclusion design rules .....	70
6	Conclusion & Recommendation.....	74
6.1	Conclusions .....	74
6.2	Recommendations.....	77
7	References.....	80
Appendices .....		A.I
A.	Python script .....	A.I
Appendices B-G (separate document "Appendices B-G")		
B.	Results validation study .....	B.I
C.	FEA results penetrated CHS X-joints .....	C.I
D.	FEA results comparison penetrated – non-penetrated CHS X-joints .....	D.I
E.	Design rule check – combination of forces .....	E.I
F.	Failure mechanism calculation sheet.....	F.I
G.	Calculation sheet – penetrated CHS X-joints.....	G.I





# 1 INTRODUCTION

Steel circular hollow sections (CHS) are widely used for structures in the civil industry, such as mooring and off-shore structures. A common joint in these structures is the CHS X-joint, in which two coaxial braces are connected to either side of the chord, which is the main structural element (with the largest diameter). In most cases, the braces are welded to the chord, without penetrating it at the intersection. However, in civil structures, another type of X-joint for CHS is frequently used. These joints are referred to as penetrated CHS X-joints, in which the brace passes through the chord.

Although penetrated CHS X-joints are frequently applied by Dutch engineering firms in civil structures and extensive guidelines and rules are available for non-penetrated X-joints, there are no specific design rules available for penetrated CHS X-joints and research into these joints is limited.

This research focused on gaining insight into and predicting the behavior of penetrated CHS X-joints. Since very limited research has been done into this type of CHS X-joints, literature and existing research into a comparable penetrated connection, plate-to-structural hollow sections (SHS), has been studied. Analogous to the penetrated CHS X-joints and their non-penetrated equivalents, the behavior of through plate joints is compared with their corresponding branched plate equivalents.

In Section 2.1 the failure mechanisms and design rules for non-penetrated X-joints according to EN 1993-1-8 are presented and elaborated. The literature study into comparable penetrated connections, is then elaborated in Section 2.2.

In a similar way, as done in the literature study, in this research, a Finite Element (FE) model is created of both a penetrated CHS X-joint and its 'standard', non-penetrated equivalent in which the brace is welded to the chord. A schematic view of both joints and an example structure of the joint is given in Figure 1. With a Finite Element Method (FEM) a FE model is created which is further elaborated in Section 3.

To gain insight into the structural behavior and the possible differences between the penetrated and non-penetrated X-joints, a numerical parameter study is conducted in which applied loads as well as geometrical dimensions are varied. The effects of the boundary conditions and material models on the joint behavior are evaluated once and then fixed for the remaining of this research.

By analyzing the results of the parameter study, which are elaborated in Section 4, and comparing the different failure mechanisms of the penetrated and non-penetrated CHS X-joints, several critical areas are distinguished for which the current set of design rules insufficiently describes the behavior of the joint and the capacity of the penetrated CHS X-joint is underestimated significantly.

Since it appears that the design rules for (non-penetrated) CHS X-joints, as provided in the EN 1993-1-8, do not apply to penetrated CHS X-joints in those critical areas, a suggestion for an adjustment or addition to the existing design rules is presented. In Section 5, the development and performance of these rules is elaborated.

**Concludingly, it is the objective of this study to gain insight into and be able to predict the behavior of penetrated CHS X-joints. Moreover, a clear and uniform set of design rules that can be used for the calculation of penetrated CHS X-joints is aimed for.**

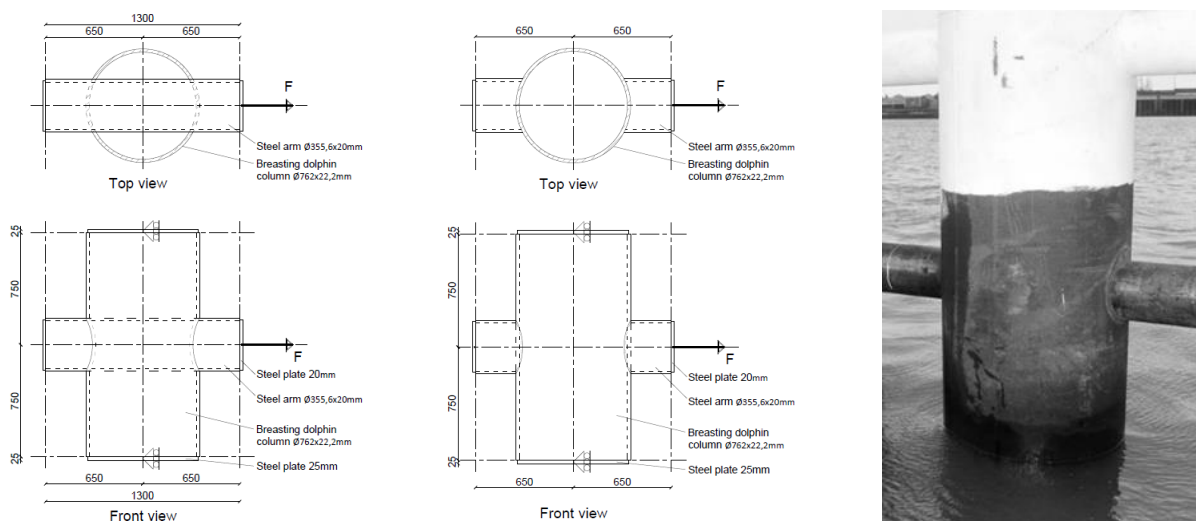


Figure 1: Penetrated CHS X-joint (left), "standard" non-penetrated CHS X-joint (middle) and an example (right) [1]





## 2 LITERATURE STUDY

### 2.1 DESIGN RULES FOR HOLLOW SECTION JOINTS

The NEN-EN 1993-1-8 provides design rules for the determination of the static design resistance of hollow section joints in uniplanar and multiplanar arrangements. The provided design rules are applicable to circular, square and rectangular hollow sections in various configurations, e.g. K-, N-, Y-, T- and X-joints. This research focusses on penetrated X-joints, in which a single brace penetrates the chord, in contrast to its conventional equivalent in which two coaxial braces are connected to the chord. The scope of this research is limited to uniplanar connections for which  $\theta$ , the included angle between the brace and the chord, equals 90 degrees. For these connections, the influence of the penetration of the chord is researched for various loading conditions, including both single-sided loading, for which only one of the brace edges is loaded, and double-sided loading. For the latter, the joint is expected to behave as an X-joint, however, the behavior of the former may possibly show more resemblance to T-joints. Therefore, in this paragraph the EC design rules, as provided in Section 7 of the NEN-EN 1993-1-8, for both X-joints, as well as for T-joints, are elaborated.

#### 2.1.1 Failure modes for hollow section joints

For CHS T- and X-joints, the design resistance of the chord, brace, and the connection is based on the following failure modes, as stated in the NEN-EN 1993-1-8 [2] and provided in Figure 2:

- Chord face failure** (plastic failure of the chord face) or chord plastification (plastic failure of the chord cross-section);
- Chord sidewall failure (or chord web failure)** by yielding, crushing or instability (crippling or buckling of the chord side wall of chord web) under compression brace member;
- Chord shear failure;**
- Punching shear failure** of a hollow section chord wall (crack initiation leading to rupture of the brace members from the chord member);
- Brace failure** with reduced effective width (cracking in the welds or in the brace members);
- Local buckling failure** of a brace member or of a hollow section chord member at the joint location. [2]

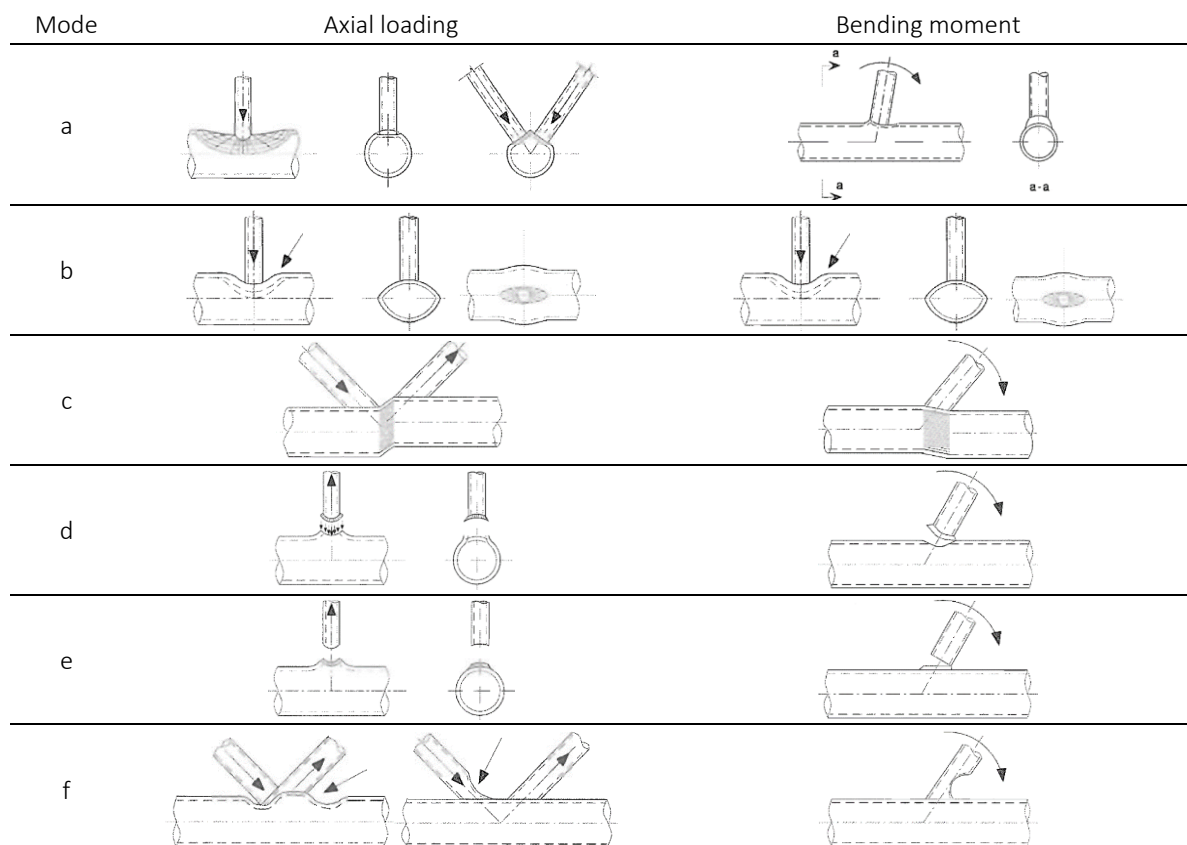


Figure 2: Failure modes for joints between CHS members [2]

### 2.1.2 Design resistance

In general, the chord and brace member(s) shall be designed to have sufficient design resistance to safely withstand the design values of the internal axial forces and/or moments, according to EN 1993-1-1. Moreover, the welded connection between the chord and the brace shall be designed to have sufficient resistance and deformation capacity to allow redistribution of bending moments. However, the actual resistance and check of the welds is out of the scope of this research. The design rules provided in NEN-EN 1993-1-8 Section 7.4 are outlined in Paragraph 2.1.2.2 till 2.1.2.4, and may be used to determine the design capacity of the X- and T-joints when the validity requirements outlined in Paragraph 2.1.2.1 are met. Design rules are provided for braces subjected to an axial force, braces subjected to a bending moment or subjected to a combination of both. The calculated maximum design resistance is expressed in terms of a maximum axial force or bending moment on the brace member and should be calculated using the stresses as defined below.

The stresses in the chord  $\sigma_{0,Ed}$  or  $\sigma_{p,Ed}$  should be determined from [2]:

$$\sigma_{0,Ed} = \frac{N_{0,Ed}}{A_0} + \frac{M_{0,Ed}}{W_{el,0}}, \quad (2.1)$$

$$\sigma_{p,Ed} = \frac{N_{p,Ed}}{A_0} + \frac{M_{0,Ed}}{W_{el,0}}, \quad (2.2)$$

where:

$$N_{p,Ed} = N_{0,Ed} - \sum_{i>0} N_{i,Ed} * \cos \theta_i. \quad (2.3)$$

Where  $\sigma_{0,Ed}$  is the maximum compressive stress in the chord at the joint and  $\sigma_{p,Ed}$  is the value of  $\sigma_{0,Ed}$  excluding the chord stress due to the axial force in the brace at that joint.  $N_{0,Ed}$  and  $N_{p,Ed}$  are the design values of the internal axial force in the chord, which relate to each other in a similar way as  $\sigma_{0,Ed}$  and  $\sigma_{p,Ed}$ .  $M_{0,Ed}$  represents design value of the bending moment in the chord,  $A_0$  is the cross-sectional area of the chord,  $W_{el,0}$  is the elastic section modulus of the chord, and  $\theta_i$  is the angle between the brace and chord, where  $i$  refers to the relevant brace member  $i$ , in this research limited to  $i = 1$ . [2] Note that, in this thesis the subscript 1 refers to the brace whereas the subscript 0 refers to the chord member.

#### 2.1.2.1 Range of validity

The design rules can be applied for hot finished hollow sections and cold formed hollow sections with a minimal nominal wall thickness of 2.5 mm for both hollow sections, a nominal chord wall thickness of less than 25 mm and a nominal yield strength of less than 460 N/mm<sup>2</sup>. The design resistance of elements with yield strengths higher than 355 N/mm<sup>2</sup>, needs to be reduced by multiplying for a factor of 0.9.

Furthermore, to use the provided design rules for the calculation of the design resistance of CHS joints, the members in compression must belong to either the class 1 or class 2 steel profiles and additionally, the validity requirements as presented in Table 1 must be met. These validity requirements regulate the relationship between the dimensions of the chord and the brace. The ratio between the brace and chord diameter,  $d_1$  and  $d_0$  respectively, needs to be between 0.2 and 1.0. Additionally, the ratio between the chord diameter ( $d_0$ ) and wall thickness ( $t_0$ ) needs to be between 10 and 50 for braces subjected to both tension and compression, and the brace diameter ( $d_1$ ) to brace wall thickness ( $t_1$ ) ratio needs to be below 50 for members subjected to tension. [2] If the requirements are met, only the resistance of the joint to the chord face failure and punching shear failure needs to be considered. The design resistance of the CHS joint is then defined as the minimum of those two values, which can, depending on the loading condition, be calculated using the rules as elaborated in the following paragraphs. For joints that do not meet the requirements of Table 1, all failure modes as described in Paragraph 2.1.1 should be taken into consideration for the calculation of the design resistance. [2] However, these joints are beyond the scope of this research.

Table 1: Range of validity for welded joints between CHS brace and chord members [2]

Diameter ratio		$0.2 \leq d_1/d_0 \leq 1.0$
Chords	Tension	$10 \leq d_0/t_0 \leq 50$
	Compression	Class 1 or 2 & $10 \leq d_0/t_0 \leq 50$
Braces	Tension	$d_1/t_1 \leq 50$
	Compression	Class 1 or 2

### 2.1.2.2 Brace subjected to axial load

Figure 3 shows a schematization of a CHS T- and X-joint, subjected to compression or tension. The NEN-EN 1993-1-8 Table 7.2 [2] provides calculation rules to predict the design resistance for chord face failure and punching shear failure of joints for which the brace is subjected to axial loads. These formulas can be used to obtain the design resistance for chord face failure of T- and X-joints. The resistance to chord face failure for T-joints can be calculated with the formula provided in Equation 2.4, and the formula for X-joints is provided in Equation 2.5. [2]

$$N_{1,Rd} = \frac{\gamma^{0.2} * k_p * f_{y0} * t_0^2}{\sin \theta_1} * (2.8 + 14.2 * \beta^2) / \gamma_{M5}, \quad (2.4)$$

$$N_{1,Rd} = \frac{k_p * f_{y0} * t_0^2}{\sin \theta_1} * \frac{5.2}{(1 - 0.81\beta)} / \gamma_{M5}. \quad (2.5)$$

$$\text{For } n_p > 0 \text{ (compression): } k_p = 1 - 0.3 * n_p * (1 + n_p), \quad \text{but } k_p \leq 1.0$$

$$\text{For } n_p \leq 0 \text{ (tension): } k_p = 1.0$$

In these formulas,  $\gamma$  is the ratio of the chord diameter to twice its wall thickness ( $\gamma = d_0/2t_0$ ),  $\beta$  is the chord diameter to the brace diameter ratio ( $\beta = d_0/d_1$ ), and  $\gamma_{M5}$  is the partial safety factor for joint resistance in hollow section lattice girders.  $k_p$  is a reduction factor based on  $n_p$  which takes into account the stress ratio between the action stress in the chord and the yield strength and can be calculated using  $n_p = (\sigma_{0,Ed}/f_{y0})/\gamma_{M5}$ . [2]

Finally, the design resistance for punching shear failure for both joint types when  $d_1 \leq d_0 - 2t_0$ , can be calculated using Equation 2.6:

$$N_{1,Rd} = \frac{f_{y0}}{\sqrt{3}} * t_0 * \pi * d_1 * \frac{1 + \sin \theta_1}{2 \sin^2 \theta_1} / \gamma_{M5}. \quad (2.6)$$

### 2.1.2.3 Brace subjected to bending moment

In Figure 4, a schematization of a CHS T-joint subjected to a bending moment is shown. The NEN-EN 1993-1-8 [2] provides calculation rules to predict the design resistance to chord face failure and punching shear failure for joints where the brace is subjected to a bending moment. The Eurocode (EC) formulas for the chord face failure resistance for a T- and X-joint subjected to an in-plane bending moment  $M_{ip}$  and out-of-plane bending moment  $M_{op}$  are provided in Equation 2.7 and 2.8, respectively. [2]

$$M_{ip,1,Rd} = 4.85 * \frac{f_{y0} * t_0^2 * d_1}{\sin \theta_1} * \sqrt{\gamma} * \beta * k_p / \gamma_{M5}, \quad (2.7)$$

$$M_{op,1,Rd} = \frac{f_{y0} * t_0^2 * d_1}{\sin \theta_1} * \frac{2.7}{1 - 0.81\beta} * k_p / \gamma_{M5}. \quad (2.8)$$

$$\text{For } n_p > 0 \text{ (compression): } k_p = 1 - 0.3 * n_p * (1 + n_p), \quad \text{but } k_p \leq 1.0$$

$$\text{For } n_p \leq 0 \text{ (tension): } k_p = 1.0$$

The design resistance formulas for punching shear failure, given that  $d_1 \leq d_0 - 2t_0$ , are provided in Equation 2.9 and 2.10:

$$M_{ip,1,Rd} = \frac{f_{y0} * t_0 * d_1^2}{\sqrt{3}} * \frac{1 + 3 \sin \theta_1}{4 \sin^2 \theta_1} / \gamma_{M5}, \quad (2.9)$$

$$M_{op,1,Rd} = \frac{f_{y0} * t_0 * d_1^2}{\sqrt{3}} * \frac{3 + \sin \theta_1}{4 \sin^2 \theta_1} / \gamma_{M5}. \quad (2.10)$$

### 2.1.2.4 Combination of axial force and bending moments

For joints where the brace member connection is subjected to a combination of an axial force and a bending moment, the joint resistance should satisfy the following equation [2]:

$$\frac{N_{1,Ed}}{N_{1,Rd}} + \left[ \frac{M_{ip,1,Ed}}{M_{ip,1,Rd}} \right]^2 + \frac{|M_{op,1,Ed}|}{M_{op,1,Rd}} \leq 1.0, \quad (2.11)$$

where:

- $N_{1,Ed}$  is the design axial force;
- $N_{1,Rd}$  is the design axial force resistance;
- $M_{ip,1,Ed}$  is the design in-plane internal moment;
- $M_{ip,1,Rd}$  is the design in-plane moment resistance;
- $M_{op,1,Ed}$  is the design out-of-plane internal moment;
- $M_{op,1,Rd}$  is the design out-of-plane moment resistance.

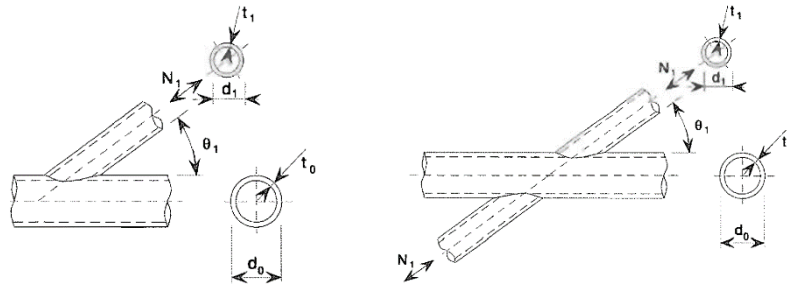


Figure 3: T- and X-joint subjected to an axial force [2]

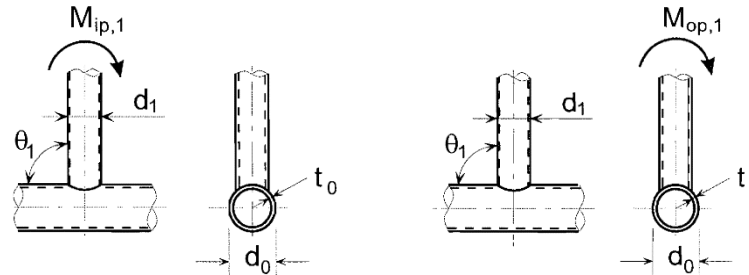


Figure 4: T-joint subjected to in-plane and out-of-plane bending moment [2]

### 2.1.2.5 CIDECT Design Guides

The CIDECT is an international association researching steel construction and engineering with CHS's as main focus, for which they also provide design guides. The CIDECT provides the design rule "chord plastification" and "punching shear" for non-penetrated CHS joints, for which the design rule chord plastification is comparable to the EC design rule for chord face failure, and the punching shear failure design rule is exactly the same as the EC design rule. The design rule for the prediction of geometries failing in chord plastification is given as:

$$N_{1,Rd} = \frac{F_{y0} * t_0^2}{\sin \theta_1} * \frac{2.6 + 2.6 * \beta}{1 - 0.7 * \beta} * \gamma^{0.15} * Q_f, \quad (2.12)$$

where  $Q_f = (1 - |n|)^{C1}$ , which can be calculated by  $n = \frac{N_{0,Ed}}{N_{pl,0,Rd}} + \frac{M_{0,Ed}}{M_{pl,0,Rd}}$  and  $C1 = 0.45 - 0.25 * \beta$ . [3]

To compare the design rules from the CIDECT with the EC design rules, the design resistances are calculated for different parameter configurations. From these calculations, it can be concluded that the formula for chord plastification almost predicts the same yield loads as the design rule from the EC for chord face failure. The design rules of the CIDECT are therefore, not further taken into account within this study.

## 2.2 PENETRATED HOLLOW STRUCTURAL SECTION

During the literature search into performed studies and realized projects into CHS X-joints, no information could be found about penetrated CHS X-joints. However, some studies on penetrated plate-to-hollow structural sections (HSS) were found: Kostas and Packer researched “Longitudinal plate and through plate-to-hollow structural section welded connections” [4], Voth et al. looked into “Branch plate-to-circular hollow structural section connections, part I and part II” [5] [6] and lastly, Voth and Packer studied “Circular hollow through plate connections” [7]. These studies may be interesting for the current research due to their applicability for CHS joints and their relation to penetrated connections. In this paragraph, these relevant studies are evaluated and information on the researched joint configuration, applied deformation limit, the finite element modeling, parameter study and conclusions and recommendations are provided.

### 2.2.1 Through plate-to-hollow structural section joint

HSS are becoming a commonly used steel member, and the joint possibilities and techniques are still expanding. Within the performed researches into HSS, the main focus lies on CHS joints. CHS joints have their own specific design rules that are provided in the NEN-EN 1993-1-8 [2], in the design guide for CHS joints under predominantly static loading [8], and in the study of “Deformation limit for the ultimate strength of hollow joints” by Wardenier J. and Winkel L.H. [9].

Currently, joints and connections between circular hollow sections are expensive due to their complex and labor-intensive joint designs [4]. With the further optimized processing techniques that are applied nowadays, such as for example laser cutting techniques, more precise joints can be designed and created in a limited time period, which reduces previous drawbacks of these joints in terms of costs. Therefore recently, an increasing amount of research is done to further optimize CHS joints and expand the possible joint types, including also penetrated joints in CHS members. Penetrated CHS-to-CHS joints are still relatively unknown, however a more commonly applied similar joint type, optimized plate-to-CHS joints, have been studied before. In these joints, the plate passes through the CHS, and the welded connection is applied on both sides of the CHS, for which an example is shown in Figure 5. These types of plate joints are often applied as shear joints or in wind bracing connections. Especially in wind bracings, where the normal force in the diagonal is distributed via the plate to the CHS. The double welded connection, on both sides of the CHS column, can be beneficial for the distribution of the stresses and the activation of the back of the CHS column.

### 2.2.2 Design resistance by deformation limit

In accordance with the research goal of this thesis, in these studies the behavior of through plate joints is compared with their corresponding branched plate equivalents. As a first indication for the resistance of the through plate joints, i.e. penetrated plate-to-CHS joints, the design rules for uniplanar branch plate-to-CHS connections under axial load are used and deformation limits provided by the research from Wardenier J. and Winkel L.H. are applied. [4] [5] [6] [7] [9] The deformation limits give practical restrictions for the joint deformations in the serviceability limit state and the ultimate limit state. In the serviceability limit state, an ultimate deformation limit of 1% of the diameter ( $1\% d_0$ ) of the main CHS member is allowed for. While in the ultimate limit state, the ultimate deformation limit is set to 3% of the chord diameter ( $3\% d_0$ ).

### 2.2.3 Finite element modeling

In the evaluated studies, the created finite element (FE) models and assumptions are validated using experimental tests. The test and the results obtained using the FEM are compared and verified on the overall load-deformation behavior, local deformation, local spot strain, and ultimate failure mechanisms. Validation of the FE models ensures that the FE model and associated assumptions are verified and that the results of the FE models approach reality. The validation of the FE models allows for the expansion of the model to a numerical parametrical model. [5] In the next paragraphs, the geometries, boundary conditions, mesh-, and material properties researched in the mentioned studies will be evaluated.



Figure 5: Example of a through plate connection to a CHS [6]

### 2.2.3.1 Geometry and boundary conditions

Both transverse and longitudinal oriented through plate-to-CHS connections and their branched equivalents have been researched for T-type as well as X-type plate-to-CHS connections. The geometrical dimensions of the examined joints are based on proportionality ratios. The proportionality ratios are defined as the effective longitudinal plate depth-to-HSS width ratio ( $\eta$ ), the effective transverse plate width-to-HSS width ratio ( $\beta$ ), and the chord diameter-to-thickness ratio ( $2\gamma$ ). Where the effective longitudinal plate depth-to-HSS width ratio ( $\eta$ ) can be calculated by dividing the plate depth in longitudinal direction through the HSS width ( $\eta = h'_1/b'_0$ ), the effective transverse plate width-to-HSS width ratio ( $\beta$ ) can be calculated by dividing the plate width through the HSS width ( $\beta = b'_1/b'_0$ ), and the chord diameter-to-thickness ratio ( $2\gamma$ ) can be calculated by dividing the chord diameter through the wall thickness ( $2\gamma = d'_0/t'_0$ ), using the dimensions as shown in Figure 6. For T-type connections the chord diameter to thickness ratio must be equal or less than 50, whereas for X-type connections this ratio must be equal or less than 40. [5]

To avoid that end effects of the boundary conditions have an influence on the behavior and strength of the joint, the free "effective" length of the chord extending beyond the plate or HSS must be sufficiently long. Kostas and Packer state in their paper the following about the free length: FEM analysis showed that the free length of the chord must be greater than 1.25 times the HSS chord width ( $b_0$ ) to avoid end effects. As a precaution, a more conservative value of  $1.5 b_0$  was used in the FEM parametric study. [4]

On the contrary, Voth et al. [6] and Vegte and Makino [10] both state that the end effects can be eliminated for all geometric configurations for which the effective chord length parameter ( $\alpha'$ ) is equal or higher than 20. This effective chord length parameter can be calculated by dividing two times the effective chord length by the chord width or diameter ( $\alpha' = 2l'_0/d_0$ ). In other words, the effective chord length needs to be at least ten times the chord width or diameter, which is four times as much as stated by Kostas and Packer [4].

To ensure that the applied boundary conditions in the FE model optimally approach the boundary conditions from the experimental test set-up, in the research of Voth et al. [5] and Voth and Packer [7], end plates are modeled to the chord. Furthermore, Voth et al. researched the schematization of the model and included a boundary condition study in their research. The research concludes that by implying a fully restrained boundary condition to the CHS chord end, the modeled structure was found to have a stiffer behavior than the experimental test results. To simulate the experimental setup and conditions, deformable end plates are modeled to the CHS chord, and only the inside surface of the bolt holes are restraint against displacements. This boundary condition is applied for the T-joint, as well as for the X-joint.

### 2.2.3.2 Mesh

In all studies [4], [5], [6], and [7], solid brick elements are applied in the FE model. In the papers, mesh convergence studies are presented which have been carried out to decide on a suitable level of discretization and the best appropriate mesh settings and layout. The mesh settings are chosen based on the comparison between the FEA results and results of the experimental load-deformation responses. Voth et al. [5] [6] and Voth and Packer [7] applied in their studies eight-node solid brick elements (SOLID45), with three translational degrees of freedom per node. However, Voth et al. also executed the study with twenty-node solid brick elements (SOLID 95), which have been applied by Kostas and Packer as well [4]. Voth et al. concluded that the eight-node SOLID45 elements show a load-deformation response and an overall joint behavior that better approaches the experimentally obtained results. Additionally, Voth et al. [5] [6] and Voth and Packer [7] applied in their studies integration with hourglass control in order to limit the zero-energy modes, which are physically not possible. Moreover, in their models, both applied a nonlinear time step analysis to incorporate the nonlinear material properties, allow for large deformations, and apply a full Newton-Raphson frontal equation solver.

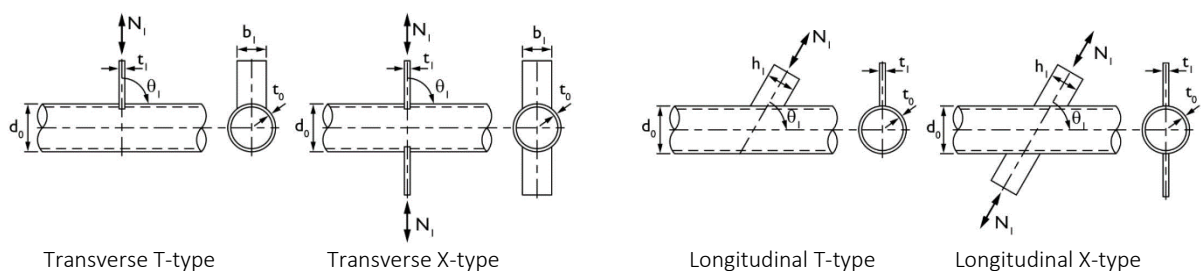


Figure 6: Branch plate joint configurations with geometric properties as used for the proportionality ratios of branch- and through plate-to-CHS connections. [5]

### 2.2.3.3 Material properties

In the mentioned papers [4] [5] [6] [7], the material models for FEA are obtained from the experimental tests. From the HSS and plate used in the experimental tests, the exact material properties are determined by tensile coupon tests. From the test results, the stress-strain curves of the average measured material properties are plotted. The engineering and true stress-strain material curves are plotted, and the true stress-strain curve is used for the FEA. The true strain is calculated by the formula  $\epsilon_{true} = \ln(1 + \epsilon_{eng})$  and the true stress value is calculated by the formula  $\sigma_{true} = \sigma_{eng}(1 + \epsilon_{eng})$ . In the research of Kostas and Packer [4] and Voth and Packer [7] the exact weld properties are not investigated. The weld is assumed to be strong and stiff enough, and the material properties are therefore assumed to be the same as the plate material. In the research of Voth et al. [5] + [6], the material behavior of the welded connection is taken into account by applying the true stress-strain behavior of the welded material in the same manner as the HSS and plate are applied.

### 2.2.4 Parametric study

For the parametric study, the researchers [4] [5] [6] [7] used the proportionality ratios as outlined in Paragraph 2.2.3.1, being the effective longitudinal plate depth-to-HSS width ratio ( $\eta$ ), the effective transverse plate width-to-HSS width ratio ( $\beta$ ), and the chord diameter-to-thickness ratio ( $2\gamma$ )

In the papers, the value of the effective longitudinal plate depth-to-HSS width ratio ( $\eta$ ) is varied between 0.32 and 4.12. Where Kostas and Packer chose for the values 0.5, 1.0, 1.5 and 2.0, Voth et al. opted for the values 0.32, 0.53, 0.72, 0.92, 1.12, 1.62, 2.12, 2.62, 3.12, and 4.12 and, finally, Voth and Packer applied an  $\eta$  of 0.32, 0.72, 1.12, 1.62, 2.12 and 2.62. The value of the effective transverse plate width-to-HSS width ratio ( $\beta$ ) is varied between 0.2 and 1.0, with intermediate steps of 0.2, and the values of the chord diameter-to-thickness ratio ( $2\gamma$ ) is varied between 13 and 46.

### 2.2.5 Conclusions and recommendations

The studies from Kostas and Packer [4], Voth et al. [5], and Voth and Packer [7], evaluated the behavior of a T-type through plate-to-CHS joints and compared it with the behavior of T-type branch plate-to-CHS joints loaded in tension and compression.

Voth et al. [6] studied the effect of the chord length and boundary conditions on the behavior of a branch plate-to-CHS X-joint. The study concluded that the effects of the chord end boundary conditions could be neglected by an effective chord length of at least  $10 d_0$  (or  $\alpha' = 20$ ). Kostas and Packer state however, that their FEM analysis showed that the free length of the chord must be greater than 1.25 times the HSS chord width ( $b_0$ ) to avoid end effects and used as a precaution, a more conservative value of  $1.5 b_0$  in their FEM parametric study. [4]

Voth et al. and Voth and Packer concluded that for branch plate-to-CHS joints loaded in tension, the CIDECT international design guidelines by Wardenier [3] underpredict the capacity of the joints significantly. For through plate-to-CHS joints, it is concluded from the parameter studies, that the joints have a capacity of more than double the capacity of an equivalent branch plate connection. Voth et al. and Voth and Packer concluded that the capacity is approximately the summation of a branch plate-to-CHS joint under tension and compression loading, which results in a capacity of even more than three times the joint capacity of a branch plate joint loaded in compression. By Voth and Packer [7], a recommendation is given for a set of design rules for through plate-to-CHS joints. In the set of design rules, the advantageous behavior of joints in which the plate penetrates the chord, is taken into account. Voth and Packer developed the following design rules for the design resistance of transverse (Equation 2.13) and longitudinal (Equation 2.14) through plate-to-CHS T-joints [7]:

$$N_1^* = f_{y0} * t_0^2 * \zeta * [2.9 * (1 + 3\beta'^2) * \gamma^{0.35} + 2.6 * (1 + 2.5\beta'^2) * \gamma^{0.55}] * Q_f, \quad (2.13)$$

$$N_1^* = f_{y0} * t_0^2 * \zeta * [7.2 * (1 + 0.7\eta') + 10.2 * (1 + 0.6\eta')] * Q_f. \quad (2.14)$$

Where  $\zeta$  is a reduction factor for the design resistance, equivalent to the inverse of the European partial safety factor and can be taken as 0.85. This reduction factor should provide sufficient conservatism for structures with a geometric parameter outside the investigated range since the parameter study used to create the design rule has been verified for a limited parameter and data range only. The factor  $Q_f$  is a factor for the chord plastification, which is provided by Wardenier in the CIDECT international design guidelines [3]. The design guideline states that  $Q_f = (1 - |n|)^{C1}$ , where  $n = (N_0/N_{pl,0}) + (M_0/M_{pl,0})$  and  $C1 = 0.25$  for chord compression stress ( $n < 0$ ), and  $C1 = 0.20$  for chord tension stress ( $n \geq 0$ ).





### 3 FINITE ELEMENT MODEL FOR CHS X-JOINTS

In this research, a finite element (FE) model is created to perform a parameter study and to predict the structural behavior, the yield, and the ultimate loads of (non-) penetrated CHS X-joints. For the FE model, a script is created using Python programming language; the script is imported in the FE software ABAQUS CAE 6.14 which is used to run the model and perform the calculations. In this section, the construction of the FE model is presented and the model is validated using the results of a research done on the “Axial capacity of circular hollow section T-joints using grade HSB 600 steel” [11]. The geometry build-up, material model, mesh settings and element types, including a mesh convergence study and the loads and boundary conditions, including a boundary condition study are elaborated in Section 3.1. In Section 3.2, the validation study of the FE model is presented. First the research and tests from literature, used for validation, are outlined. Next the adjustments to the created FEM to allow validation with the (experimental) results from the presented paper are listed. And finally, various material models are studied and the conclusions of the validation study are presented.

#### 3.1 FINITE ELEMENT MODEL

A FEM is constructed to evaluate the structural behavior and the failure mechanisms of (non-) penetrated CHS X-joints. In this paragraph, the main features of the finite element model are explained. A Python based script is used as base from which two comparable FEM’s, for the penetrated and non-penetrated joint, are created. In the following paragraph the geometrical differences between these models will be explained and in Appendix A, the Python script for the penetrated CHS X-joint is provided. Additionally, the material models, mesh settings and element types, the mesh convergence study, applied loads, and boundary conditions for the model are explained.

##### 3.1.1 Geometry

The joint geometry is modeled in a three-dimensional environment, in which the brace and the chord are modeled using deformable shell elements. Both members are build up parametrically using geometrical parameters, in a similar way as in the literature presented in section 2.2.4. The geometrical setup, based on these geometrical parameters, is equal for the penetrated and the non-penetrated models. The only difference is that for a non-penetrated joint, the part of the brace member that falls within the chord diameter has been removed, and that for a penetrated joint, the part of the chord wall that falls within the brace diameter has been removed. In the script difference is made between geometrical parameters (ratios) and geometrical properties. The geometrical parameters are used for the parameter study and are referred to with Greek symbols, while the geometrical properties are used to set up the geometry of the model and are referred to by abbreviations of the specific properties. The defined geometrical parameters are the effective chord length parameter ( $\alpha'$ ), the brace width-to-chord width ratio ( $\beta$ ), the chord diameter-to-wall thickness ratio ( $2\gamma$ ), and the brace diameter-to-wall thickness ratio ( $2\delta$ ), and can be calculated using the following formula’s:

$$\alpha' = 2l'_0/d_0 \quad (3.15)$$

$$\beta = d_1/d_0 \quad (3.16)$$

$$2\gamma = d_0/t_0 \quad (3.17)$$

$$2\delta = d_1/t_1 \quad (3.18)$$

Where  $d_0$  is the chord diameter,  $d_1$  is the brace diameter,  $t_0$  is the chord wall thickness and  $t_1$  is the brace wall thickness, and  $l'_0$  is the effective chord length, which is defined as the chord length minus the brace diameter divided by two ( $l'_0 = (l_0 - d_1)/d_0$ ). The parameters and the related geometrical properties are shown in Figure 7.

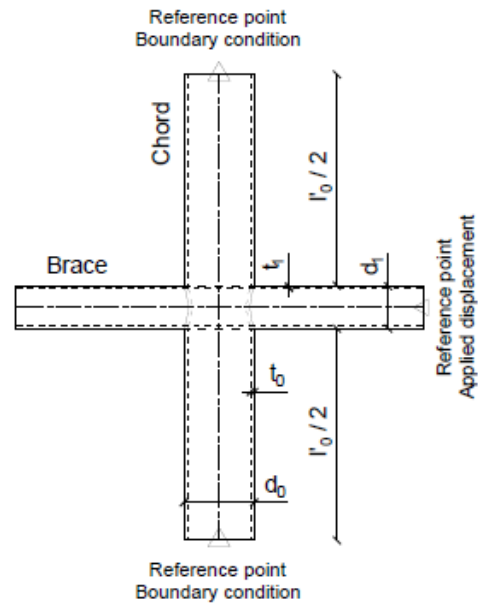


Figure 7: Geometrical parameters of a CHS X-joint

The geometrical properties are fixed formulas, used for creating the geometry. The first geometrical property is the chord diameter ( $d_0$ ), which is fixed on 762.0 mm. The second property is the chord wall thickness ( $t_0$ ), which can be calculated by dividing the chord diameter through the chord diameter-to-wall thickness ratio ( $t_0 = d_0/2\gamma$ ). With the chord diameter and wall thickness, the chord radius till mid-surface of the cross-section wall thickness can be calculated by dividing the chord diameter minus the wall thickness by two ( $r_0 = (d_0 - t_0)/2$ ). The brace diameter is set by multiplying the chord diameter with the brace width-to-chord width ratio ( $d_1 = d_0 * \beta$ ). The brace wall thickness can be calculated in the similar manner as the chord wall thickness, but this time by dividing the brace diameter through the brace diameter-to-thickness ratio ( $t_1 = d_1/2\delta$ ). Furthermore, for the brace radius the same formula holds as for the chord radius. The last geometrical properties are the chord and brace lengths. The chord length is based on the effective chord length parameter divided by two times the chord diameter, plus the brace diameter ( $l_0 = a'/2 * d_0 + d_1$ ), and the brace length is set to eight times the brace diameter plus the chord diameter ( $l_1 = 8 * d_1 + d_0$ ). The factor eight for the brace length is assumed to have sufficient length to induce the flow of stresses in the brace, while still resulting in a limited brace length, preventing the brace from buckling in compression.

With the above geometrical properties, the members can be created in Abaqus. To create the chord and brace member, the radii till mid-surface of the cross-sections ( $r_0, r_1$ ) and their lengths ( $l_0, l_1$ ) are used. After generating the geometry, the shell thicknesses and material properties are assigned to the sections.

In the next step, the members are combined. Therefore, first, the members have to be translated and moved to the right positions. Next, the members are merged, dependent instances are created from them. Doing so, creates a fixed connection on all locations where the instances intersect each other. The difference between the penetrated and the non-penetrated model is made by removing different joint parts. In the penetrated model, the part of the chord wall that falls in between the brace diameter is cut out of the model, and at the non-penetrated model, the brace part that passes through the chord is cut out the model. The different models are shown in Figure 9.

### 3.1.2 Material model

Several material models are compared and evaluated in the validation study of the FE model, which can be found in paragraph 3.2.2. Based on the outcomes from this material study, an elastic-plastic material model with linear strain hardening, which is based on the formulas as provided in the EC EN 1993-1-5 appendix C.6 [12], is adopted within this research. Furthermore, a yield strength ( $\sigma_y$ ) of 355 N/mm<sup>2</sup> and an ultimate strength ( $\sigma_u$ ) of 490 N/mm<sup>2</sup> are applied. Since this study aims to evaluate the behavior up to the plastic capacity of penetrated CHS X-joints subjected to several load cases, by the means of a parameter study, material damage is not taken into account in this analysis. The Von Mises yield criterion is used to evaluate when the geometry starts yielding and to determine the corresponding plastic capacity. The strain hardening effect is accounted for by a reduced Youngs modulus once the yield strain is reached. The reduced Youngs modulus is defined by the slope as shown in Figure 8, which can be calculated using  $\tan^{-1}(E/100)$ . The material model provided in EC EN 1993-1-5 appendix C.6 concerns the engineering stress and strain, which not represents the physics properly. Therefore, the engineering stress-strain model is converted to a true stress-strain model, which is required FEA in the software Abaqus, for which the true strain and true stress can be calculated with formula 3.19 and 3.20, respectively.

$$\epsilon_{true} = \ln(1 + \epsilon_{eng}) \quad (3.19)$$

$$\sigma_{true} = \sigma_{eng}(1 + \epsilon_{eng}) \quad (3.20)$$

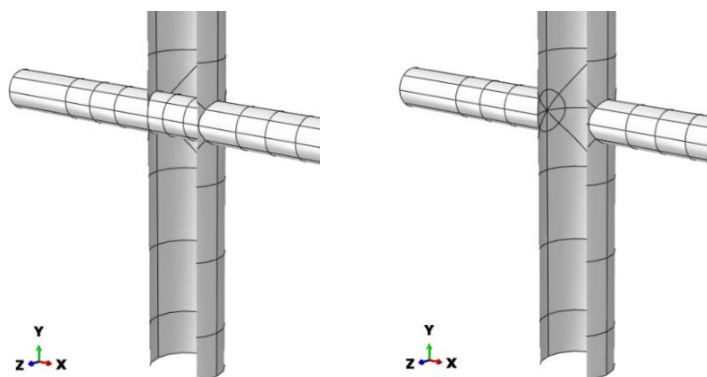


Figure 9: Geometry of a penetrated (left) and non-penetrated (right) CHS X-joint

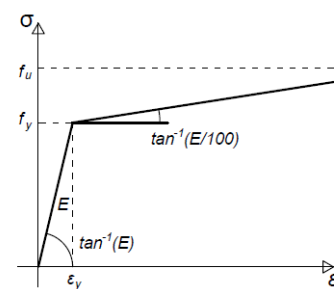


Figure 8: Elastic-plastic material model with linear strain hardening

### 3.1.3 Mesh settings and element types

In this paragraph, the mesh settings and element types are explained, and the mesh convergence study is discussed. The mesh design of the X-joint model is created using datum planes, which are planes that span two axis at a certain offset from the datum point in the direction of the third axis. These datum planes make it possible to create partitions where the plane intersects the members, as shown in Figure 11, to which different element types and mesh settings can be assigned. These distinctions allow for a reduction in the number of elements and accordingly, a reduction in computational time. Moreover, diagonal partitions were required for controlling the structured meshing technique around the connection.

#### 3.1.3.1 Mesh settings

To create an optimized mesh design, both the chord and the brace member are divided into four sections. Using the seed edges function, the number of elements or the maximum size of elements along the edges of the partitions are controlled. The region near the connection is the most important region for analyzing the joint behavior and therefore has the finest mesh. The regions near the end of the chord and the brace are less important since they have less influence on the joint behavior, and are therefore designed with a coarser mesh. The mesh is controlled by using a structured mesh technique and assigning different element shape options. Near the connection, only quadrilateral element shapes are applied to ensure that the elements in this joint region have optimal mesh shapes. On the other parts of the model, a quad-dominated shape option is applied, which uses primarily quadrilateral elements but also allows triangular elements where needed for the creation of adequate mesh shapes, for example, in mesh size transition regions [13]. The resulting meshed model is shown in Figure 11, in which it can be seen that a fine mesh is obtained near the connection between the chord and the brace, and that towards the ends of the members, the mesh size is increasing.

#### 3.1.3.2 Element type

The shell elements are applied as quadratic, 8-node doubly curved thick shell elements with reduced integration and six degrees of freedom per node (S8R). The six degrees of freedom per node take into account the translation and the rotations in three directions. The shell elements make use of a reduced integration scheme with four integration points, which are shown in Figure 10. The reduced integration option uses fewer integration points in each direction, which makes the element slightly less accurate, but in computational time, the FEA substantially faster. Moreover, the application of reduced integration mainly influences the plastic behavior, while in this research is focussed merely on the onset of the plastic behavior and therefore the application of reduced integration has very limited influence on the results of the analysis. Over the thickness of the shell element, 5 section points are defined.

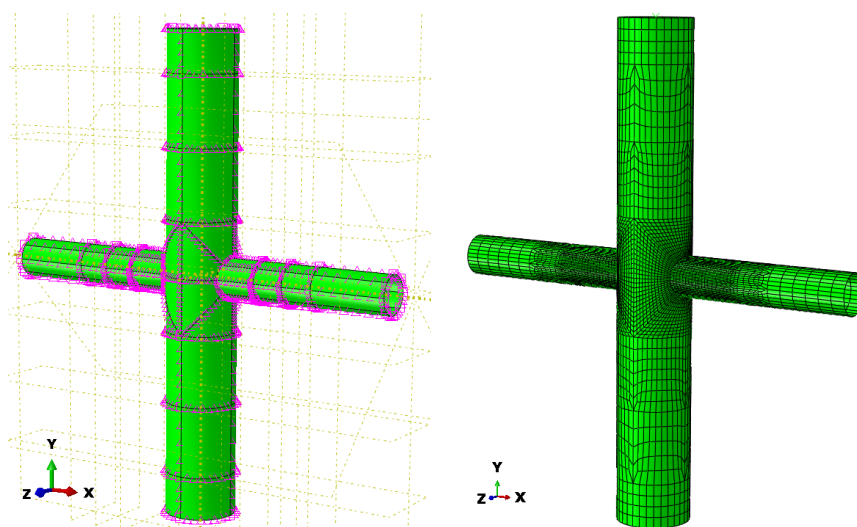


Figure 11: Partitioned and meshed geometry

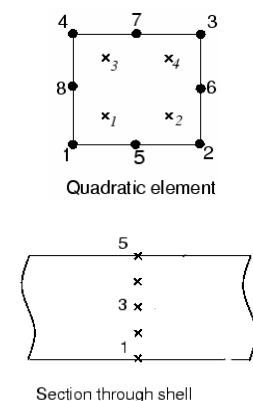


Figure 10: Reduced integration points (top) and section points (bottom) in two-dimensional elements [11]

### 3.1.3.3 Mesh convergence study

A mesh convergence study is performed to decide on a suitable mesh refinement level for which the model provides accurate results, but no more elements than necessary are applied in order to keep the required computational time limited. Initially, a FEA is performed on a coarsely meshed model. Then, the level of mesh refinement, i.e. the number of elements, is increased gradually. While the mesh becomes finer, the results should become more accurate and the influence of mesh size on the obtained results should reduce. An accurate solution is assumed to be found when further refinement of the mesh results in a negligibly small difference of the solution. For comparison of the results, the reaction force, the stress at one specific node in the chord, and displacement in one specific node in the connection between the chord and the brace are measured, which are indicated in Figure 12.

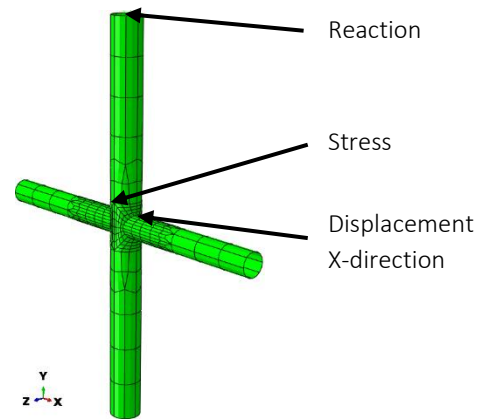


Figure 12: Locations for mesh refinement study

In section 3.1.3.1 the construction of the mesh using seeded edges and the distinctions made in mesh refinement for certain regions of the joints are elaborated; the number of seeds on the edges is increased for regions near the connections while a coarser mesh is allowed near the ends of the members. In the Python script, the number of elements on an edge is set to a specific value depending on the required mesh refinement for the region of the joint concerned. This value is expressed in terms of the geometrical dimensions of the specific edges and is multiplied with a certain 'mesh number'; this number is a factor that scales the number of seeds on the edge linearly and equals 1 for the basic 'very coarse' mesh. To increase the mesh density and study the consequent effects on the solution, the mesh number can be easily adjusted, while the proportional mesh refinement levels of the different joint regions are maintained.

The mesh number in the script is doubled from 1 till 16, causing the number of elements to grow exponentially. In the mesh convergence study, the following models with the corresponding number of elements are compared, and shown in Figure 13:

- 1 Very coarse mesh      728 elements
- 2 Coarse mesh            2880 elements
- 4 Normal mesh            11712 elements
- 8 Fine mesh                46080 elements
- 16 Very fine mesh        182784 elements

The results of the mesh convergence study can be seen in Table 2 and in the left graph in Figure 14. In the table from left to right, the mesh number, number of elements, normalized mesh density, displacement, normalized displacement, reaction force, normalized reaction force, stress, normalized stress, and the computational (CPU) time. Using the normalized results, which can be calculated by  $Normalized\ res. = X_2/X_1, \dots, X_{16}/X_1$ , the results of the different mesh refinement levels are compared with the basic 'very coarse' mesh with mesh number 1.

In the left graph of Figure 14, the normalized displacement, reaction force and stress are plotted against the normalized mesh density in blue, orange and grey respectively.

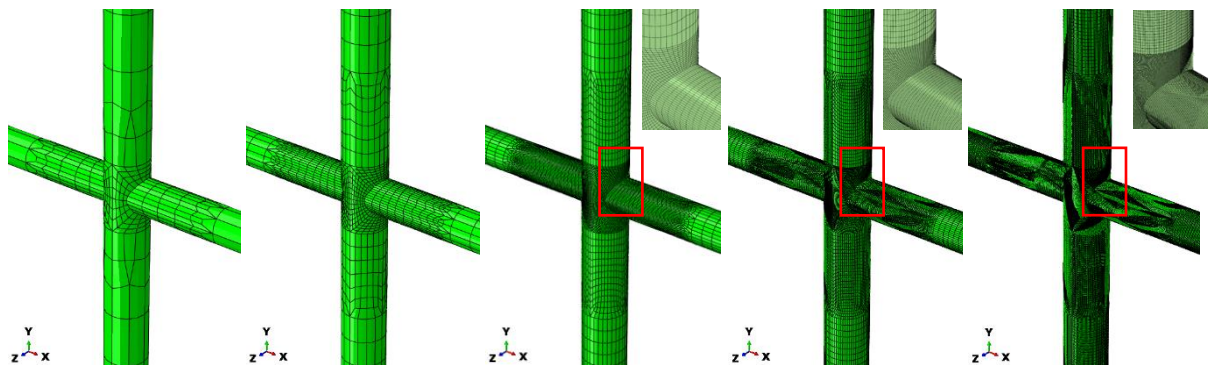


Figure 13: Very coarse (1), coarse (2), normal (4), fine (8), and very fine (16) mesh

Table 2: Mesh convergence study results mesh 1-16

Mesh	Mesh density	Norm. Mesh d.	Displ.	Norm. Displ.	RF	Norm. RF	Stress	Norm. Stress	CPU time
1 V. C.	728	1.00	4.352	1.000	1020.9	1.000	121.72	1.000	13.8
2 C.	2880	3.96	4.450	1.022	973.0	1.049	108.26	1.124	59.6
4 N.	11712	16.09	4.486	1.031	952.6	1.072	105.92	1.149	322.1
8 F.	46080	63.30	4.502	1.034	943.3	1.082	105.59	1.153	2356.1
16 V. F.	182784	251.08	4.508	1.036	939.0	1.087	105.37	1.155	20912.0

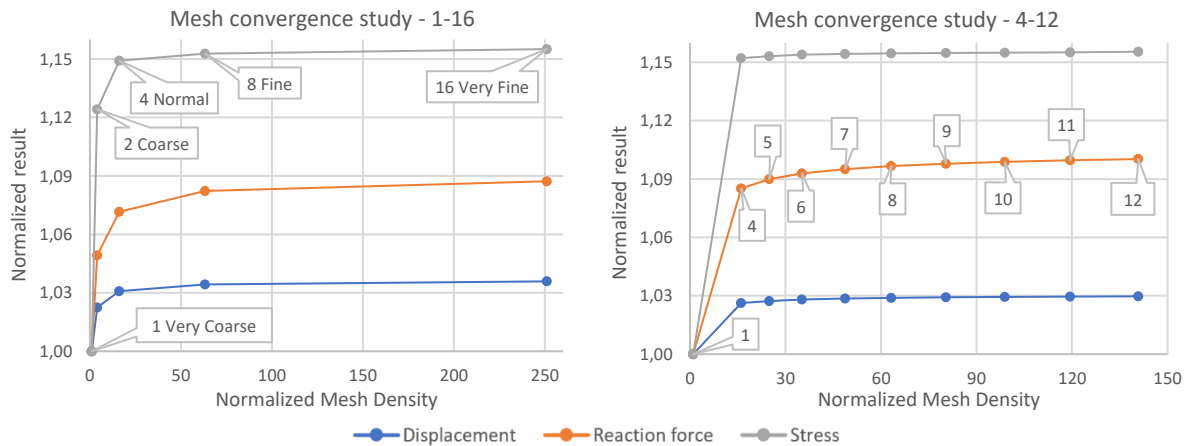


Figure 14: Normalized mesh convergence study results mesh 1-16 (left) and mesh 4-12 (right)

In the graph can be seen that between mesh number 2 and 4, an increase in mesh density still effects the results, however, between mesh number 4 and 8, the graph is flattening, and between 8 and 16, the graph is almost horizontal, yielding a converged solution. To determine on the optimal mesh refinement level, the studied mesh numbers in between these flattened and horizontal regions, is increased and an additional mesh convergence study is performed for the mesh numbers between 4 and 12. The results of this study are shown in Table 3 and in the right graph of Figure 14. The graph shows a relatively flat and horizontal line, which means that from mesh number 4 on, the results are almost stable, and convergence is reached. Comparing the results of mesh numbers four and five, there is a maximal difference observed of 0.5% for the reaction forces, while the CPU time doubles. Looking to the relative change between the parameters  $((old - new)/old * 100 = (X_4 - X_5)/X_4 * 100)$ , there is a difference of 0.43%. It can be concluded that improvements in accuracy do not outweigh the increase in computational time. Therefore, mesh number four is assumed as converging and gives sufficiently stable results without increasing the computation time too much.

Table 3: Mesh convergence study results mesh 4-12

Mesh	Mesh density	Norm. Mesh d.	Displ.	Norm. Displ.	RF	Norm. RF	Stress	Norm. Stress	CPU time
1 V. C.	728	1.00	6.677	1.000	1116.0	1.000	137.57	1.000	13.8
4 N.	11712	16.09	6.852	1.026	1028.4	1.085	119.41	1.152	322.1
5	18152	24.93	6.859	1.027	1024.0	1.090	119.30	1.153	594.8
6	25634	35.21	6.864	1.028	1021.1	1.093	119.22	1.154	1039.2
7	35496	48.76	6.868	1.029	1019.1	1.095	119.18	1.154	1814.0
8 F.	46080	63.30	6.870	1.029	1017.6	1.097	119.15	1.155	2356.1
9	58592	80.48	6.872	1.029	1016.5	1.098	119.14	1.155	3494.3
10	72000	98.90	6.873	1.029	1015.6	1.099	119.11	1.155	4660.5
11	86928	119.41	6.874	1.030	1014.9	1.100	119.09	1.155	6520.1
12 V. F.	102528	140.84	6.875	1.030	1014.3	1.100	119.06	1.155	7546.6

### 3.1.4 Loads and boundary conditions

#### 3.1.4.1 Load

Within this research, displacement controlled calculations are performed; the prescribed displacements are imposed in a stepwise manner. In the model, the prescribed displacement is applied as a boundary condition with a uniform distributed displacement on a reference point. The reference point is located at the center of the brace edge and is connected with a rigid body constraint to the edge of the brace element. The rigid body constraint is applied as tie nodes, which means that both the translational and rotational degrees of freedom are part of the constraint and that the edge motion is governed by the motion of the reference point and the relative positions of the edge nodes with respect to the reference point remain constant during the simulation. [13]

#### 3.1.4.2 Boundary conditions

Based on the conclusion of Voth et al. from the literature study, first a boundary condition study is performed. Voth et al. [6] concluded in their research, as explained in section 2.2.5, that the effect of the end boundary conditions on the behavior of a plate-to-CHS X-joint can be neglected when an effective chord length of at least  $10 * d_0$  (or  $\alpha' = 20$ ) is applied.

To see if this conclusion holds for CHS X-joints as well, four different boundary conditions and five effective chord lengths have been compared. The boundary conditions (BC) clamped, pinned, X symmetrical, and X asymmetrical are applied to the top and bottom edges of the chord. In case of a clamped BC all six degrees of freedom are fixed, for a pinned BC the displacements in X-, Y- and Z-direction are fixed, for a X symmetrical BC displacement in X-direction and rotations about the Y- and Z-axis are fixed, and for a X asymmetrical BC, displacements in Y- and Z-direction and rotations about the X-axis are fixed. For the effective chord length, the length parameters ( $\alpha'$ ) 16, 24, 32, 40, and 48 are compared. The resulting load-displacement curves for the effective chord length parameters 16, 32, and 48 are provided in Figure 15. In the graphs, the scale of the vertical axis (Force in kN) is kept equal. It can be seen that the boundary condition X asymmetrical is only plotted for an effective chord length parameter of 16. This is due to an increasing instability of this model for increasing chord lengths. The top end of the chord is allowed to displace in Y-direction. When a load is applied in X-direction on the brace, a bending moment is introduced in the chord and, therefore, due to cable effects, a large displacement of the top edge is caused. In the model with an effective chord length parameter of 16, the model is able to handle these displacements, however, in the models with a higher effective length, the model becomes unstable due to these displacements.

Additionally, it can be noticed in the graphs that the force-displacement curves of clamped and X symmetrical boundary conditions, and pinned and X asymmetrical boundary conditions coincide up to a displacement of 150 mm. The models behave equally because of the application of the boundary conditions; the boundary conditions are applied on the edge of the chord members. Applying the X symmetrical boundary condition on the chord leads to a fixed chord end, which is equal to the clamped model. The same holds for the x asymmetrical and the pinned model.

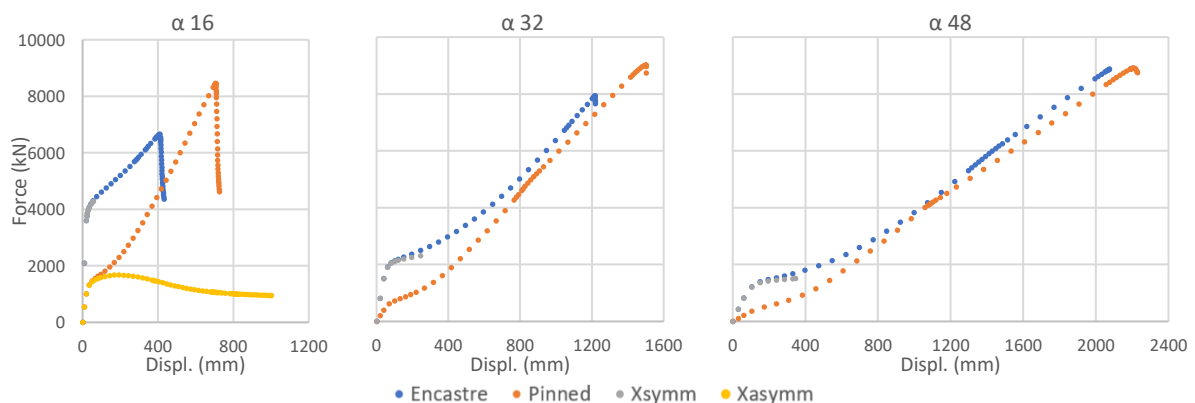


Figure 15: Force-displacement graphs boundary condition study

The graphs show that with a longer effective chord length, the type of boundary conditions applied, has less influence on the behavior of the joint, however, even for an effective chord length parameter of 48, differences in the behavior are noticeable. It is therefore concluded that the statement of Voth et al. [6], that the effects of the chord end boundary conditions can be neglected when  $\alpha' \leq 20$ , cannot be used. Furthermore, with an effective chord length parameter of 48, the bending moment of the chord will always be normative and the failure mechanisms of interest cannot be studied.

For the parameter study, the boundary conditions are applied on a reference point and tied by constrains as a rigid body to the chord edge, and the clamped and pinned boundary conditions are compared. A noticeable difference in the force-displacement curves between the boundary conditions is that the clamped boundary conditions, have a significantly higher failure load for the longer chord lengths. This is due to the failure of the chord on bending moment. Bending moment is, next to the standard member failures, one of the failure mechanisms that is not interesting for this study on the behavior of penetrated joints. Therefore, bending moment as a governing failure mechanism, needs to be avoided as much as possible within the parameter study. To do so, clamped boundary conditions will be applied at the chord ends and additionally, the effective chord length parameter is set to 12. The latter is done in order to limit the chord length and thus prevent bending moment of the chord to be governing, will ensuring to have a sufficient chord length to allow for a well distribution of the stresses around the joint.

### 3.1.5 Finite element analysis (FEA)

For the FEA of the structural behavior of a CHS X-joint, a geometric and material nonlinear analysis is implemented in the script. In this paragraph, the geometric and material nonlinear analysis and the solver methods are explained.

#### 3.1.5.1 Geometric and material nonlinear analysis (GMNA)

Within the FEM, geometrical and material nonlinearity are applied because the model will show large deformations and displacements. Geometric nonlinearity is associated with large displacements, and is applied within Abaqus by turning on the NLGEOM function. The material nonlinearity is associated with the elastic-plastic material model with strain hardening that is applied in this research, as explained in section 3.1.2. The nonlinearity makes it possible to include the changes in the geometry during the analysis and to take into account the stiffening effects; a standard Newton-Raphson incremental-iterative procedure is adopted in which the stiffness matrix is updated each iteration. [14]

#### 3.1.5.2 Solving method

As mentioned above, for the nonlinear FEA a standard Newton-Raphson incremental-iterative procedure is used. This method makes use of an algorithm to find equilibrium in every increment, where the increments are the converged stages after of a number of iterations. The stiffness matrix is updated For the nonlinear analysis, the initial time increment is set at 0.001, the maximum time increment on 0.015, and the maximum number of time increments at 200.

### 3.1.6 Output

The requested results from the FEA are obtained from the history & field output and saved in an output database and additionally, plotted in an Excel sheet. The mentioned steps will be elaborated within this paragraph.

#### 3.1.6.1 History and field output

The requested results are saved in the history and field output of Abaqus. The field output is the more general output of the data collected from the whole structure, and the history output can contain data from the whole model or specified smaller regions, e.g. specific elements or nodes. In this study, the requested data saved in the field output are the stresses, strains, plastic strains, plastic strain equivalent, elastic strains, and deformations. In the history output, the displacement and reaction force are collected at the reference point on the brace, where the load is applied. Secondly, the energy dissipated by rate-independent and rate-dependent plastic deformation (ALLPD) is requested for the whole model; this function shows plastic strains in the structure [13]. Lastly, also ten node displacements are collected; these displacements are provided to implement a deformation criterion for the ultimate load, which will be explained in the following paragraph.

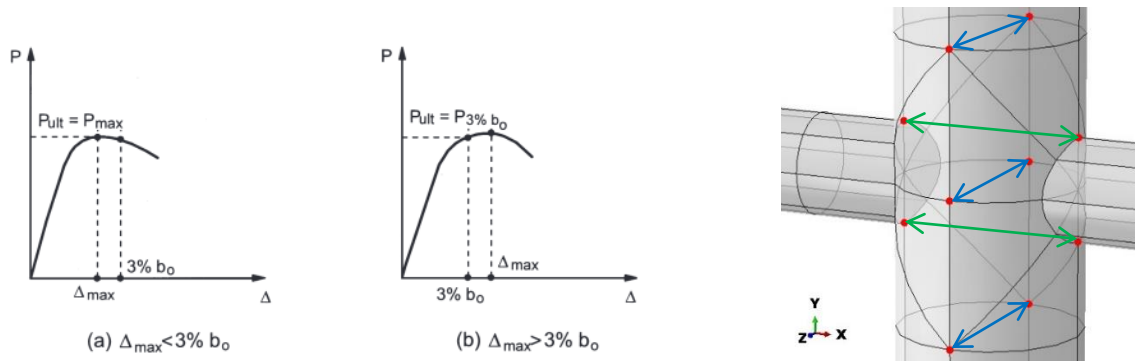


Figure 16: Deformation criterion [15] and deformation criterion application within the model

### 3.1.6.2 Deformation criterion

The ultimate load of CHS joints can be found by the lowest value of the first peak load from the load-displacement graph or via an ultimate load predicted by a deformation criterion. Wardenier J. and Winkel L.H. have performed several studies on CHS joints, after which they concluded that the ultimate load of a CHS joints also could be described by a deformation criterion. The deformation limit is set to 3% of the CHS diameter ( $3\% * d_0$ ) for the ultimate limit state, and limits the ultimate load in case excessive deformation is observed for one of the failure mechanisms that can cause the chord to be severely deformed [9], i.e. chord face failure, chord side wall failure. Two ways to determine the ultimate load obtained from FEA are thus build in, as is illustrated in Figure 16. The left graph shows that the peak load is reached by a smaller displacement than the 3% criterion; therefore, the peak load is assumed as the ultimate load. The right graph shows that the 3% deformation criterion is reached before the peak load, here the 3% deformation criterion is governing for the ultimate load.

The 3% rule is applied within the Python script as a criterion on several nodes. In the right figure in Figure 16, the application of the deformation criterion within the model is shown. Node sets are created of nodes that are situated opposite to each other, and from these node sets, the in-between distance and deformation are measured. In the figure, the node sets are shown with a double arrow in between. The blue arrows are node sets for which the deformation criterion relates to the Z-direction, and the green arrows are node sets for which the deformation criterion relates to the X-direction. If deformation between the nodes becomes more than the limit of 3%, the load capacity at that increment is stored.

### 3.1.6.3 Output database and creating Excel values

With the history and field output, an output database (ODB output) is created. To use the history and field output for processing the results, the output has to be requested upfront within the script. Therefore, the ODB output is created. For the ODB, the storage directory is set, and from the history or field output, the required results are requested. The history and field output are requested for every increment, and additionally, for the reaction force and the displacement, the maximum value reached during the simulation is requested.

### 3.1.6.4 Create Excel values

For collecting and accessing of the results, the results are plotted in an Excel sheet. For every model, an excel sheet is created and opened in which the results from the ODB output are written to. In the Excel sheet, the increment number, displacement, reaction force, plastic dissipation, deformation limit, maximum reaction force, and maximum reaction force due to the deformation limit are plotted. As a last step, the workbook is closed, so a new calculation with new parameters can be started.



## 3.2 VALIDATION OF THE FINITE ELEMENT MODEL

For the validation of the FE model, the research “Axial capacity of circular hollow section T-joint using grade HSB 600 steel” from Byong-Jeong Choi, Eun-Taik Lee, Jae-Guen Yang, and Cheol-Kyu Kang is used [11]. In their research, eight specimens with different geometries and material properties are analyzed numerically and evaluated. For the validation of the FE model, these eight specimens have been reproduced and tested experimentally as well. In this paragraph, the experimental and numerical results from Byong-Jeong Choi et al. are elaborated, and the FE model created for the current study, as described in the previous paragraph, is validated.

### 3.2.1 Experimental test

#### 3.2.1.1 Test specimen

Byong-Jeong Choi et al. did research on the axial capacity of a CHS T-joint, loaded under compression. The basic model for the test specimen is shown on the left side in Figure 17, where can be seen that the specimen lengths are fixed on a length of 3000 mm for the chord and 1950 mm for the brace, and the diameters are fixed on a diameter of 750 mm for the chord and 650 mm for the brace. The chord thickness has been varied between 12 and 26 mm, the brace thickness between 12 and 40 mm, and the material strength has been chosen as 400 or 600 N/mm<sup>2</sup>. On top of the brace, a 50 mm thick steel plate is welded, to attach the specimen to the testing machine and to introduce the forces in the brace. [11]

#### 3.2.1.2 Test setup

On the right side of Figure 17, the test setup with the locations of the LVDTs is shown. With the LVDTs, the deformations and displacements of the model are measured. [11] Next to that, the supports of the specimens are shown: it can be seen that double steel plates are welded to both chord ends.

#### 3.2.1.3 Material properties

The material properties of the specimens are obtained by coupon tests of the elements. The materials that are used for the experiments are SS400 and HSB600 steel. The SS400 steel refers to steel with yield stress ( $F_y$ ) of 235 N/mm<sup>2</sup> or 215 N/mm<sup>2</sup> for thicknesses of more than 40 mm, ultimate tensile stress ( $F_u$ ) of 400 N/mm<sup>2</sup>, and the HSB 600 steel refers to steel with a yield stress ( $F_y$ ) of 480 N/mm<sup>2</sup> for all thicknesses and ultimate stress ( $F_u$ ) of 600 N/mm<sup>2</sup>. In the paper, the minimum yield and ultimate stress are applied in the FE models. [11]

#### 3.2.1.4 Finite element analysis

For the finite element analysis, Byong-Jeong Choi et al. used the software package Abaqus to simulate a displacement controlled nonlinear static analysis using the static-Riks analysis option. For the analysis, quadrilateral shell elements with six degrees of freedom per node are applied (S4R elements). Furthermore, an elastic-perfectly plastic material model was applied, based on the minimum yield and ultimate stress as given in section 3.2.1.3. For the elastic part of the material model, the Young’s modulus ( $E$ ) of 205 GPa and a Poisson’s ratio ( $\nu$ ) of 0.3 are applied. For the welded connection between the chord and the brace was assumed that it is strong and stiff enough, and therefore, the welded connection was not modelled within the FEA. For the boundary conditions, Byong-Jeong Choi et al. assumed in the FE model that the steel plates behave as a pinned constraint on the chord ends. [11]

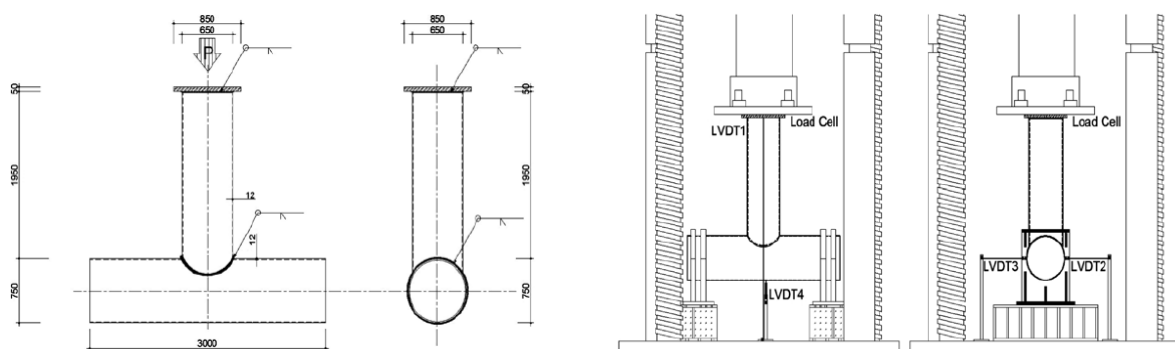


Figure 17: Test specimen and test setup with the locations of the LVDTs [11].

### 3.2.1.5 Experimental and numerical calculation results

The results of the experiment, the FEA, and design resistances calculated with the design rules from AISC and CIDECT are compared on nominal strength (kN). A ratio between the experiment result and resistance according to AISC, the experiment and FEA result, and FEA result and resistance according to AISC, is given. The results are shown in Table 4 and Figure 18, in which the results are divided into the two material groups, SS 400 series, and HSB 600 series. In the graphs, two calculation methods and four geometries are shown, where every geometry is indicated by its own color and every calculation method by its own line type. Specifications of the graphs are shown in Table 5.

Table 4: Nominal strengths and yield loads [11]

No	Specimen	Nominal strength (kN)		Exp. (kN)	FEM (kN)	Exp./AISC	Exp./FEM	FEM./AISC
		AISC	CIDECT					
1	400M-t12-bt12	995	896	1326	1400	1.33	0.95	1.41
2	400M-t12-bt40	995	896	1522	1250	1.53	1.22	1.26
3	400M-t26-bt12	4000	3600	4698	4400	1.17	1.07	1.10
4	400M-t26-bt40	4000	3600	4945	4350	1.24	1.14	1.09
5	600M-t12-bt12	2031	1828	2105	2750	1.04	0.77	1.35
6	600M-t12-bt40	2031	1828	1975	2500	0.97	0.79	1.23
7	600M-t26-bt12	8170	7353	8857	8550	1.08	1.04	1.05
8	600M-t26-bt40	8170	7353	8523	8500	1.04	1.00	1.04

Table 5: Legend two calculation methods and two steel classes with both four geometries, used to obtain results

Calculation methods		SS 400 series		HSB 600 series	
—	Choi et al. Exp. [11]	■	400M-t12-bt12	■	600M-t12-bt12
- - -	Choi et al. FEM [11]	■	400M-t12-bt40	■	600M-t12-bt40
		■	400M-t26-bt12	■	600M-t26-bt12
		■	400M-t26-bt40	■	600M-t26-bt40

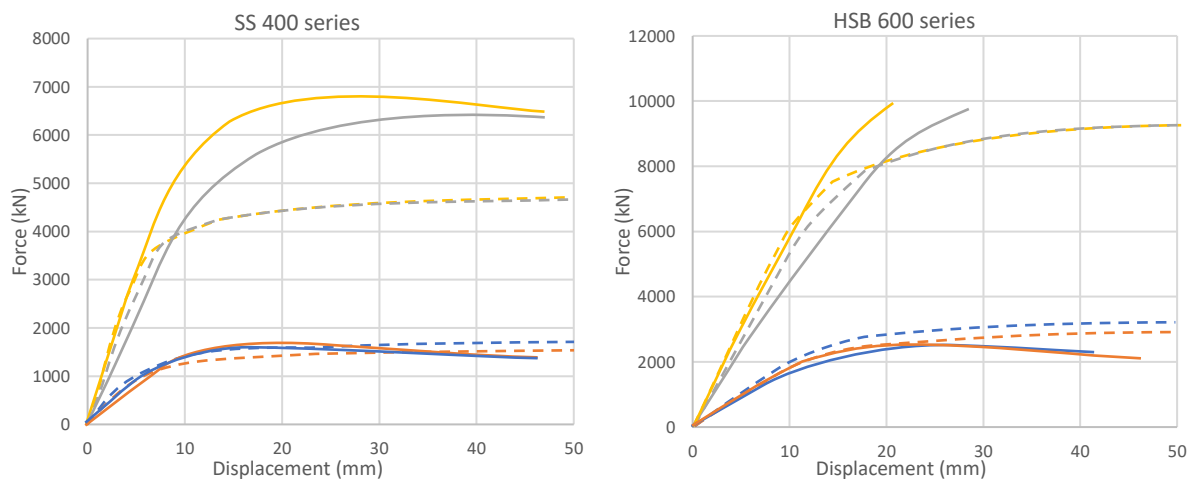


Figure 18: Force-displacement diagram experimental and numerical results

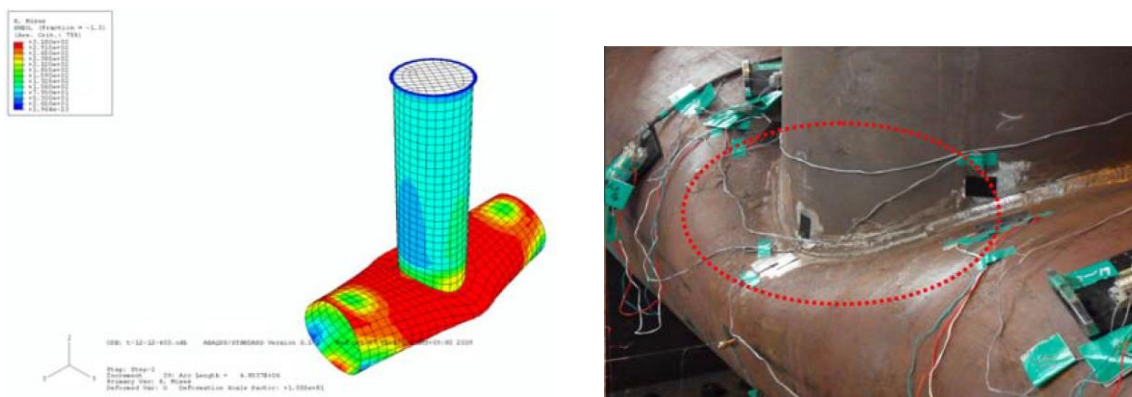


Figure 19: 400M-t12-bt12, FEM result and experimental result of geometry failing in chord face failure [11]

The results show that the behavior of the FE model differed from the experimental results. For the stiffness of the models, the elastic path is acceptable, but looking to the plastic phase, the FE model continues to increase and there is no maximum reaction force reached or softening behavior shown. The models with a chord thickness of 12 mm seem to have almost the same yield load, but for the models with a chord diameter of 26 mm, there is a significant difference in yield load. It seems that their FEA does not give accurate results to predict the behavior of the joints. In Figure 19, the finite element and experimental result of the 400M-t12-bt12 are shown. These results show that in both cases, the failure mechanism chord face failure occurs.

### 3.2.2 FE model

For the FE model created in the current research, the Python script as explained in section 3.1, is used. The python script is altered in such a way that the material model, boundary conditions and element types from the FEA in the paper are incorporated. Byong-Jeong Choi et al. used the minimum standard yield stress and ultimate stress for their FEA, instead of using the actual mechanical steel properties obtained from their coupon tests. Furthermore, they used S4R elements in their FE model and applied pinned boundary conditions to the edges of the chord.

The FEA results from the FE model created in this research with the above mentioned assumptions from Byong-Jeong Choi et al., give an acceptable prediction for the behavior of the joint, however, compared to the experimental results, the joint behaves slightly too stiff. Therefore, several steps are taken in an attempt to obtain numerical results that better match the experimental tests from Byong-Jeong Choi et al.; different element types are tested, the material properties are upgraded to the mechanical properties retrieved from the coupon tests, and furthermore, different boundary conditions and material models are studied. The FEA results of the steps taken are given in Appendix B, and the steps are described in the next paragraph.

As a first step the influence of the type of shell elements is evaluated. Byong-Jeong Choi et al. used 4-node shell elements with a linear shape function. But in some cases, it can have significant influence to calculate the stiffness matrix in a higher-order, so apply a quadratic shape function with 8-noded shell elements. In this case, the 8-noded doubly curved thick shell elements give more accurate results than the 4-node shell elements and therefore, the 8-node shell elements are applied in the following steps.

In the second step, the mechanical steel properties retrieved from the coupon tests presented in the paper are implemented. For every geometry, one coupon test was performed, and the mechanical properties of the tests are provided. The engineering stresses and strains are converted to true stresses and strains, with formulas 3.19 and 3.20. The coupon test yield and ultimate stresses are significantly higher than the stresses initially assumed, resulting in higher loads, which in this case fits the experimental results better.

After implementation of the steel properties from the coupon tests, the yield and ultimate loads fit the experimental results well, however, for the elastic part, the FE model tends to behave stiffer than is observed in the experimental results. Therefore, as a third step, the boundary conditions are varied between Pinned, X symmetrical, clamped and pinned applied on a reference point. For the first three, the boundary conditions are applied directly on the edge of the chord; for the latter, the pinned boundary with a reference point, a reference point is created on which the boundary condition is applied. In Figure 22, the left graph, the results for the varied boundary conditions are shown. It can be seen that the boundary conditions mostly influence the stiffness of the structure and the height of the yield- and ultimate load. The pinned and the clamped boundary conditions show the same results: a very stiff behavior of the structure and the highest loads. The pinned boundary condition with a reference point, shows a less stiff behavior and lower loads, however, the behavior observed in the experimental test results are best approximated by the X symmetrical boundary condition that shows the lowest stiffness and yield load. Therefore, X symmetrical is assumed as the boundary condition in the next steps.

The fourth and last step takes into account different material models. Material models from the EC EN 1993-1-5 [12] and the British standard 7910 [16] are applied. From the EC, models a, b and c are based on the standard steel properties, while model d (d1 and d2) are based on the true stress-strain curve from the coupon tests. Model d2 differed from model d1 as in model d2, the Lüders strain plateau from the British standard is implemented. Model d3 is also based on the true stress-strain curve from the coupon tests, like model d1 and d2 from the EC, but now the approach from the British standard is applied to generate a stress-strain curve.

The material models are shown in Figure 20, and the explanation of the models is as follows:  
 EC EN 1993-1-5 [12]:

- a) Elastic-perfectly plastic without strain hardening;
- b) Elastic-plastic with a nominal plateau slope;
- c) Elastic-plastic with linear strain hardening;
- d1) Elastic-plastic with linear strain hardening,  $\epsilon_u = \%$  elongation;
- d2) Elastic-plastic with linear strain hardening,  $\epsilon_u = \%$  elongation, with Lüders strain plateau.

British standard 7910 [16]:

- d3) Stress-strain curve modified from the test results.

In Figure 21 the results from the material model study are shown. In the first stage of the validation study, model a – elastic perfectly plastic was applied. In the graph, it can be seen that both model a and b, however, do not capture the hardening behavior of the material observed in experimental results. Though the d models, describe this behavior slightly better, model c provides the best approximation of the experimental results, and since it is based on a standard rule from the EC, material model c is used for obtaining the final results.

Finally, from both Figure 21 and Figure 22, it is visible that the FEA results from Byong-Jeong Choi et al. are insufficiently describing the stiffness and strength behavior observed in their experiments. Therefore, their FEM results are omitted in the graphs in the next paragraph and the results from the FE model created in this research are merely compared with their experimental results.

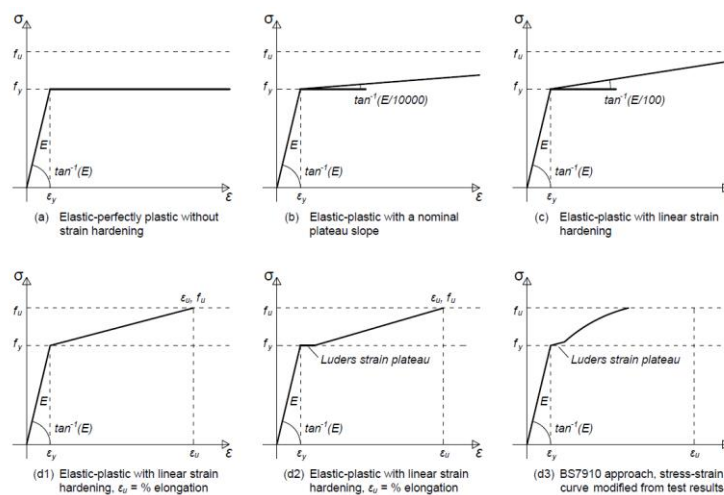


Figure 20: Material models by the EC EN 1993-1-5 and the British standard 7910 approach

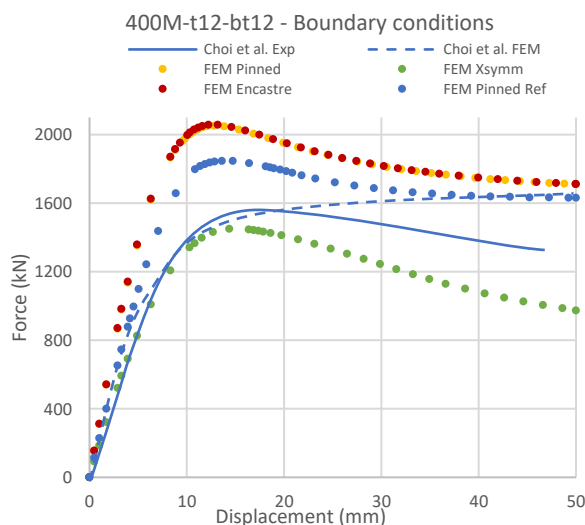


Figure 22: FEA results varied boundary conditions

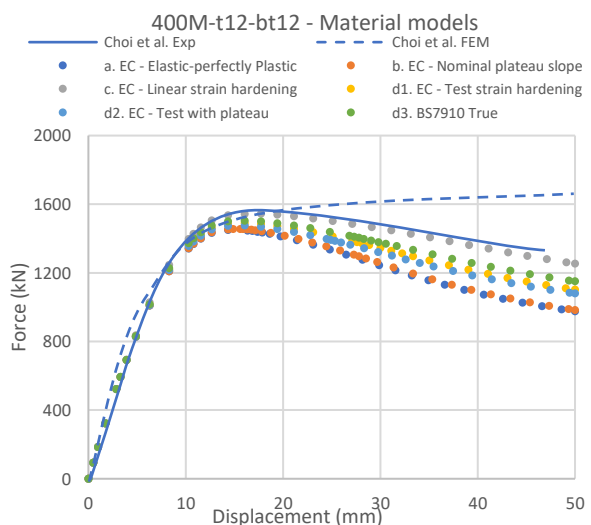


Figure 21: FEA results varied material models

### 3.2.3 Results

Concludingly, starting from a FE model with the assumptions applied by Byong-Jeong Choi et al., the following steps, as also explained in section 3.2.2, are taken to arrive at the final results:









- Shell elements varied between S4R and S8R elements;
- Material properties (true stress-strain curve) from coupon tests applied;
- Boundary condition study performed;
- Material model study performed.

With these steps taken, a FE model is created with mechanical steel properties as predicted from the coupon tests (converted to true stresses and strains), in which 8-noded doubly curved thick shell elements, pinned boundary conditions on a reference point, and a material model with strain hardening are applied. The results obtained with this optimized model are shown in Figure 23 and Figure 24. The legend associated with these graphs, indicating the different calculation methods and geometries, is shown in Table 6.

Though significant improvements have been made compared to the FEA results of Byong-Jeong Choi et al., the graphs show that the curves from the FE models do not exactly follow the curves from the experimental tests. The elastic behavior of the geometrical configurations is predicted reasonably well; only for the geometry with a chord thickness of 26 mm and a brace thickness of 12 mm in HSB 600 steel, a stiffer behavior of the joint is observed in the FEA. In addition, it can be seen that the FE models from SS 400 steel geometries show a similar trend as the experimental results in the plastic regime, however, for some geometries, the heights of the graphs, and therefore the heights of the yield loads, differ from the tests. For the geometry with a chord and brace thickness of 12 mm from SS 400 steel, the FEA describes the joint behavior quite accurately, but for the other geometries, the FE models predict, in particular, the plastic behavior of the joint less accurate. In the FE models of most of these geometries, plastic behavior of the joints is initiated slightly earlier than observed in the experimental tests, resulting in an slight underestimation of the yield loads as well.

Overall, it may be concluded that the experimental results of the SS 400 series are better approximated by the FEA than those of the HSB 600 series, and that geometries with smaller wall thicknesses of the members also match the experimental results better than those with larger wall thicknesses.

Table 6: Two methods and two steel classes with both four geometries, used to obtain results

Calculation methods		SS 400 series		HSB 600 series	
—	Choi et al. Exp. [11]		400M-t12-bt12		600M-t12-bt12
+	Finite element model		400M-t12-bt40		600M-t12-bt40
			400M-t26-bt12		600M-t26-bt12
			400M-t26-bt40		600M-t26-bt40

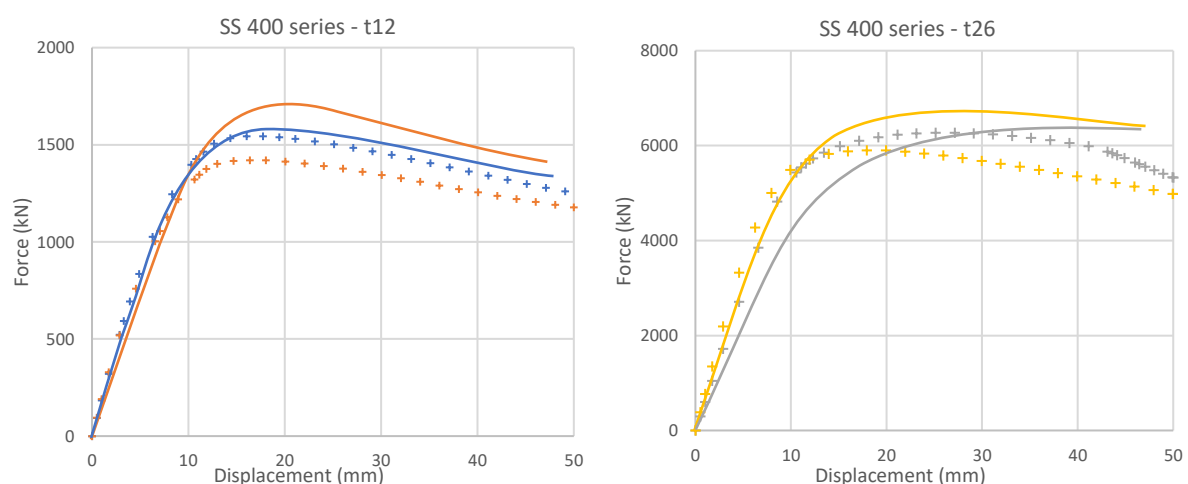


Figure 23: Validation study results for SS 400 series

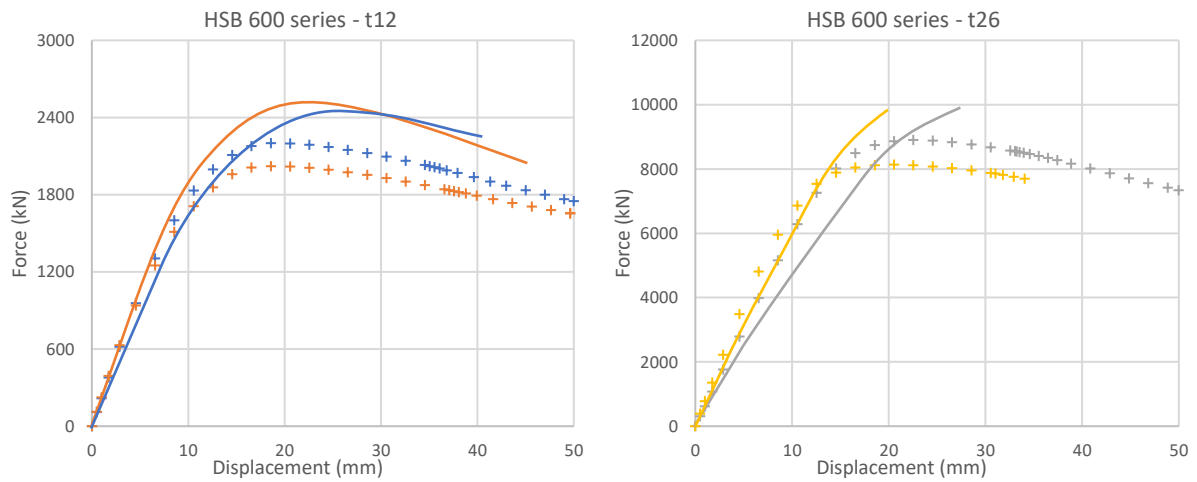


Figure 24: Validation study results for HSB 600 series

### 3.2.4 Conclusion

The numerical results describe the joint behavior as observed in the experimental tests from Byong-Jeong Choi et al. accurately enough to be able to conclude that the, in this research, created FE model works as intended. For the eight specimens the correct failure mechanisms, i.e. chord face failure and brace cross-section failure, in accordance to the experimental tests are obtained. The deviations from the FEA results in failure loads compared to the experimental results, as mentioned in the previous paragraph, may be caused by several unknown aspects of the research from Byon-Jeong Choi et al. as for example:

- A lack of information on the experimental tests and the interpretation of the results;
- Included side effects in the experimental results, that are omitted in the FEA, e.g. the weld strengths, which may provide additional stiffness;
- The interpretation and computation of the displacements and strains from the LVDT's measurements.

## 4 PARAMETER STUDY

In this section, information is provided about the performed parameter study, the failure mechanisms that may occur are elaborated, the results from the FEA are presented and the way they are processed is explained. A geometrical parameter study is performed for each of the following load combinations:

- Double-sided compression and tension ( $F_x$ )
- Single-sided compression and tension ( $F_x$ )
- Bending moment about the Y-axis ( $M_y$ )
- Bending moment about the Z-axis ( $M_z$ )
- Shear  $F_y$  (chord bending moment)
- Shear  $F_z$  (chord torsional moment)

The Python script is used to retrieve the results from the Abaqus database and create Excel files that contain the requested outputs from the FEA, as explained in section 3.1. In the Excel sheets, the following information is plotted:

- increment number;
- prescribed displacement in the reference point;
- reaction force in the reference point;
- plastic dissipation (PEEQ);
- relative deformation of the node sets (to check for the deformation limit);
- maximum reaction force reached in the reference point (RF1.1);
- maximum reaction force reached based on the deformation limit (RF1.2).

A complete overview of all results from the FEA of penetrated CHS X-joints is presented in Appendix D. Using the outputted Excel sheets, the maximum yield loads, ultimate loads, and the associated displacements are plotted in graphs. With the Abaqus viewer, the stresses and strains of the models are evaluated. The Von Mises stress ( $S_{Mises}$ ), stresses in the X- ( $S_{11}$ ) and Y- ( $S_{22}$ ) direction and the equivalent plastic strain ( $PEEQ$ ) are plotted and shown at the increment that is, by examination of the load-displacement curves, identified as the increment in which the yield load is reached. In the plots of the stresses, the yield strength is applied as the upper and lower limit (tensile and compressive yield strength, respectively) of the color bar. By setting this limit, a clear yield pattern can be observed at the increment associated with the yield load, from which the governing failure mechanism is identified. Additionally, the locations at which plastic deformation is initiated, are shown in the equivalent plastic strain (PEEQ) plots.

### 4.1 PARAMETER STUDY

In the parameter study, different parameters are chosen to create a reasonable representation of the types and geometries of CHS X-joints that can be applied in the field of civil engineering. In Figure 25, an overview of the varied parameters is shown, for which the definitions and formulas are provided in section 3.1.1 and formulas 3.15 till 3.18. The parameters varied in these study are:

- the applied load case;
- the brace width-to-chord width ratio ( $\beta$ );
- the chord diameter-to-thickness ratio ( $2\gamma$ );
- the brace diameter-to-thickness ratio ( $2\delta$ ).

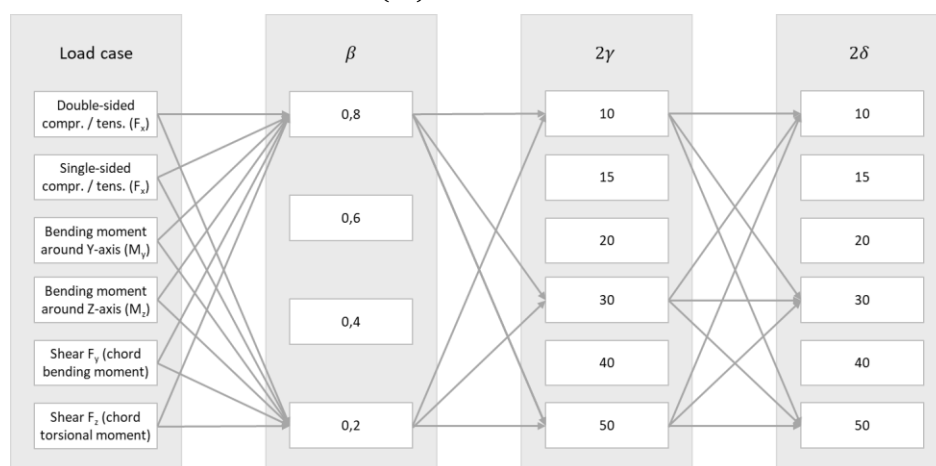


Figure 25: Overview of the parameter study

The applied load case is varied between normal forces (with respect to the brace) in the X-direction (double- and single-sided compression and tension), bending moment about the Y- and Z-axis, and shear in Y- and Z-direction. The brace width-to-chord width ratio ( $\beta$ ) is varied between 0.2, 0.4, 0.6, and 0.8, and the chord diameter-to-thickness ratio ( $2\gamma$ ), as well as the brace diameter-to-thickness ratio ( $2\delta$ ), are varied between 10, 15, 20, 30, 40, and 50.

However, it can be seen in Figure 25, that initially, not all parameter combinations are analyzed numerically. Since the main interest of this research is the behavior and capacity of joints, for which a failure mechanism is governing that cannot be calculated with, or is insufficiently described by the standard cross-section design rules from the EC, an indication for the critical areas within the varied parameter field is created first by varying the  $\beta$  between 0.2 and 0.8, and the  $2\gamma$  and  $2\delta$  between 10, 30 and 50. In this way, the limit or boundary parameter configurations are modelled and analyzed and an indication can be given for the critical areas in which joint failures occur that are insufficiently described by the current design rules. To decrease the gap between the values 10 and 50 for the parameters  $2\gamma$  and  $2\delta$ , the value 30 is also included in this first study.

For the parameter configurations in Figure 25, the failure mechanisms are derived from the results of the FEA. The critical areas are identified and further investigated. For those areas, where joint failures may occur that are described insufficiently by the EC, extra parameter configurations are modelled and investigated in order to define the parameter limits for which failure mechanism occurs and to create a larger dataset on which a newly created design rule may be fitted. The parameter study is performed for penetrated, as well as for non-penetrated CHS X-joints. The conclusions for studies on penetrated geometries are elaborated in this section and a complete overview including the stresses, PEEQ and load-displacement plots, is provided in the in Appendix C. The results of parameter study on non-penetrated geometries are compared to the results of their penetrated equivalents and a complete overview of this comparison, containing the FEA yield loads and governing failure mechanisms, is provided in Appendix D.

## 4.2 FAILURE MECHANISMS

There are several failure mechanisms for CHS X-joints, which can be divided into three groups. The first group includes the joints that fail in basic cross-section failures, which can be calculated using the standard design rules from the EC. The second group is the group of non-penetrated CHS joint failures, for which the design rules are provided in the NEN-EN 1993-1-8, and which are elaborated in section 2.1 [2]. The third group is for failure mechanisms for which the current design rules do not describe the capacity correctly and thus no suitable design rules exist, for instance, chord face failure and mixed chord side-wall failure for penetrated CHS X-joints. The three groups and the corresponding failure mechanisms are:

1. Basic section failures
  - 1 B cs Brace cross-section failure;
  - 1 B bm Brace bending moment failure;
  - 1 C bm Chord bending moment failure;
  - 1 C tm Chord torsional moment failure;
2. Non-penetrated CHS joint failures;
  - 2 C ff Chord face failure;
  - 2 C ps Chord punching shear failure;
3. Penetrated CHS X-joint failures (failure mechanism without existing design rule);
  - 3 C ff Chord face & mixed chord side-wall failures.

For the most common failure mechanisms, the failure patterns are shown in the figures below, in which the Von Mises stresses ( $S_{Mises}$ ), the stresses in the X-direction ( $S_{11}$ ), the stresses in the Y-direction ( $S_{22}$ ) and the plastic equivalent strain ( $PEEQ$ ) are plotted. In Figure 26, Figure 27 and Figure 28, brace cross-section failure, brace bending moment and chord bending moment failure from failure group 1 are shown. In Figure 29, chord face failure is shown. For this failure mechanism, the same failure patterns are observed for non-penetrated (failure group 2 C ff) and penetrated (failure group 3 C ff) geometries, however, for this latter, the capacity is insufficiently described by the existing design rules. In Figure 30, another possible failure mechanism from failure group 3 C ff, mixed chord side-wall failure, is shown. Also for this failure mechanism, no suitable design rule exists. Chord torsional moment failure from group 1 and punching shear failure from failure group 2 are not shown; these failure mechanisms are often not governing and did not occur within this research.



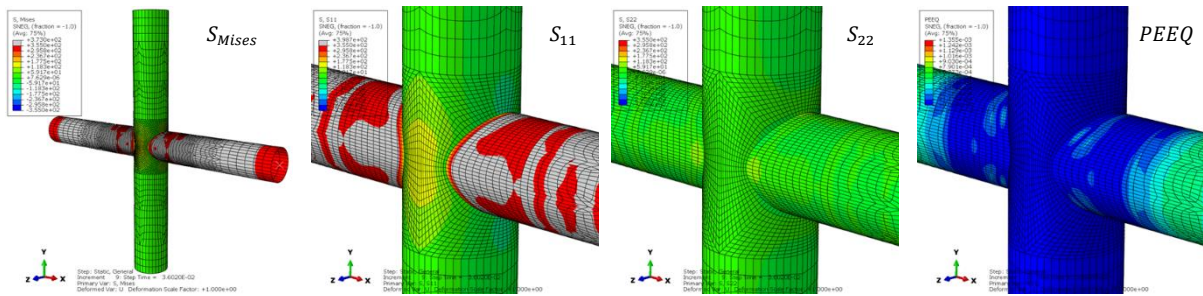


Figure 26: 1. Brace cross-section failure (penetrated joint - double-sided tension -  $\beta$  0.8 -  $2\gamma$  10 -  $2\delta$  50)

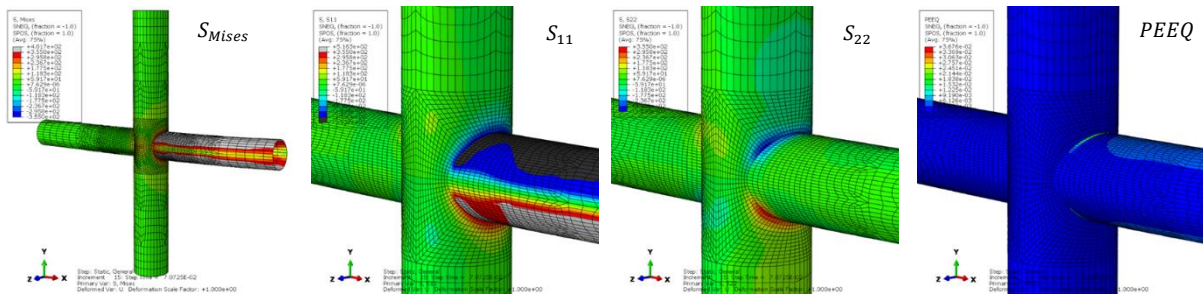


Figure 27: 1. Brace bending moment failure (penetrated joint - bending moment  $M_y$  -  $\beta$  0.8 -  $2\gamma$  50 -  $2\delta$  10)

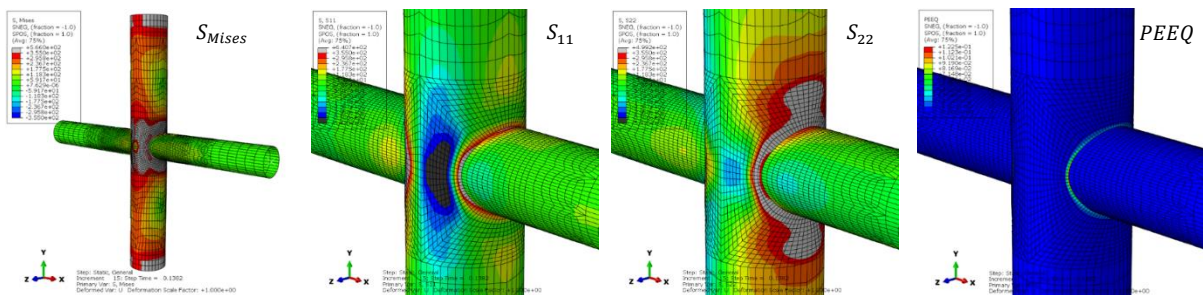


Figure 28: 1. Chord bending moment failure (penetrated joint - single-sided tension -  $\beta$  0.8 -  $2\gamma$  50 -  $2\delta$  10)

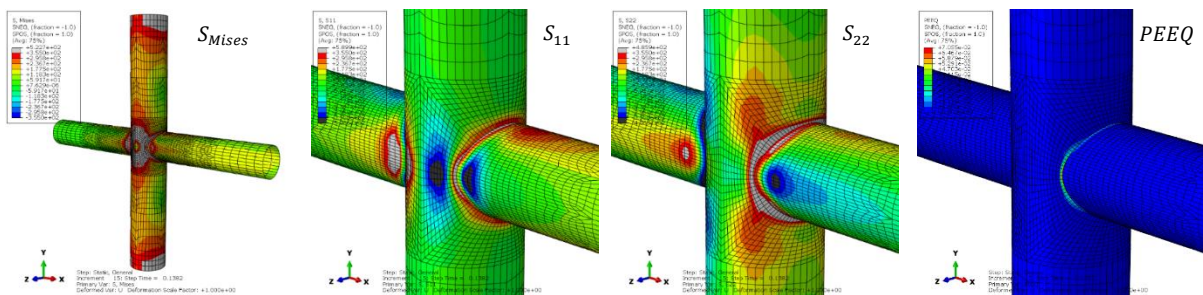


Figure 29: 2 & 3. Chord face failure (penetrated joint - single-sided tension -  $\beta$  0.8 -  $2\gamma$  50 -  $2\delta$  30)

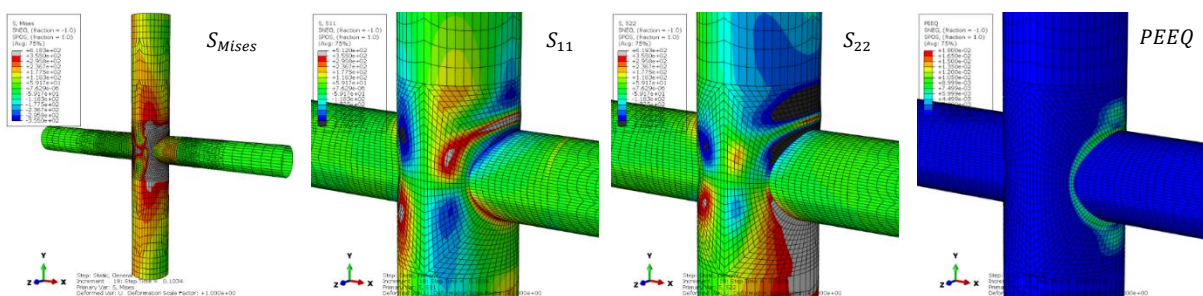


Figure 30: 3. Mixed chord side-wall failure (penetrated joint - shear -  $\beta$  0.8 -  $2\gamma$  50 -  $2\delta$  10)

### 4.3 PROCESSING RESULTS

In this paragraph, two examples are provided to show how the results are processed and to illustrate the procedure for determining the failure mechanisms. The first example is a penetrated CHS X-joint subjected to double-sided compression in X-direction ( $F_x$ ) and with geometrical parameters  $\beta 0.8 - 2\gamma 10 - 2\delta 30$ . In this model, it is evident, based on the FEA results, that from failure group 1, brace cross-section failure occurs. The second model is a penetrated CHS X-joint subjected to single-sided compression in X-direction ( $F_x$ ) with geometrical parameters  $\beta 0.2 - 2\gamma 50 - 2\delta 10$ . From the results of this model it is less obvious which failure mechanism occurs, because in the stress plots from Abaqus, the influence of two failure mechanisms can be seen, and in the force-displacement diagram, two yield and two ultimate loads can be observed. The principles used to identify the failure mechanisms for the different geometries are described in the next paragraphs and are used to obtain the governing failure mechanism of all the models in the parameter study.

#### 4.3.1 Penetrated double-sided compression $\beta 0.8 - 2\gamma 10 - 2\delta 30$

The first example is a penetrated CHS X-joint subjected to double-sided compression in X-direction ( $F_x$ ) with the geometrical parameters  $\beta 0.8 - 2\gamma 10 - 2\delta 30$ . For this geometry, the design resistance according to the EC design rules for brace cross-section failure, chord face failure, and punching shear failure are provided in Table 7. In Table 8, the FEA results for the yield load, the maximum load based on the load-displacement graph (RF1.1), the maximum load according to the deformation criterion (RF1.2), and the ultimate load (RF1), being the lowest value of RF1.1 and RF1.2, are shown. In the table can be seen that the deformation criterion is not reached, which means that the maximum deformation of the chord cross-section is less than 3%. In Figure 31, the force-displacement diagram is shown in which the yield load of 13358 kN and corresponding displacement are marked with the dashed black lines, and the ultimate load and corresponding displacement are indicated with the dashed-dotted grey lines. In Figure 32, the Von Mises stresses, and the normal stresses in the X and Y-direction from the Abaqus FEA are shown. The stresses are plotted for the increment in which, according to the force-displacement diagram in Figure 31, the yield load as given in Table 8, is reached.

Based on these stresses and yield patterns, brace cross-section failure is identified as the governing failure mechanism of the joint as it is clearly visible in Figure 32 that the brace is yielding over the whole section. The lowest design resistance according the EC design rules in Table 7 equals 13354 kN for brace cross-section failure, from which it can be concluded that the EC design rules predict both the governing failure mechanism and the yield load of the joint correctly.

Table 7: Design resistance according to EC design rules

Brace cross-section failure:		$N_{pl,Rd}$
$2\delta 30$		13354 kN
Chord face failure:		$N_{pl,Rd}$
$2\gamma 10$		30451 kN
Punching shear failure:		$N_{pl,Rd}$
$2\gamma 10$		29910 kN

Table 8: FEA results

Yield Load (kN)	RF1.1 (kN)	RF1.2 (kN)	RF1 (kN)
13358.2	14590.7	Not reached	14590.7

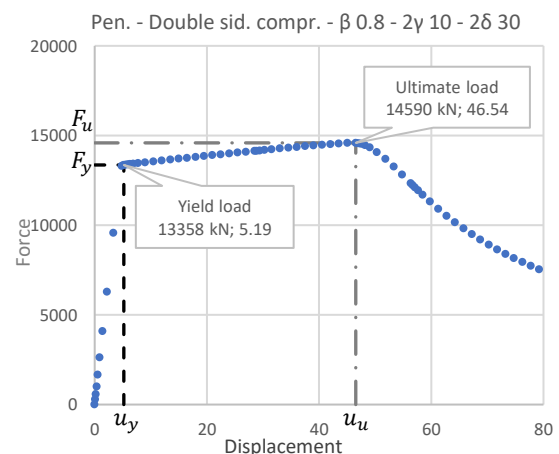


Figure 31: Force-displacement diagram

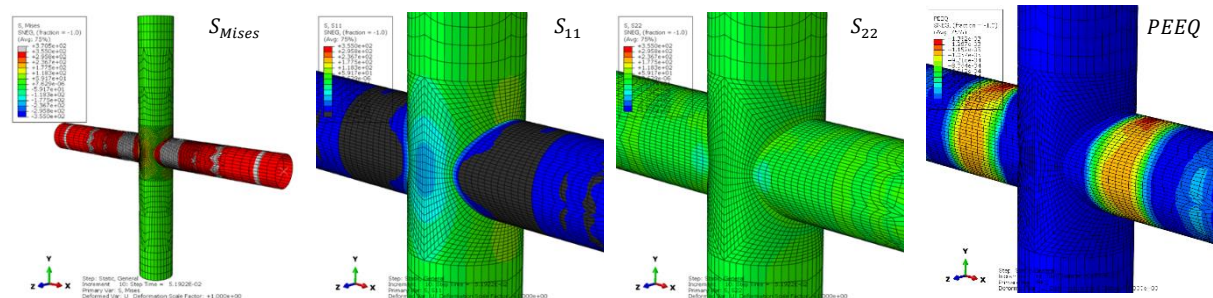


Figure 32:  $S_{Mises}$ ,  $S_{11}$ ,  $S_{22}$ ,  $PEEQ$  plotted from Abaqus

#### 4.3.2 Penetrated single-sided compression $\beta 0.2 - 2\gamma 50 - 2\delta 10$

The second example is a penetrated CHS X-joint subjected to single-sided compression in X-direction ( $F_x$ ), with geometrical parameters  $\beta 0.2 - 2\gamma 50 - 2\delta 10$ . For this geometry, the design resistances for brace cross-section failure, chord bending moment, chord face failure, and chord punching shear failure according to the EC are provided in Table 9. In Table 10, the FEA results for the yield load, the maximum load based on the load-displacement graph (RF1.1), the maximum load according to the deformation criterion (RF1.2), and the ultimate load (RF1), being the lowest value of RF1.1 and RF1.2, are shown. In the table can be seen that the maximum load from the deformation criterion is lower than the maximum load according to the load-displacement graph, and therefore RF1 equals RF1.2.

In Figure 33, the force-displacement diagram is shown, in which the yield load and corresponding displacement are marked with the dashed black line, and the ultimate load and corresponding displacement are indicated with the dashed-dotted grey line. Two kinks are observed in the curve, indicating the plastic behavior of the joint is influenced by two failure mechanisms. When evaluating the stresses plotted with Abaqus at the increment corresponding to the first kink, indeed the influence of two failure mechanisms can be identified. The first and the most evident yield pattern indicates chord face failure, as can be seen from the yield pattern that is distributed around the brace on the chord and that is mainly distributed in the Z-direction. Additionally, it can be seen that the yield strength is reached in some parts of the brace, indicating that brace cross-section failure is the second failure mechanism that has an influence on the behavior of the joint. By evaluating and comparing the results from the FEA and the design resistances according to the EC, this assumption is confirmed; the load corresponding to the second kink in the graph, indicated by the thin dashed lines, corresponds to the design resistance to brace cross-section failure according to the EC. Since the second kink is associated with brace cross-section failure, the first kink in the graph, is associated with the first observed failure mechanism; chord face failure. This means that the observed FEA yield load for chord face failure is twice as high as the design resistance for chord face failure according to the existing EC design rule. The difference between the yield load predicted by the EC design rule for non-penetrated models and the true capacity of the penetrated joint according to FEA can be attributed to the fact the brace is now continuous and penetrates the chord and some conservatism that is included in the design rules from the EC.

Besides the two kinks that are indicated in the graph, also two ultimate loads are indicated with the grey dashed-dotted lines. The highest load is the maximum load according to the load-displacement curve, however, the lower is the maximum load based on the deformation criterion which is governing in this case and thus equals the ultimate load capacity of the joint.

Table 9: Design resistance according to EC design rules

Brace cross-section failure:	$N_{pl,Rd}$
$2\delta 30$	2331 kN
Chord bending moment:	$N_{pl,Rd}$
$2\gamma 10$	5110 kN
Chord face failure:	$N_{pl,Rd}$
$2\gamma 10$	529 kN
Punching shear failure:	$N_{pl,Rd}$
$2\gamma 10$	1496 kN

Table 10: FEA results

Yield Load (kN)	RF1.1 (kN)	RF1.2 (kN)	RF1 (kN)
1165.5	2846.9	2693.1	2693.1

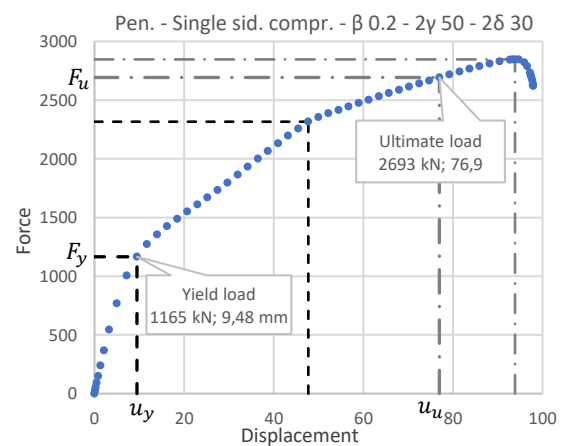


Figure 33: Force-displacement diagram

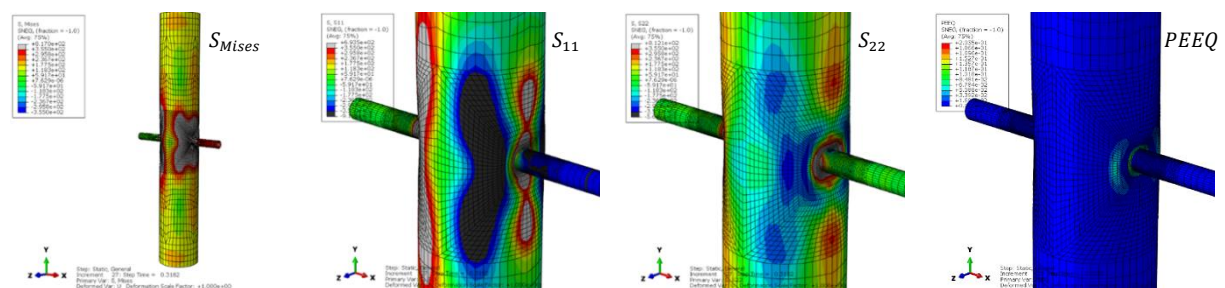


Figure 34:  $S_{Mises}$ ,  $S_{11}$ ,  $S_{22}$ ,  $PEEQ$  plotted from Abaqus

## 4.4 DOUBLE-SIDED COMPRESSION AND TENSION ( $F_x$ )

### 4.4.1 Penetrated CHS X-joint FEA results

A representation of the penetrated CHS X-joints subjected to double-sided compression and tension (by a force in X-direction) is shown in Figure 35. The results of the FEA are shown in Table 11, in which for every geometry the FEA yield load ( $F_{x,FEA}$ ), the governing failure mechanism according to FEA as identified according to the strategies outlined in the previous paragraph (*Failure mech.*), the EC plastic design resistance associated with this failure mechanism ( $F_{x,Rd}$ ), and the resistance ratio ( $RR$ ), which is the ratio between the FEA yield load and the plastic design resistance according to corresponding EC design rule ( $F_{FEA}/F_{Rd}$ ) are shown.

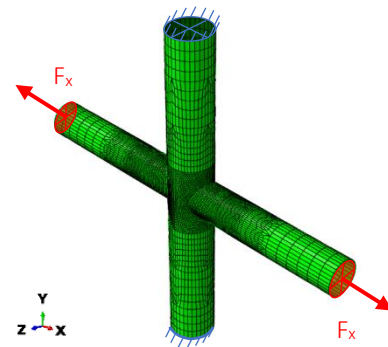


Figure 35: X-joint subjected to double-sided tension ( $F_x$ )

The resistance ratio ( $RR$ ) gives an indication of the way the true plastic capacity of the joint according to the FEA, is approximated by the design resistance according to the EC design rule associated with the governing failure mechanism. For a resistance ratio ( $RR$ ) below 1.0, the plastic design resistance ( $F_{Rd}$ ) overpredicts the plastic capacity according to FEA ( $F_{FEA}$ ) and is unsafe. For values higher than 1.3, the plastic capacity is underpredicted by the design rule and the plastic design resistance will therefore be conservative.

In the table, under ‘failure mechanisms’, it can be seen that all models subjected to compression, as well as to tension, fail in brace cross-section failure, for which the failure pattern can be seen in Figure 26. Next to that, it can be seen from the resistance ratio that the plastic design resistance obtained by the EC design rule for brace cross-section failure, fits the yield load obtained by the FEA very well.

In Figure 36, the load-displacement curves from the FEA for joints with parameters  $\beta$  0.2 –  $2\gamma$  10 and various values of  $2\delta$ , subjected to compression and tension are shown. In the graphs, a similar behavior is observed for joints in compression and tension and moreover, the yield loads of both failure mechanisms are equal. However, for the models subjected to compression a lower ultimate load is reached and the joints fail in an earlier stage than the models subjected to tension, due to local buckling of the brace members subjected to compression.

Table 11: FEA results penetrated model – double-sided compression and tension ( $F_x$ )

Model		$2\gamma$ 10				$2\gamma$ 30				$2\gamma$ 50				
Load	$\beta$	$2\delta$	$F_{x,FEA}$ (kN)	$F_{x,Rd}$ (kN)	RR	Failure mech.	$F_{x,FEA}$ (kN)	$F_{x,Rd}$ (kN)	RR	Failure mech.	$F_{x,FEA}$ (kN)	$F_{x,Rd}$ (kN)	RR	Failure mech.
Double-sided compression ( $F_x$ )	0.8	10	37473.8	37300	1.005	1 B cs	37461.4	37300	1.004	1 B cs	37455.0	37300	1.004	1 B cs
	0.8	30	13358.2	13354	1.000	1 B cs	13407.5	13354	1.004	1 B cs	13405.2	13354	1.004	1 B cs
	0.8	50	8123.5	8123	1.000	1 B cs	8117.4	8123	0.999	1 B cs	8150.9	8123	1.003	1 B cs
	0.2	10	2330.5	2331	1.000	1 B cs	2343.9	2331	1.006	1 B cs	2343.6	2331	1.005	1 B cs
	0.2	30	835.3	835	1.000	1 B cs	834.1	835	0.999	1 B cs	835.8	835	1.001	1 B cs
	0.2	50	507.2	508	0.998	1 B cs	507.8	508	1.000	1 B cs	506.7	508	0.997	1 B cs
Double-sided tension ( $F_x$ )	0.8	10	37366.3	37300	1.002	1 B cs	37365.6	37300	1.002	1 B cs	37365.9	37300	1.002	1 B cs
	0.8	30	13354.2	13354	1.000	1 B cs	13380.3	13354	1.002	1 B cs	13380.2	13354	1.002	1 B cs
	0.8	50	8124.8	8123	1.000	1 B cs	8139.8	8123	1.002	1 B cs	8139.6	8123	1.002	1 B cs
	0.2	10	2330.1	2331	1.000	1 B cs	2335.9	2331	1.002	1 B cs	2335.9	2331	1.002	1 B cs
	0.2	30	833.4	835	0.998	1 B cs	834.2	835	0.999	1 B cs	833.9	835	0.999	1 B cs
	0.2	50	506.4	508	0.997	1 B cs	507.7	508	0.999	1 B cs	507.3	508	0.999	1 B cs

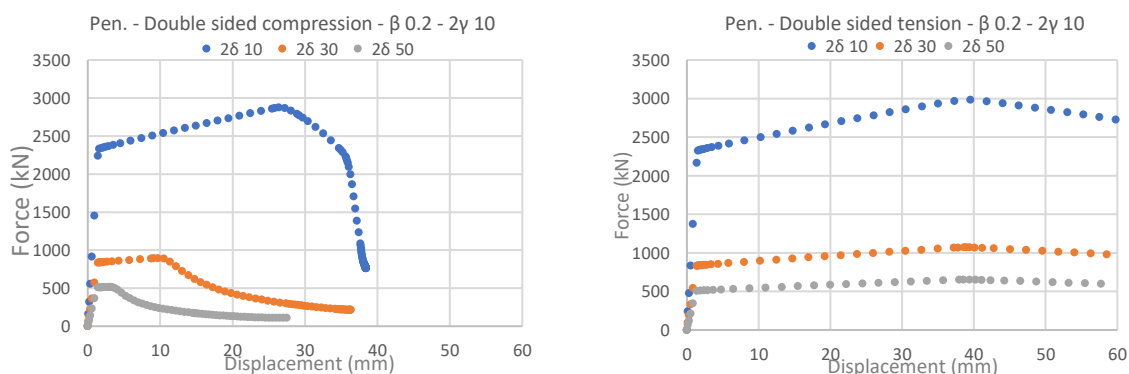


Figure 36: FEA results  $\beta$  0.2 -  $2\gamma$  10 - double-sided compression and tension ( $F_x$ )

#### 4.4.2 Comparison penetrated and non-penetrated results

The parameter configurations simulated for the penetrated joints are also simulated for the non-penetrated CHS X-joints. In Table 12 and Table 13, the results for the non-penetrated, as well as the penetrated configurations are shown, where Table 12 shows the results for models subjected to double-sided compression, and Table 13 shows the results for models subjected to double-sided tension. In the tables, for every penetrated and non-penetrated geometry, the FEA yield load ( $F_{x,FEA}$ ), the ratio between the FEA yield loads of the penetrated and non-penetrated configurations (P/N-P), the governing failure mechanism (Fail. Mech.) as identified with the strategy outlined in the previous paragraphs and the EC plastic design resistance ( $F_{x,Rd}$ ) corresponding to this failure mechanism are shown. The results of penetrated joints are shown in black and the results of non-penetrated joints are shown in grey. In column 'P/N-P', it can be seen that for the models with higher  $2\gamma$  factors and lower  $2\delta$  factors, the ratio between the FEA yield loads of the penetrated and non-penetrated configurations is above 1. This means that the plastic capacity that follows from the FEA of the penetrated model is higher than the plastic capacity of its non-penetrated equivalent. This increased capacity can be explained by the difference in governing failure mechanism; instead of chord face failure which is governing for the non-penetrated geometries, brace cross section failure is triggered for the corresponding penetrated geometries. This difference leads to an increase of the FEA yield load of penetrated geometries by a factor of 1.25 till 35.8 with respect to the yield loads of their non-penetrated equivalents. The results of the parameter configurations for which this is the case, are shaded in grey in the tables.

Table 12: Comparison penetrated and non-penetrated results double-sided compression ( $F_x$ )

Model				2 $\gamma$ 10				2 $\gamma$ 30				2 $\gamma$ 50			
L	$\beta$	$2\delta$	M	$F_{x,FEA}$ (kN)	P/N-P	$F_{x,Rd}$ (kN)	Fail. mech.	$F_{x,FEA}$ (kN)	P/N-P	$F_{x,Rd}$ (kN)	Fail. mech.	$F_{x,FEA}$ (kN)	P/N-P	$F_{x,Rd}$ (kN)	Fail. mech.
Double-sided compression ( $F_x$ )	0.8	10	Pen	37473.8	1.389	37300	1 B cs	37461.4	12.578	37300	1 B cs	37455.0	35.768	37300	1 B cs
			N-P	26982.3		37300	2 C ff	2978.4		3383	2 C ff	1047.2		1218	2 C ff
	0.8	30	Pen	13358.2	0.999	13354	1 B cs	13407.5	4.194	13354	1 B cs	13405.2	12.754	13354	1 B cs
			N-P	13368.1		13354	1 B cs	3197.1		3383	2 C ff	1051.0		1218	2 C ff
	0.8	50	Pen	8123.5	0.999	8123	1 B cs	8117.4	2.547	8123	1 B cs	8150.9	7.753	8123	1 B cs
			N-P	8131.4		8123	1 B cs	3187.2		3383	2 C ff	1051.4		1218	2 C ff
	0.2	10	Pen	2330.5	0.998	2331	1 B cs	2343.9	1.994	2331	1 B cs	2343.6	5.484	2331	1 B cs
			N-P	2334.1		2331	1 B cs	1175.8		1326	2 C ff	427.3		512	2 C ff
	0.2	30	Pen	835.3	1.000	835	1 B cs	834.1	0.997	835	1 B cs	835.8	1.977	835	1 B cs
			N-P	835.4		835	1 B cs	836.6		835	1 B cs	422.7		512	2 C ff
	0.2	50	Pen	507.2	1.000	508	1 B cs	507.8	1.003	508	1 B cs	506.7	1.246	508	1 B cs
			N-P	507.1		508	1 B cs	506.0		508	1 B cs	406.5		512	2 C ff

Table 13: Comparison penetrated and non-penetrated results double-sided tension ( $F_x$ )

Model				2 $\gamma$ 10				2 $\gamma$ 30				2 $\gamma$ 50			
L	$\beta$	$2\delta$	M	$F_{x,FEA}$ (kN)	P/N-P	$F_{x,Rd}$ (kN)	Fail. mech.	$F_{x,FEA}$ (kN)	P/N-P	$F_{x,Rd}$ (kN)	Fail. mech.	$F_{x,FEA}$ (kN)	P/N-P	$F_{x,Rd}$ (kN)	Fail. mech.
Double-sided tension ( $F_x$ )	0.8	10	Pen	37366.3	1.190	37300	1 B cs	37365.6	9.936	37300	1 B cs	37365.9	26.778	37300	1 B cs
			N-P	31396.6		30451	2 C ff	3760.5		3383	2 C ff	1395.4		1218	2 C ff
	0.8	30	Pen	13354.2	0.996	13354	1 B cs	13380.3	3.606	13354	1 B cs	13380.2	10.365	13354	1 B cs
			N-P	13406.3		13354	1 B cs	3710.2		3383	2 C ff	1290.9		1218	2 C ff
	0.8	50	Pen	8124.8	0.994	8123	1 B cs	8139.8	2.172	8123	1 B cs	8139.6	5.925	8123	1 B cs
			N-P	8173.2		8123	1 B cs	3747.1		3383	2 C ff	1373.8		1218	2 C ff
	0.2	10	Pen	2330.1	0.996	2331	1 B cs	2335.9	1.623	2331	1 B cs	2335.9	4.281	2331	1 B cs
			N-P	2338.3		2331	1 B cs	1439.6		1326	2 C ff	545.7		512	2 C ff
	0.2	30	Pen	833.4	0.995	835	1 B cs	834.2	0.997	835	1 B cs	833.9	1.561	835	1 B cs
			N-P	837.2		835	1 B cs	836.4		835	1 B cs	534.1		512	2 C ff
	0.2	50	Pen	506.4	0.995	508	1 B cs	507.7	0.989	508	1 B cs	507.3	1.022	508	1 B cs
			N-P	508.9		508	1 B cs	513.2		508	1 B cs	496.5		512	2 C ff

#### 4.4.3 Conclusion double-sided compression and tension

For CHS X-joints loaded in double-sided compression or tension, penetration of the chord by a continuous brace, may decrease the load on the connection and the chord, as this load is now directly transferred through the brace to obtain equilibrium with the force on the opposite end of the brace. This assumption is confirmed by the change in governing failure mechanism that is observed for the grey shaded models in Table 12 and Table 13. From these tables it can be concluded that joint failures are not governing for models subjected to double-sided tension or compression in which the chord is penetrated by a continuous brace and therefore, the EC design rules for joint failures must be omitted. These design rules, for chord face failure and punching shear failure, would otherwise underestimate the plastic capacity of the penetrated models significantly.

In Table 11, it can be seen that the models with upper limit parameter values, as well as the models with lower limit parameter values, fail in brace cross-section failure. From this it can be concluded that also the models with parameters values between those limits, that are initially not simulated, fail in brace cross-section failure. Therefore it is concluded that no additional parameter configurations need to be simulated.

Concludingly it is stated that the basic cross-section design rules from the EC, can be applied for penetrated CHS X-joints subjected to double-sided compression and tension and that the EC design rules for joint failures of non-penetrated CHS X-joints, should be omitted in these calculations. The current set of design rules in the EC does otherwise not predict the governing failure mechanism correctly, which may result in an underestimation of the plastic capacity by a factor 1.25 till 35.8.

### 4.5 SINGLE-SIDED COMPRESSION AND TENSION ( $F_x$ )

#### 4.5.1 Penetrated CHS X-joint FEA results

In Figure 37, a representation of a penetrated CHS X-joint subjected to single-sided compression and tension (by a force in X-direction) is shown. In Table 14 the FEA results are shown. It can be seen that a significant part of the geometries fail in basic cross-section failures, i.e. in brace cross-section and chord bending moment failure, while the remaining geometries, in Table 14 shaded in dark grey, fail due to chord face failure. When for those geometries the yield load obtained with the FEA is compared to the plastic design resistance calculated from the EC design rule for chord face failure, it can be seen that the true plastic capacity according to FEA is 1.69 till 4.97 times higher than predicted with the existing EC design rule. The plastic capacity of the geometries failing in basic cross section failures, on the other hand, are approximated very well by the EC design rules.

Similar to the geometries subjected to double-sided tension and compression, the difference in joint behavior and the FEA results between models subjected to single-sided compression or tension, is very limited and therefore, additional simulations are only executed for models subjected to tension. The extra simulations are done for the parameter configuration with  $\beta$  factors of 0.4 and 0.6, to create an extended overview in which the boundaries of the critical areas for geometries failing on chord face failure can be identified. In general, chord face failure is observed for joints with a higher  $2\gamma$  factors, for both models subjected to tension, as well as compression.

#### 4.5.2 Comparison penetrated and non-penetrated results

Table 15 and Table 16 show the results of the comparison between penetrated and non-penetrated FEA results, for models subjected to single-sided compression (Table 16) and tension (Table 15). Similar as in Table 14, in Table 15 and Table 16 the data, associated with the parameter configurations for which the penetrated geometry fails due to chord face failure, is shaded in dark grey. Additionally, the data associated with the parameter configurations for which merely the non-penetrated geometry fails due to chord face failure, is shaded in light grey in these tables. From the ratio between the plastic capacity (according to the FEA), P/N-P, it is observed that for these parameter configurations, shaded in light grey, the plastic capacity of the penetrated models is increased by a factor of approximately 1.07 till 2.49 compared to their non-penetrated equivalents. For the parameter configurations shaded in dark grey, for which both the penetrated and non-penetrated models fail in chord face failure, an increase in the plastic capacity of the penetrated geometries by a factor of approximately 1.04 till 3.15

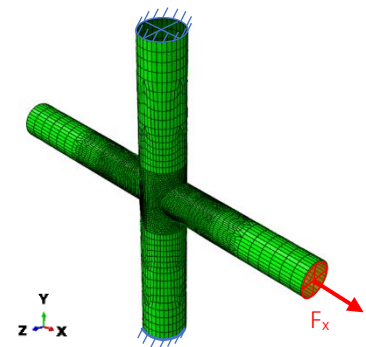


Figure 37: X-joint subjected to single-sided tension ( $F_x$ )

compared to their non-penetrated equivalents is observed. This increase in plastic capacity is especially observed for parameter configurations for which either the non-penetrated geometry or both the non-penetrated and the penetrated geometries are failing in chord face failure, which is more often the case for  $2\gamma$  factors of 30 and 50. For the other, non-shaded parameter configurations, both the penetrated and non-penetrated geometries fail in one of the basic cross-section failures, which can be accurately approximated by the existing set of EC design rules.

Table 14: FEA results penetrated model – single-sided compression and tension ( $F_x$ )

Model		$2\gamma$ 10				$2\gamma$ 30				$2\gamma$ 50				
Load	$\beta$	$2\delta$	$F_{x,FEA}$ (kN)	$F_{x,Rd}$ (kN)	RR	Failure mech.	$F_{x,FEA}$ (kN)	$F_{x,Rd}$ (kN)	RR	Failure mech.	$F_{x,FEA}$ (kN)	$F_{x,Rd}$ (kN)	RR	Failure mech.
Single-sided compression ( $F_x$ )	0.8	10	20146.9	19724	1.021	1 C bm	8529.7	7557	1.129	1 C bm	5126.5	4659	1.100	1 C bm
	0.8	30	13366.1	13354	1.001	1 B cs	6312.1	3383	1.866	3 C ff	4449.6	1218	3.653	3 C ff
	0.8	50	8128.5	8123	1.001	1 B cs	5699.8	3383	1.685	3 C ff	3850.9	1218	3.165	3 C ff
	0.2	10	2336.7	2331	1.002	1 B cs	2333.4	2331	1.001	1 B cs	1165.5	512	2.276	3 C ff
	0.2	30	834.8	835	1.000	1 B cs	837.6	835	1.003	1 B cs	822.3	835	0.985	1 B cs
	0.2	50	508.4	508	1.001	1 B cs	509.4	508	1.003	1 B cs	504.0	508	0.992	1 B cs
Single-sided tension ( $F_x$ )	0.8	10	20221.3	19724	1.025	1 C bm	8742.3	7557	1.157	1 C bm	5040.2	4659	1.082	1 C bm
	0.8	30	13369.4	13354	1.001	1 B cs	6575.6	3383	1.944	3 C ff	4361.5	1218	3.581	3 C ff
	0.8	50	8125.6	8123	1.000	1 B cs	5752.6	3383	1.700	3 C ff	3789.7	1218	3.111	3 C ff
	0.6	10	20373.1	20321	1.003	1 C bm	8019.2	2317	3.461	3 C ff	4147.2	834	4.973	3 C ff
	0.6	30	7514.8	7512	1.000	1 B cs	6540.1	2317	2.823	3 C ff	4028.7	834	4.831	3 C ff
	0.6	50	4574.2	4569	1.001	1 B cs	4554.5	4569	0.997	1 B cs	3557.8	834	4.266	3 C ff
	0.4	10	9333.6	9325	1.001	1 B cs	5500.2	1762	3.122	3 C ff	2388.2	634	3.767	3 C ff
	0.4	30	3341.8	3339	1.001	1 B cs	3348.4	3339	1.003	1 B cs	2124.8	634	3.351	3 C ff
	0.4	50	2032.1	2031	1.001	1 B cs	2029.0	2031	0.999	1 B cs	2032.1	634	3.205	3 C ff
	0.2	10	2331.0	2331	1.000	1 B cs	2345.1	2331	1.006	1 B cs	1178.1	512	2.301	3 C ff
	0.2	30	833.6	835	0.998	1 B cs	843.0	835	1.010	1 B cs	837.9	835	1.003	1 B cs
	0.2	50	507.8	508	1.000	1 B cs	509.3	508	1.003	1 B cs	520.5	508	1.010	1 B cs

Table 15: Comparison penetrated and non-penetrated results single-sided tension ( $F_x$ )

Model		$2\gamma$ 10				$2\gamma$ 30				$2\gamma$ 50					
L	$\beta$	$2\delta$	M	$F_{x,FEA}$ (kN)	P/N-P	$F_{x,Rd}$ (kN)	Fail. mech.	$F_{x,FEA}$ (kN)	P/N-P	$F_{x,Rd}$ (kN)	Fail. mech.	$F_{x,FEA}$ (kN)	P/N-P	$F_{x,Rd}$ (kN)	Fail. mech.
Single-sided tension ( $F_x$ )	0.8	10	Pen	20221.3	0.845	19724	1 C bm	8742.3	1.514	7557	1 C bm	5040.2	2.113	4659	1 C bm
			N-P	23943.3		19724	1 C bm	5774.8		3383	2 C ff	2385.1		1218	2 C ff
	0.8	30	Pen	13369.4	0.999	13354	1 B cs	6575.6	1.094	3383	3 C ff	4361.5	1.668	1218	3 C ff
			N-P	13378.9		13354	1 B cs	6010.4		3383	2 C ff	2615.0		1218	2 C ff
	0.8	50	Pen	8125.6	0.997	8123	1 B cs	5752.6	1.020	3383	3 C ff	3789.7	1.467	1218	3 C ff
			N-P	8152.9		8123	1 B cs	5638.8		3383	2 C ff	2582.6		1218	2 C ff
	0.6	10	Pen	20373.1	0.999	20321	1 C bm	8019.2	2.524	2317	3 C ff	4147.2	3.148	834	3 C ff
			N-P	21053.7		20321	1 C bm	3176.6		2317	2 C ff	1317.2		834	2 C ff
	0.6	30	Pen	7514.8	0.998	7512	1 B cs	6540.1	2.086	2317	3 C ff	4028.7	2.918	834	3 C ff
			N-P	7533.1		7512	1 B cs	3134.9		2317	2 C ff	1380.6		834	2 C ff
	0.6	50	Pen	4574.2	0.997	4569	1 B cs	4554.5	1.571	4569	1 B cs	3557.8	2.648	834	3 C ff
			N-P	4586.8		4569	1 B cs	2899.3		2317	2 C ff	1343.7		834	2 C ff
	0.4	10	Pen	9333.6	0.998	9325	1 B cs	5500.2	2.480	1762	3 C ff	2388.2	3.033	634	3 C ff
			N-P	9353.1		9325	1 B cs	2218.2		1762	2 C ff	787.4		634	2 C ff
	0.4	30	Pen	3341.8	0.998	3339	1 B cs	3348.4	1.567	3339	1 B cs	2124.8	3.041	634	3 C ff
			N-P	3346.8		3339	1 B cs	2136.2		1762	2 C ff	698.7		634	2 C ff
	0.4	50	Pen	2032.1	0.997	2031	1 B cs	2029.0	1.083	2031	1 B cs	2032.1	3.015	634	3 C ff
			N-P	2037.6		2031	1 B cs	1874.2		1762	2 C ff	674.0		634	2 C ff
0.2	10	Pen	2331.0	0.997	2331	1 B cs	2345.1	1.543	2331	1 B cs	1178.1	1.784	512	3 C ff	
		N-P	2339.1		2331	1 B cs	1519.4		1421	2 C ff	660.2		512	2 C ff	
0.2	30	Pen	833.6	0.995	835	1 B cs	843.0	0.996	835	1 B cs	837.9	1.306	835	1 B cs	
		N-P	837.6		835	1 B cs	846.2		835	1 B cs	641.8		512	2 C ff	
0.2	50	Pen	507.8	0.991	508	1 B cs	509.3	0.994	508	1 B cs	513.1	1.005	508	1 B cs	
		N-P	512.4		508	1 B cs	512.6		508	1 B cs	510.8		508	1 B cs	

Table 16: Comparison penetrated and non-penetrated results single-sided compression ( $F_x$ )

Model				2γ 10				2γ 30				2γ 50			
L	β	2δ	M	$F_{x,FEA}$ (kN)	P/N-P	$F_{x,Rd}$ (kN)	Fail. mech.	$F_{x,FEA}$ (kN)	P/N-P	$F_{x,Rd}$ (kN)	Fail. mech.	$F_{x,FEA}$ (kN)	P/N-P	$F_{x,Rd}$ (kN)	Fail. mech.
Single-sided compression ( $F_x$ )	0.8	10	Pen N-P	20146.9	0.852	19724	1 C bm	8529.7	1.707	7557	1 C bm	5126.5	2.488	4659	1 C bm
				23655.6		19724	1 C bm	4997.3		3383	2 C ff	2060.3		1218	2 C ff
	0.8	30	Pen N-P	13366.1	1.000	13354	1 B cs	6312.1	1.146	3383	3 C ff	4449.6	1.910	1218	3 C ff
				13361.4		13354	1 B cs	5509.9		3383	2 C ff	2329.5		1218	2 C ff
	0.8	50	Pen N-P	8128.5	1.000	8123	1 B cs	5699.8	1.038	3383	3 C ff	3850.9	1.644	1218	3 C ff
				8126.7		8123	1 B cs	5490.3		3383	2 C ff	2341.8		1218	2 C ff
	0.2	10	Pen N-P	2336.7	1.003	2331	1 B cs	2333.4	1.752	2331	1 B cs	1165.5	2.333	529	3 C ff
				2329.7		2331	1 B cs	1332.0		1326	2 C ff	499.6		529	2 C ff
	0.2	30	Pen N-P	834.8	1.001	835	1 B cs	837.6	1.002	835	1 B cs	822.3	1.663	835	1 B cs
				834.1		835	1 B cs	835.6		835	1 B cs	494.5		529	2 C ff
	0.2	50	Pen N-P	508.4	1.003	508	1 B cs	509.4	1.003	508	1 B cs	504.0	1.071	508	1 B cs
				507.0		508	1 B cs	507.7		508	1 B cs	470.4		529	2 C ff

#### 4.5.3 Conclusion single-sided compression and tension

From the above described observations, it is firstly concluded that for penetrated CHS X-joints failing in basic cross-section failures, the design resistance as calculated by the existing EC design rules (for basic cross-section failures) approximates the plastic capacity of these joints according to FEA very well. Secondly, it is however concluded that, in contrast to what is stated for CHS X-joints subjected to double-sided compression or tension, joint failures should not be omitted when calculating the design resistance of penetrated CHS X-joints subjected to single-sided compression or tension, since for some parameter configurations (shaded in dark grey in Table 14, Table 15 and Table 16), joint failures actually are governing. For these penetrated joint configurations, failing in chord face failure, the plastic capacity is not properly predicted with the existing EC design rule for chord face failure for non-penetrated joints and a new design rule to calculate the design resistances of the penetrated CHS X-joints failing in chord face failure is required. This is indicated by the Resistance Ratio (RR) in Table 14, from which it can be seen that the plastic capacity of these joints according to the FEA, is between 1.69 till 4.97 times higher than the design resistance calculated with the existing EC design rule for the governing failure mechanism as observed in FEA.

When comparing the FEA plastic capacity of these penetrated CHS X-joints (shaded in dark grey and failing in Cff) with their non-penetrated equivalents, it is seen from the P/N-P ratio in Table 15 and Table 16, that the FEA yield loads of the penetrated joints is 1.04 till 3.15 times higher than the yield loads of their non-penetrated equivalents. This increase in capacity of the penetrated geometries is slightly lower than the increase suggested by the resistance ratio (RR), since for the P/N-P ratio the FEA capacity of penetrated and non-penetrated geometries are compared, and thus the conservativeness of the existing EC design rules for non-penetrated geometries is omitted.

Thirdly, it is observed that for parameter configurations for which another governing failure mechanism is observed for the penetrated geometries compared to their non-penetrated equivalents, which are shaded in light grey in Table 15 and Table 16, the FEA yield loads for penetrated models are 1.07 till 2.49 times higher than the FEA yield loads of their non-penetrated equivalents. Finally, only a little difference is observed between the yield loads of models subjected to single-sided compression and tension, and it is therefore concluded that a design rule based on models subjected to single-sided tension will also be suitable for models subjected to single-sided compression.



## 4.6 BENDING MOMENT ABOUT THE Y- ( $M_y$ ) AND Z- ( $M_z$ ) AXIS

### 4.6.1 Penetrated CHS X-joint FEA results

In Figure 38, a representation of a penetrated CHS X-joint subjected to a bending moment applied on the brace, about the Y- ( $M_y$ ) or Z- ( $M_z$ ) axis, is shown. The FEA results for these joints are shown in Table 17, in which it can be seen that the geometries from all analyzed parameter configurations fail due to the basic cross-section failure mechanisms brace bending moment (1 B bm) and chord torsional moment (1 C tm). Moreover, it can be seen that the resistance ratio (RR) approximates 1 for all geometries, from which it can be concluded that the plastic design resistance can be calculated with the existing basic cross-section design rules from the EC and that no additional design rules are required for penetrated CHS X-joints subjected to this load case.

### 4.6.2 Comparison non-penetrated and penetrated results

In Table 18 and Table 19, the comparison between the FEA results of the penetrated and non-penetrated CHS X-joints subjected to a bending moment about the Y- (Table 18) or Z- (Table 19) axis, is presented. In the tables can be seen that for several non-penetrated geometries, which are shaded in light grey, chord face failure is governing. However, for their equivalent penetrated geometries, the basic cross-section failure mechanisms are governing and due to this shift in governing failure mechanism, their plastic capacity observed in FEA are approximately 1.21 till 12.1 times higher than the observed plastic capacity of their non-penetrated equivalents.

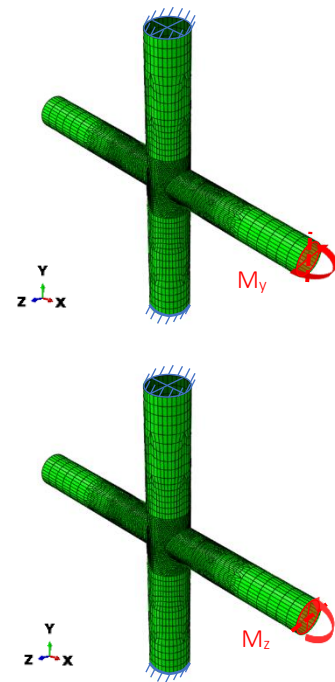


Figure 38: X-joint subjected to a bending moment about the Y- or Z-axis

Table 17: FEA results penetrated model – bending moment about the Y- ( $M_y$ ) and Z- ( $M_z$ ) axis

Model	2γ 10				2γ 30				2γ 50			
	Load	$\beta$	$2\delta$	Failure mech.	$M_{y,z,FEA}$ (kNm)	$M_{y,z,Rd}$ (kNm)	RR	Failure mech.	$M_{y,z,FEA}$ (kNm)	$M_{y,z,Rd}$ (kNm)	RR	Failure mech.
Bending moment about Y-axis ( $M_y$ )	0.8	10		1 B bm	6567.8	6541	1.004	1 B bm	4723.4	4646	1.017	1 C tm
	0.8	30		1 B bm	2502.5	2506	0.999	1 B bm	2505.2	2506	1.000	1 B bm
	0.8	50		1 B bm	1539.7	1545	0.997	1 B bm	1539.6	1545	0.997	1 B bm
	0.2	10		1 B bm	101.7	102	0.997	1 B bm	102.8	102	1.008	1 B bm
	0.2	30		1 B bm	39.1	39	1.003	1 B bm	39.2	39	1.005	1 B bm
	0.2	50		1 B bm	23.9	24	0.996	1 B bm	24.0	24	1.000	1 B bm
Bending moment about Z-axis ( $M_z$ )	0.8	10		1 B bm	6533.5	6541	0.999	1 B bm	6533.0	6541	0.999	1 B bm
	0.8	30		1 B bm	2501.8	2506	0.998	1 B bm	2513.1	2506	1.003	1 B bm
	0.8	50		1 B bm	1537.3	1545	0.995	1 B bm	1533.7	1545	0.993	1 B bm
	0.2	10		1 B bm	102.1	102	1.001	1 B bm	102.0	102	1.000	1 B bm
	0.2	30		1 B bm	39.2	39	1.005	1 B bm	39.0	39	1.000	1 B bm
	0.2	50		1 B bm	24.1	24	1.004	1 B bm	24.0	24	1.000	1 B bm

Table 18: Comparison penetrated and non-penetrated results bending moment about the Y-axis ( $M_y$ )

Model	2γ 10				2γ 30				2γ 50							
	L	$\beta$	$2\delta$	M	$M_{y,FEA}$ (kNm)	P/N-P	$M_{y,Rd}$ (kNm)	Fail. mech.	$M_{y,FEA}$ (kNm)	P/N-P	$M_{y,Rd}$ (kNm)	Fail. mech.	$M_{y,FEA}$ (kNm)	P/N-P	$M_{y,Rd}$ (kNm)	Fail. mech.
Bending moment about the Y-axis ( $M_y$ )	0.8	10	Pen	N-P	6567.8	1.024	6541	1 B bm	6572.0	5.983	6541	1 B bm	4723.4	12.046	4646	1 C tm
					6415.5		5804	1 C ps	1098.4		1071	2 C ff	392.1		386	2 C ff
	0.8	30	Pen	N-P	2502.5	1.002	2506	1 B bm	2521.4	2.293	2506	1 B bm	2505.2	6.265	2506	1 B bm
					2497.7		2506	1 B bm	1099.5		1071	2 C ff	399.9		386	2 C ff
	0.8	50	Pen	N-P	1539.7	1.000	1545	1 B bm	1541.9	1.407	1545	1 B bm	1539.6	3.907	1545	1 B bm
					1539.6		1545	1 B bm	1096.1		1071	2 C ff	394.1		386	2 C ff
0.2	10	Pen	N-P	101.7	0.999	102	1 B bm	102.0	0.999	102	1 B bm	102.8	2.544	102	1 B bm	
				101.8		102	1 B bm	102.1		102	1 B bm	40.4		40	2 C ff	
0.2	30	Pen	N-P	39.1	0.995	39	1 B bm	39.1	0.995	39	1 B bm	39.2	1.002	39	1 B bm	
				39.3		39	1 B bm	39.3		39	1 B bm	39.1		39	1 B bm	
0.2	50	Pen	N-P	23.9	0.999	24	1 B bm	24.0	0.999	24	1 B bm	24.0	1.000	24	1 B bm	
				23.9		24	1 B bm	24.0		24	1 B bm	24.0		24	1 B bm	

Table 19: Comparison penetrated and non-penetrated results bending moment about the Z-axis ( $M_z$ )

Model				2 $\gamma$ 10				2 $\gamma$ 30				2 $\gamma$ 50			
L	$\beta$	2 $\delta$	M	$M_{z,FEA}$ (kNm)	P/N-P	$M_{z,Rd}$ (kNm)	Fail. mech.	$M_{z,FEA}$ (kNm)	P/N-P	$M_{z,Rd}$ (kNm)	Fail. mech.	$M_{z,FEA}$ (kNm)	P/N-P	$M_{z,Rd}$ (kNm)	Fail. mech.
Bending moment about the Z-axis ( $M_z$ )	0.8	10	Pen N-P	6533.5	0.990	6541	1 B bm	6533.0	3.145	6541	1 B bm	6533.0	6.711	6541	1 B bm
				6596.5		6541	1 B bm	2077.1		2098	2 C ff	978.1		975	2 C ff
	0.8	30	Pen N-P	2501.8	1.001	2506	1 B bm	2513.1	1.209	2506	1 B bm	2513.1	2.542	2506	1 B bm
				2498.5		2506	1 B bm	2078.5		2098	2 C ff	993.2		975	2 C ff
	0.8	50	Pen N-P	1537.3	1.003	1545	1 B bm	1533.7	0.994	1545	1 B bm	1533.7	1.590	1545	1 B bm
				1533.0		1545	1 B bm	1542.5		1545	1 B bm	975.6		975	2 C ff
	0.2	10	Pen N-P	102.1	1.004	102	1 B bm	102.1	0.991	102	1 B bm	102.1	1.889	102	1 B bm
				101.7		102	1 B bm	103.1		102	1 B bm	54.0		61	2 C ff
	0.2	30	Pen N-P	39.2	1.006	39	1 B bm	39.1	1.005	39	1 B bm	39.1	1.005	39	1 B bm
				38.9		39	1 B bm	38.9		39	1 B bm	38.9		39	1 B bm
	0.2	50	Pen N-P	24.1	1.005	24	1 B bm	24.0	1.001	24	1 B bm	24.0	1.002	24	1 B bm
				23.9		24	1 B bm	24.0		24	1 B bm	24.0		24	1 B bm

#### 4.6.3 Conclusion bending moment about the Y- ( $M_y$ ) and Z- ( $M_z$ ) axis

From the FEA of the geometries subjected to a bending moment about the Y- ( $M_y$ ) or Z- ( $M_z$ ) axis, it is concluded that no additional design rules are required for the calculation of the plastic design resistance of penetrated CHS X-joints. For the geometries of all simulated parameter configurations, brace bending moment or chord torsional moment is governing according to the FEA and the plastic capacity for these failure mechanisms are well approximated by the plastic design resistance calculated with the EC design rules (as follows from the RR). However, from the comparison between the penetrated and non-penetrated geometries, as given in Table 18 and Table 19, it is observed that for several penetrated geometries with higher 2 $\gamma$  factors and lower 2 $\delta$  factors, the plastic capacity (according to the FEA) from penetrated configurations ranges from 1.21 up till 12.1 times the plastic capacity of their non-penetrated equivalents. This increase in capacity is caused by the shift in governing failure mechanism that is observed in FEA; in contrast to non-penetrated geometries that fail in chord face failure, their equivalent penetrated geometries fail due to a basic cross-section failure. To ensure that these basic cross-section failures are also the governing failure mechanisms obtained while calculating the design resistance of a joint subjected to bending moment  $M_y$  or  $M_z$ , the design rules for joint failures, i.e. chord face failure and punching shear failure, should be omitted. This is also clearly visible in the two tables presented in each paragraph of Appendix F.5. In the first table, for each parameter configuration, the plastic design resistances according to all relevant EC design rules for non-penetrated joints are given and the minimum design resistance is selected as the governing (design) failure mechanism for non-penetrated geometries. The (governing) design resistance and (design) failure mechanism are then compared to the ones obtained from FEA. In the second table, the same is done for the penetrated geometries, and it can be seen that by omitting the EC design rules for joint failures, indeed the correct (i.e. in accordance with the observations in the FEA) governing plastic design resistance and failure mechanism are found. The tables shown in Appendix F.5 are further elaborated in Paragraph 5.2.1.3.

### 4.7 SHEAR $F_y$ (CHORD BENDING MOMENT)

#### 4.7.1 Penetrated CHS X-joint FEA results

Figure 39 shows a representation of the penetrated CHS X-joint subjected to a shear force in the Y-direction ( $F_y$ ), which also induces a small bending moment in the brace and the chord. Bending moment on the brace is kept as small as possible by reducing the eccentricity of the force to be applied. Initially, only the geometrical parameter configurations with  $\beta$  factor 0.8 and 0.2 were simulated, to identify possible critical areas for which joint failures are governing. From this FEA, from which the results are shown in Table 20, chord face failure was observed as the governing failure mechanism for the geometries with  $\beta$  0.8 – 2 $\gamma$  30/50 – 2 $\delta$  10, and therefore, additional simulations with  $\beta$  factors 0.6 and 0.4 are performed. The parameter

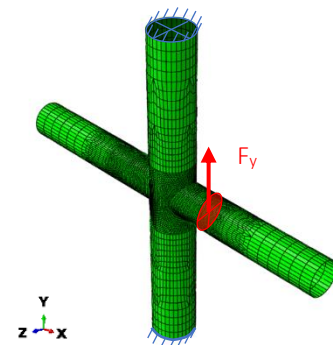


Figure 39: X-joint subjected to shear in Y-direction ( $F_y$ )

configurations used for the additional simulations are selected based on the chance that the geometry fails in chord face failure and to ensure the boundaries of the critical areas for models subjected to shear  $F_y$  are identified. For the additional calculations, chord face failure is only governing for the geometry  $\beta$  0.6 –  $2\gamma$  50 –  $2\delta$  10. For the geometries failing in chord face failure, a plastic capacity is observed that is 4.46 till 7.59 times higher than the plastic design resistance obtained with the existing EC design rules, causing the true capacity of the joint to be underestimated significantly. It would therefore be interesting to create a new design rule for penetrated CHS X-joints subjected to shear force in longitudinal direction of the chord ( $F_y$ ). For the other simulated parameter configurations, bending moment of the brace is governing, for which the plastic design resistance can be calculated well with the existing EC design rules, as can be seen from the resistance ratios in Table 20.

#### 4.7.2 Comparison non-penetrated and penetrated results

In Table 21, the comparison between penetrated and non-penetrated FEA results, for models subjected to shear  $F_y$  (chord bending moment) are shown. In the results can be seen that a substantial part of the non-penetrated geometries with  $2\gamma$  factor 30 and 50, fail in chord face failure, while only three of their penetrated equivalents fail in chord face failure. Comparisons between the penetrated and the non-penetrated FEA results (P/N-P) show that for the light grey shaded configurations, the penetrated X-joints have a plastic capacity of 1.30 till 6.03 times the plastic capacity from their non-penetrated equivalents. This difference in plastic capacity is due to the continuous brace that penetrates the chord, resulting in an increased resistance to chord face failure and for some configurations, causes a shift in the governing failure mechanism; non-penetrated X-joints fail in chord face failure, while the associated penetrated X-joints fail due to the bending moment in the brace for the configurations shaded in light grey. For the configurations shaded in dark grey, for which both penetrated and non-penetrated joints are failing in chord face failure, the penetrated geometries have a plastic capacity between 3.95 till 5.82 as high as the plastic capacity of their non-penetrated equivalents. For the non-shaded configurations the non-penetrated and the penetrated X-joints fail in bending moment of the brace and these plastic capacity can be approximated well by the plastic design resistances from the EC design rules, as again can be seen from the RR.

#### 4.7.3 Conclusion shear $F_y$ (chord bending moment)

For models subjected to shear  $F_y$  (chord bending moment), it can be concluded that for penetrated geometries failing in the basic cross-section failures, the plastic capacity can be approximated well by the plastic design resistances from the EC design rules. However, for penetrated geometries failing in chord face failure, which in Table 20 and Table 21 are shaded dark grey, or penetrated models failing in a basic cross-section failure, for which the non-penetrated equivalent fails in chord face failure, which in Table 21 are shaded in light grey, the yield load is not predicted properly by the current set of EC design rules for non-penetrated and therefore, new design rules are required. For penetrated geometries failing in chord face failure, a plastic capacity between 4.46 till 7.59 times the design resistance obtained with the existing EC design rules is observed. Comparing the FEA results of penetrated joints for which a shift in failure mechanism is observed with the results of the associated non-penetrated joints, plastic capacity that are 1.30 till 6.30 times higher than their non-penetrated equivalents are obtained.

Table 20: FEA results penetrated model – shear  $F_y$  (chord bending moment)

Model		$2\gamma$ 10				$2\gamma$ 30				$2\gamma$ 50			
Load	$\beta$ 2 $\delta$	$F_{y,FEA}$ (kN)	$F_{y,Rd}$ (kN)	RR	Failure mech.	$F_{y,FEA}$ (kN)	$F_{y,Rd}$ (kN)	RR	Failure mech.	$F_{y,FEA}$ (kN)	$F_{y,Rd}$ (kN)	RR	Failure mech.
Shear $F_y$ (chord bending moment)	0.8 10	12553.5	11332	1.108	1 B bm	11165.0	2503	4.461	3 C ff	6380.1	1163	5.486	3 C ff
	0.8 30	4327.9	4342	0.997	1 B bm	4404.5	4342	1.014	1 B bm	4350.0	4342	1.002	1 B bm
	0.8 50	2597.9	2677	0.970	1 B bm	2613.6	2677	0.976	1 B bm	2595.8	2677	0.970	1 B bm
	0.6 10					6491.8	5637	1.152	1 B bm	5255.9	692	7.595	3 C ff
	0.6 30					2303.0	2160	1.066	1 B bm	2373.8	2160	1.099	1 B bm
	0.4 10					2596.8	2322	1.118	1 B bm	2613.5	2322	1.126	1 B bm
	0.2 10	513.9	559	0.919	1 B bm	583.7	559	1.044	1 B bm	590.6	559	1.057	1 B bm
	0.2 30	183.2	214	0.856	1 B bm	207.4	214	0.969	1 B bm	207.7	214	0.971	1 B bm
	0.2 50	107.1	132	0.811	1 B bm	123.5	132	0.936	1 B bm	126.8	132	0.961	1 B bm

Table 21: Comparison penetrated and non-penetrated results shear  $F_y$  (chord bending moment)

Model	2γ 10				2γ 30				2γ 50						
	L	β	2δ	M	$F_{y,FEA}$ (kN)	P/N-P	$F_{y,Rd}$ (kN)	Fail. mech.	$F_{y,FEA}$ (kN)	P/N-P	$F_{y,Rd}$ (kN)	Fail. mech.	$F_{y,FEA}$ (kN)	P/N-P	$F_{y,Rd}$ (kN)
Shear $F_y$ (chord bending moment)	0.8	10	Pen N-P	12553.5	1.000	11332	1 B bm	11165.0	3.947	2503	3 C ff	6380.1	4.020	1163	3 C ff
				12552.4		11332	1 B bm	2829.1		2503	2 C ff	1587.1		1163	2 C ff
	0.8	30	Pen N-P	4327.9	0.997	4342	1 B bm	4404.5	1.528	4342	1 B bm	4350.0	2.726	4342	1 B bm
				4342.7		4342	1 B bm	2882.4		2503	2 C ff	1595.7		1163	2 C ff
	0.8	50	Pen N-P	2597.9	0.999	2677	1 B bm	2613.6	1.056	2677	1 B bm	2595.8	1.676	2677	1 B bm
				2600.8		2677	1 B bm	2475.7		2503	2 C ff	1548.5		1163	2 C ff
	0.6	10	Pen N-P					6491.8	3.873	5637	1 B bm	5255.9	5.815	692	3 C ff
								1721.2		1489	2 C ff	903.8		692	2 C ff
	0.6	30	Pen N-P					2303.0	1.301	2160	1 B bm	2373.8	2.625	2160	1 B bm
								1770.0		1489	2 C ff	904.2		692	2 C ff
	0.4	10	Pen N-P					2596.8	2.451	2322	1 B bm	2613.5	6.031	2322	1 B bm
								1059.6		748	2 C ff	433.3		348	2 C ff
0.2	10	Pen N-P	513.9	1.006	559	1 B bm	583.7	0.989	559	1 B bm	590.6	2.282	559	1 B bm	
			510.9		559	1 B bm	590.3		559	1 B bm	258.8		233	2 C ff	
0.2	30	Pen N-P	183.2	0.988	214	1 B bm	207.4	1.001	214	1 B bm	207.7	0.917	214	1 B bm	
			185.5		214	1 B bm	207.2		214	1 B bm	226.6		214	1 B bm	
0.2	50	Pen N-P	107.1	0.984	132	1 B bm	123.5	0.992	132	1 B bm	126.8	1.013	132	1 B bm	
			108.9		132	1 B bm	124.5		132	1 B bm	125.2		132	1 B bm	

## 4.8 SHEAR $F_z$ (CHORD TORSIONAL MOMENT)

### 4.8.1 Penetrated CHS X-joint FEA results

A representation of the penetrated CHS X-joint subjected to a shear force in the Z-direction ( $F_z$ ), which induces a small bending moment on the brace and a torsional moment in the chord, is shown in Figure 40, and the FEA results are shown in Table 22. Initially, only the geometrical parameters with  $\beta$  0.8 and 0.2 were simulated, for which only the geometries  $\beta$  0.8 –  $2\gamma$  30/50 –  $2\delta$  10 and  $\beta$  0.8 –  $2\gamma$  50 –  $2\delta$  30 fail in chord face failure. Therefore, additional simulations for geometries with  $\beta$  factors 0.6 and 0.4 are performed, which are selected based on the critical area for the geometries where chord face failure may occur. For the additional calculations, chord face failure is only governing for the geometrical parameter  $\beta$  0.6 –  $2\gamma$  50 –  $2\delta$  10. For the geometries failing in chord face failure, the FEA predicts a plastic capacity of 4.68 till 11.9 times higher than the plastic design resistance predicted by the EC for non-penetrated geometries. For the other simulated geometrical parameters, bending moment of the brace is governing, for which the plastic capacity is well predicted with the existing EC design rules.

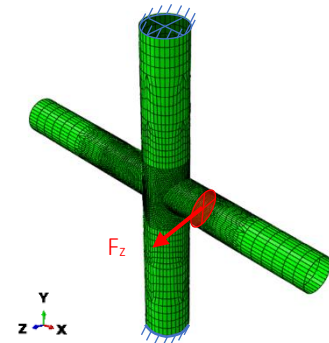


Figure 40: X-joint subjected to shear in Z-direction ( $F_z$ )

Table 22: FEA results penetrated model – shear  $F_z$  (chord torsional moment)

Model	2γ 10				2γ 30				2γ 50			
	Load	β	2δ		$F_{z,FEA}$ (kN)	$F_{z,Rd}$ (kN)	RR	Failure mech.	$F_{z,FEA}$ (kN)	$F_{z,Rd}$ (kN)	RR	Failure mech.
Shear $F_z$ (chord torsional moment)	0.8	10			11467.4	11332	1.012	1 B bm	5979.6	1278	4.679	3 C ff
					4165.5	4342	0.959	1 B bm	4244.3	4342	0.977	1 B bm
	0.8	30			2479.8	2677	0.926	1 B bm	2552.9	2677	0.954	1 B bm
	0.6	10							5644.4	5637	1.001	1 B bm
	0.6	30							2155.5	2160	0.998	1 B bm
	0.4	10							2558.2	2322	1.102	1 B bm
	0.2	10			519.3	559	0.929	1 B bm	580.5	559	1.038	1 B bm
					189.7	214	0.886	1 B bm	216.7	214	1.013	1 B bm
0.2	30			112.8	132	0.855	1 B bm	133.0	132	1.008	1 B bm	
0.2	50											

Table 23: Comparison penetrated and non-penetrated results shear  $F_z$  (chord torsional moment)

Model				2 $\gamma$ 10				2 $\gamma$ 30				2 $\gamma$ 50			
L	$\beta$	2 $\delta$	M	$F_{z,FEA}$ (kN)	P/N-P	$F_{z,Rd}$ (kN)	Fail. mech.	$F_{z,FEA}$ (kN)	P/N-P	$F_{z,Rd}$ (kN)	Fail. mech.	$F_{z,FEA}$ (kN)	P/N-P	$F_{z,Rd}$ (kN)	Fail. mech.
Shear $F_z$ (chord torsional moment)	0.8	10	Pen	11467.4	1.011	11332	1 B bm	5979.6	2.945	1278	3 C ff	3575.7	4.136	460	3 C ff
			N-P	11346.4		11332	1 B bm	2030.3		1278	2 C ff	864.6		460	2 C ff
	0.8	30	Pen	4165.5	1.016	4342	1 B bm	4244.3	1.783	4342	1 B bm	3551.3	3.370	460	3 C ff
			N-P	4098.0		4342	1 B bm	2380.0		1278	2 C ff	1053.7		460	2 C ff
	0.8	50	Pen	2479.8	1.007	2677	1 B bm	2552.9	1.091	2677	1 B bm	2595.7	2.395	2677	1 B bm
			N-P	2462.3		2677	1 B bm	2339.2		1278	2 C ff	1083.9		460	2 C ff
	0.6	10	Pen					5644.4	5.906	5637	1 B bm	2986.1	7.815	250	3 C ff
			N-P					955.6		694	2 C ff	382.1		250	2 C ff
	0.6	30	Pen					2155.5	2.062	2160	1 B bm	2156.2	4.879	2160	1 B bm
			N-P					1045.5		694	2 C ff	441.9		250	2 C ff
	0.4	10	Pen					2558.2	3.891	2322	1 B bm	2341.8	9.806	2322	1 B bm
			N-P					657.5		398	2 C ff	238.8		143	2 C ff
0.2	10	Pen	519.3	0.996	559	1 B bm	580.5	1.330	559	1 B bm	569.3	3.082	559	1 B bm	
		N-P	521.4		559	1 B bm	436.7		199	2 C ff	184.7		72	2 C ff	
0.2	30	Pen	189.7	1.004	214	1 B bm	216.7	0.994	214	1 B bm	214.9	1.162	214	1 B bm	
		N-P	188.8		214	1 B bm	217.9		214	1 B bm	185.0		72	2 C ff	
0.2	50	Pen	112.8	0.997	132	1 B bm	133.0	1.000	132	1 B bm	131.6	1.014	132	1 B bm	
		N-P	113.1		132	1 B bm	133.0		132	1 B bm	129.8		132	1 B bm	

#### 4.8.2 Comparison non-penetrated and penetrated results

Table 23 shows the comparison between non-penetrated and penetrated FEA results, for models subjected to shear in the Z-direction ( $F_z$ ). The table shows that a substantial part of the non-penetrated models with 2 $\gamma$  factor 30 and 50, fail in chord face failure, while only four of their penetrated equivalents fail in chord face failure. A comparison between the penetrated and the non-penetrated results (P/N-P) shows that for the configurations shaded in light grey, the penetrated configurations have a plastic capacity between 1.09 till 9.81 higher than their non-penetrated equivalents, and for the configurations shaded in dark grey this is between 2.95 till 7.82. This increase in capacity is caused, as elaborated in the previous paragraphs on Shear in y-direction, due to penetration of the chord by a continuous brace, resulting in an increased strength of the joint. This causes for the penetrated X-joints with the parameters configurations shaded in light grey, a shift in governing failure mechanism compared to their non-penetrated equivalents; while the non-penetrated geometries fail in chord face failure, the penetrated geometries fail in bending moment of the brace. For the non-shaded geometries, the penetrated, as well as the non-penetrated X-joints, fail in bending moment of the brace.

#### 4.8.3 Conclusion shear $F_z$ (chord torsional moment)

For penetrated CHS X-joints subjected to shear  $F_z$  (chord torsional moment), the same can be concluded as for the load case shear  $F_y$ : it can be concluded that for geometries failing in the basic cross-section failures, the plastic capacity can be predicted well. However, for models failing in chord face failure, which in Table 22 are shaded in dark grey, or penetrated models failing in a basic cross-section failure, for which the non-penetrated equivalent fails in chord face failure, which in Table 23 are shaded in light grey, the plastic capacity is not predicted properly by the current set of EC design rules for non-penetrated joints and therefore, new design rules are required. For penetrated models failing in chord face failure, a plastic capacity between 4.68 till 11.9 higher compared to the existing EC design rules for non-penetrated joints can be obtained.

#### 4.9 CONCLUSION PARAMETER STUDY

In the presented parameter study, the load case and geometrical parameters  $\beta$ ,  $2\gamma$ , &  $2\delta$  have been varied. Initially only models with parameter configurations containing the limit values of these parameters have been simulated & analyzed and based on these results, additional parameter configurations are simulated, in order to identify the critical areas for which new design rules for penetrated X-joints are required. The parameter study is performed for the load cases “Double-sided compression and tension ( $F_x$ )”, “Single-sided compression and tension ( $F_x$ )”, “Bending moment about the Y-axis ( $M_y$ )”, “Bending moment about the Z-axis ( $M_z$ )”, “Shear  $F_y$  (chord bending moment)”, and “Shear  $F_z$  (chord torsional moment)”. The parameter study is performed for penetrated CHS X-joints, as well as for non-penetrated CHS X-joints, for which the FEA plastic capacity and calculated EC design resistance are compared to each other and the governing failure mechanisms obtained via both methods, as explained in Paragraph 4.2, are assigned and compared. The results are processed based on the procedure as explained in Paragraph 4.3.

From the parameter study can be concluded that for penetrated geometries subjected to double-sided compression and tension ( $F_x$ ), and bending moment about the Y- ( $M_y$ ) and Z- ( $M_z$ ) axis, the plastic capacity is approximated well by the basic cross-section design rules for CHS from the EC, and therefore, no new design rules are required. For the penetrated geometries subjected to double-sided compression and tension ( $F_x$ ), a plastic capacity of 1.25 till 35.8 times the plastic capacity of non-penetrated geometries is observed in FEA. It appears that, for the geometries under these loading conditions, the penetration of the chord by the increases the joint capacity to such an extent, that basic cross-section failures are observed as the governing failure mechanisms. The same holds for penetrated CHS X-joints subjected to bending moment about the Y- ( $M_y$ ) and Z- ( $M_z$ ) axis, for which a plastic capacity of 1.21 till 12.1 times the plastic capacity of their non-penetrated equivalents can be observed. For all penetrated geometries, subjected to one of the aforementioned load cases, joint failures are not governing and the design rules for non-penetrated joint failures, which are chord face failure and punching shear failure, should be omitted in the calculation of the joint capacity to predict the right failure mechanism and its corresponding plastic design resistance.

For penetrated geometries subjected to single-sided compression and tension ( $F_x$ ), shear  $F_y$  (chord bending moment), and shear  $F_z$  (chord torsional moment), several geometrical parameter configurations fail in chord face failure, and for these configurations, new design rules for penetrated CHS X-joints are recommended. Comparing the plastic capacity from penetrated geometries failing in chord face failure, with the calculated design resistances obtained with the existing EC design rules for non-penetrated joints, i.e. evaluating the RR, an increase in plastic capacity can be observed for:

- single-sided compression and tension ( $F_x$ ), of 1.69 till 4.97 times the EC plastic design resistance;
- shear  $F_y$  (chord bending moment), of 4.46 till 7.59 times the EC plastic design resistance;
- shear  $F_z$  (chord torsional moment), of 4.68 till 11.9 times the EC plastic design resistance.

Moreover, for the penetrated geometries that fail in basic cross-section failures under compression and tension ( $F_x$ ), shear  $F_y$  and shear  $F_z$ , an increase of the plastic capacity is observed in FEA by a factor 1.04 till 3.15, 1.30 till 6.30, and 1.09 till 9.81 with respect to their non-penetrated equivalents that fail in chord face failure, respectively. Due to these significant increases in plastic capacity, new design rules for penetrated joints that fit the plastic capacity from FEA are recommended for these three load cases ( $F_x$ ,  $F_y$  and  $F_z$ ).

## 5 DESIGN RULES

### 5.1 INTRODUCTION

From the parameter study it is concluded that for penetrated CHS X-joints subjected to double-sided compression and tension ( $F_x$ ), and bending moment about the Y- ( $M_y$ ) and Z- ( $M_z$ ) axis, the plastic capacity can be approximated well with the basic cross-section design rules from the EC, and therefore, no new design rules are required. However, for geometries subjected to single-sided compression and tension ( $F_x$ ), shear  $F_y$  (chord bending moment), and shear  $F_z$  (chord torsional moment), several geometrical parameter configurations fail in chord face failure for which the current design rules underestimate the yield loads significantly. For these configurations, new design rules for penetrated CHS X-joints are required. In this section, the created design rules and the steps to arrive at these design rules are elaborated. The failure mechanism that is governing according to these newly defined set of design rules is then verified with the governing failure mechanism as observed in FEA. In addition to the standard load cases, the behavior of CHS X-joints is analyzed for a combined load case and a check is performed for the combination of design rules, for which the basis is provided in the EC and in Equation 2.11. Finally, a calculation sheet for penetrated X-joints is created, in which a penetrated CHS X-joint subjected to a certain load is checked for brace and chord gross cross-section failures and the joint failures. A case study has been done to the mooring bollard from Witteveen+Bos.

### 5.2 SINGLE-SIDED COMPRESSION AND TENSION ( $F_x$ )

From the parameter study for models subjected to single-sided compression and tension ( $F_x$ ) provided in Paragraph 4.5, it is concluded that for the parameter configurations from Table 16 and Table 15 for which the results are outlined and shaded in dark grey, new design rules are required. For these geometries failing in chord face failure, the plastic capacity obtained by FEA are 1.04 till 3.15 times higher than the plastic design resistances calculated by the design rules from the EC for non-penetrated joints.

Initially, the results for penetrated configurations were reviewed and there was tried to create a design rule for penetrated CHS X-joints subjected to single-sided compression and tension ( $F_x$ ). However, a first attempt to create a suitable design rule was unsuccessful since a starting point for creating a design rule was missing. Therefore, first the existing chord face failure design rules for non-penetrated CHS X-joints were reviewed and compared with the corresponding FEA results and eventually, an improved design rule for non-penetrated CHS X-joints subjected to single-sided compression and tension ( $F_x$ ) is created. Improving the existing design rule for non-penetrated models failing in chord face failure was less complex because more results were available on which the design rule could be fitted. With this study to the EC design rules for non-penetrated joints, a solid foundation was laid for the development of the design rules for penetrated CHS X-joints.

Since geometries subjected to tension and compression give almost the same results and plastic capacity, there is chosen to work further with geometries subjected to single-sided tension, for which the design rules are created. The plastic capacity from the models subjected to compression are slightly lower, which is due to local buckling of the brace under compression.

#### 5.2.1 Non-penetrated X-joints

##### 5.2.1.1 Influence geometrical parameters on plastic capacity

For the non-penetrated geometries subjected to single-sided tension, first the results from the FEA are compared to each other and the influences of the geometrical parameters are identified. Table 24 shows the results for non-penetrated geometries subjected to single-sided tension and failing in chord face failure, where under "Model" the geometrical parameters  $\beta$ ,  $2\gamma$ , and  $2\delta$  are given, and for every geometry under "Results" the plastic capacity (yield load) from FEA, and the influences of the geometrical parameters on the results (infl.  $\beta$ , infl.  $2\gamma$ , and infl.  $2\delta$ ) are given. The influence ratios are calculated by dividing the plastic capacity from FEA of the higher order geometry through the plastic capacity of the lower order geometry, as for example shown in the formulas below:

$$\text{infl } \beta = \frac{\beta \ 0.8 - 2\gamma \ 30 - 2\delta \ 10}{\beta \ 0.6 - 2\gamma \ 30 - 2\delta \ 10}, \frac{\beta \ 0.8 - 2\gamma \ 30 - 2\delta \ 30}{\beta \ 0.6 - 2\gamma \ 30 - 2\delta \ 30}, \text{ etc.} \quad (5.21)$$

$$\text{infl } 2\gamma = \frac{\beta \ 0.8 - 2\gamma \ 30 - 2\delta \ 10}{\beta \ 0.8 - 2\gamma \ 50 - 2\delta \ 10}, \frac{\beta \ 0.8 - 2\gamma \ 30 - 2\delta \ 30}{\beta \ 0.8 - 2\gamma \ 50 - 2\delta \ 30}, \text{ etc.} \quad (5.22)$$

$$\text{infl } 2\delta = \frac{\beta \ 0.8 - 2\gamma \ 30 - 2\delta \ 10}{\beta \ 0.8 - 2\gamma \ 30 - 2\delta \ 30}, \frac{\beta \ 0.8 - 2\gamma \ 30 - 2\delta \ 30}{\beta \ 0.8 - 2\gamma \ 30 - 2\delta \ 50}, \text{ etc.} \quad (5.23)$$

The identify the influence of the factor  $\beta$ , the factor  $\beta$  is varied and the  $2\gamma$  and  $2\delta$  factors are kept equal. The same holds for the calculation of the influence of  $2\gamma$  and the influence of  $2\delta$ , where the factor  $2\gamma$  is varied and the  $\beta$  and  $2\delta$  factors are kept equal and the factor  $2\delta$  is varied and the  $\beta$  and  $2\gamma$  factors are kept equal, respectively.

In the right part of Table 24, the joint capacity as calculated with two existing EC design rules and two adjusted design rules are provided, where for every design rule, the calculated yield load ( $N_{1,pl,Rd}$ ) and resistance ratio (RR) are shown. For the RR, the plastic capacity, as obtained by FEA, is divided by the plastic design resistance obtained with the evaluated design rule, which means that for RR's above 1.0, the design rule is on the safe side since the true capacity of the joint, as obtained by the FEA, is higher than the capacity calculated using the design rule. If the RR is below 1.0, a plastic design resistance is obtained with the design rule, that is higher than the plastic capacity found in FEA and the design rule is unsafe. In Table 24, conservative results with a RR above 1.3 are marked with a grey line about their results and geometries with a RR less than 0.95 that are unsafe are marked with a black line about their results.

### 5.2.1.2 Design rules

First the plastic design resistances according to the existing EC design rules for chord face failure of non-penetrated X- and T-joints are calculated for the parameter configurations. The design rules for X-joints and T-joints are given in Equation 5.24 and Equation 5.25, respectively:

$$N_{1,Rd,T} = \frac{k_p * f_{y0} * t_0^2}{\sin\theta_1} * \frac{5,2}{(1-0,81\beta)} / \gamma_{M5}, \quad (5.24)$$

$$N_{1,Rd,X} = \frac{\gamma^{0,2} * k_p * f_{y0} * t_0^2}{\sin\theta_1} * (2,8 + 14,2 * \beta^2) / \gamma_{M5}. \quad (5.25)$$

$$\text{For } n_p > 0 \text{ (compression): } k_p = 1 - 0,3 * n_p * (1 + n_p), \quad \text{but } k_p \leq 1,0$$

$$\text{For } n_p \leq 0 \text{ (tension): } k_p = 1,0$$

The reduction factor  $k_p$  takes into account the stress in the chord due to compression or bending moment in the chord member. In compression, the chord member is more sensitive to imperfections, reducing the critical load, which will be captured by the reduction factor. Imperfections are not included within the scope of this research, and therefore, the  $k_p$  factor is assumed as a factor of 1.0, which is equal to the  $k_p$  factor for a chord member subjected to tension. The results from these design rules can be found under the columns “Eurocode X-joint” and “Eurocode T-joint”, in which it can be seen that the EC design rule for X-joints has some conservative (grey marked) approximations of the plastic capacity of the joint configurations with  $\beta$  factors 0.6 and 0.8, which is also the case for the EC design rule for T-joints for a  $\beta$  factor 0.8. In addition, for this latter design rule, some unsafe design resistances are obtained for joint configurations with  $\beta$  factors 0.6 and 0.4. When evaluating the resistance ratios, it can be seen at the bottom of the table, that the EC design rule for X-joints results in an average RR of 1.46 and the EC design rule for T-joints in an average RR of 1.12. However, for the EC design rule for T-joints, the capacity of some models is overpredicted (and thus unsafe), which is undesirable.

Therefore, a proposal is made for an adaptation to both design rules, in order to improve the EC design rule for X-joints and adapt the EC design rule for T-joints in such a way that the lowest RR obtained equals approximately 0.95. The formula for the improved design rule, “X-joint – Improved”, is given in Equation 5.26. To arrive at this formula for the design rule, the influences of the parameters are reviewed, from which it was concluded that only the  $\beta$  and the  $2\gamma$  parameters have a significant influence on the plastic capacity. Therefore, based on the influences of the parameters and by curve fitting to the FEA results, some factors are adapted in the formula to better describe the influence of the  $\beta$  parameter, and a factor 1.15 is added to fit the plastic design resistance obtained with the design rule to the plastic capacity of the FEA. The final adaptations to the design rule are shown in bold in Equation 5.26. The improved design rule for T-joints is shown in Equation 5.27. The design rule is adjusted in such a way that the overpredicted capacity deviate by a maximum of 5% from the (true) plastic capacity obtained by FEA, thus having a minimal RR of 0.95. These results are obtained by changing some factors in the design rule, which are shown in bold in Equation 5.27.

X-joint improved for non-penetrated joints

$$N_{1,Rd} = \mathbf{1.15} * \frac{k_p * f_{y0} * t_0^2}{\sin\theta_1} * \frac{\mathbf{4.4}}{(1-\beta)} / \gamma_{M5}, \quad (5.26)$$

T-joint improved for non-penetrated joints

$$N_{1,Rd} = \frac{\gamma^{0,2} * k_p * f_{y0} * t_0^2}{\sin\theta_1} * (\mathbf{2.1} + \mathbf{15.5} * \beta^2) / \gamma_{M5}. \quad (5.27)$$



In the results in Table 24, it can be seen that for the “X-joint improved” only one calculated capacity is conservative, and that the average, lowest and highest RR are 1.12, 0.97, and 1.32, respectively. Figure 41 shows a box plot of the obtained RR’s of the different design rules, where for every design rule the highest and lowest RR are shown by the horizontal top and bottom line, the middle 50% of the results fall within the drawn box, the median value is the horizontal line in between, and the average value of the design rule is marked with a cross. The boxplot for the EC X-joint, is shown in blue, and for the EC T-joint is shown in grey. The results for the RR by the design rule “X-joint improved” are shown in orange, from which it can be seen that the approximation of the FEA plastic capacity by the design rule is significantly improved, as the middle 50% of the results lays between a RR of 1 till 1.2 and the range of RR’s is reduced. The results for the “T-joint improved” are provided in yellow, in which multiple slightly conservative results may be identified, but the overprediction of the plastic capacity by the design rule is reduced significantly. For the improved T-joint design rule the average, lowest and highest RR are 1.19, 0.94, and 1.55, respectively.

Based on the boxplots, the proposed design rule “X-joint improved” given in Equation 5.26, which results in an average deviation from the FEA of 12.3%, a minimum RR of 0.97 (unsafe side) and a maximum RR of 1.32 (conservative), is found to be the most suitable formula to predict the plastic design resistance of non-penetrated geometries subjected to single-sided tension.

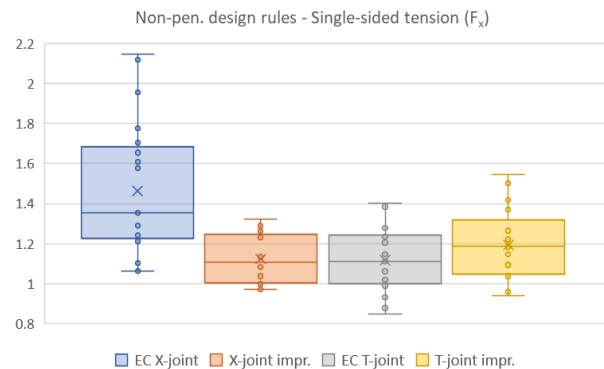


Figure 41: RR of the design rules for non-penetrated joints – Single-sided tension ( $F_x$ )

Table 24: Results design rules for non-penetrated joints – Single-sided tension ( $F_x$ )

Model			FEA results				EC X-joint		X-joint – impr.		EC T-joint		T-joint – impr.	
$\beta$	$2\gamma$	$2\delta$	$N_{1,FEA}$	Infl $\beta$	Infl $2\gamma$	Infl $2\delta$	$N_{1,Rd}$	RR	$N_{1,Rd}$	RR	$N_{1,Rd}$	RR	$N_{1,Rd}$	RR
0.8	30	10	5774.8	1.818	2.421	0.961	3383	1.707	5795	0.997	4680	1.234	4732	1.220
0.8	30	30	6010.4	1.917	2.298	1.066	3383	1.776	5795	1.037	4680	1.284	4732	1.270
0.8	30	50	5638.8	1.945	2.183		3383	1.667	5795	0.973	4680	1.205	4732	1.192
0.8	50	10	2385.1	1.811		0.912	1218	1.958	2086	1.143	1866	1.278	1887	1.264
0.8	50	30	2615	1.894		1.013	1218	2.147	2086	1.254	1866	1.401	1887	1.386
0.8	50	50	2582.6	1.922			1218	2.120	2086	1.238	1866	1.384	1887	1.369
0.6	30	10	3176.6	1.432	2.412	1.013	2317	1.371	2897	1.096	3115	1.020	3023	1.051
0.6	30	30	3134.9	1.468	2.271	1.081	2317	1.353	2897	1.082	3115	1.007	3023	1.037
0.6	30	50	2899.3	1.547	2.158		2317	1.251	2897	1.001	3115	0.931	3023	0.959
0.6	50	10	1317.2	1.673		0.954	834	1.579	1043	1.263	1242	1.061	1205	1.093
0.6	50	30	1380.6	1.976		1.027	834	1.655	1043	1.324	1242	1.112	1205	1.145
0.6	50	50	1343.7	1.994			834	1.611	1043	1.288	1242	1.082	1205	1.115
0.4	30	10	2218.2	1.460	2.817	1.038	1762	1.259	1932	1.148	1997	1.111	1803	1.230
0.4	30	30	2136.2		3.057	1.140	1762	1.213	1932	1.106	1997	1.070	1803	1.185
0.4	30	50	1874.2		2.781		1762	1.064	1932	0.970	1997	0.939	1803	1.040
0.4	50	10	787.4	1.193		1.127	634	1.241	695	1.132	796	0.989	719	1.095
0.4	50	30	698.7	1.089		1.037	634	1.102	695	1.005	796	0.878	719	0.972
0.4	50	50	674				634	1.063	695	0.969	796	0.847	719	0.938
0.2	30	10	1519.4		2.301		1421	1.069	1449	1.049	1326	1.146	1071	1.419
0.2	50	10	660.2			1.029	512	1.290	522	1.266	529	1.249	427	1.546
0.2	50	30	641.8				512	1.254	522	1.231	529	1.214	427	1.503
							<b>Mean</b>	<b>1.464</b>	<b>Mean</b>	<b>1.123</b>	<b>Mean</b>	<b>1.116</b>	<b>Mean</b>	<b>1.192</b>
							Lowest	1.063	Lowest	0.969	Lowest	0.847	Lowest	0.938
							Highest	2.147	Highest	1.324	Highest	1.401	Highest	1.546

### 5.2.1.3 Verification of the governing failure mechanisms

For each parameter configuration, the plastic design resistances according to all relevant design rule for non-penetrated joints are calculated. The minimum of these resistances then indicates which failure mechanism is governing according to the used set of design rules. This governing failure mechanism is compared to the actual governing failure mechanism that is observed in the FEA. This is done for the set of design rules containing existing EC design rules, as well as for the set of design rules in which the, in this research created design rules, are included. In this way the influence of the proposed new design rules on the prediction of the governing failure mechanism can be evaluated while verifying it with the results from the FEA as well. A summary of this procedure, containing merely the governing plastic design resistance and failure mechanisms according to FEA and design rules, is presented in the tables shown in each subparagraph on the verification of the governing failure mechanism for the several load cases. But as an example, in Table 25, the design resistances of all relevant failure mechanisms and the selection of the governing failure mechanism is shown for non-penetrated geometries with  $\beta$  factor 0.2. The relevant failure mechanisms are in this case from failure group 1, EC basic cross-section failures, Brace cross-section failure (1 B cs), and Chord bending moment (1 C bm), and from failure group 2, EC joint failures, chord face failure (2 C ff) and chord punching shear failure (2 C ps). For chord face failure, the plastic design resistance according to the design rules for both X- and for T-joints are given, since the joint configurations considered in this research could in case of single-sided loading be interpret as either an X-joint loaded on only one side of the brace or a T-joint. Under “comparison EC-FEA”, the by the set of design rules governing plastic design resistance and failure mechanism are given and next to it, the plastic capacity and corresponding failure mechanism observed in the FEA are shown. This part of Table 25 is also visible in the last block of summarized representations of this procedure in Table 26 and Table 27. The extensive versions (of which an example is given in Table 25) of the summarized representations presented in all upcoming subparagraphs, can be found in Appendix F.

In Table 26 and Table 27 the results for the parameter configurations for non-penetrated geometries subjected to single-sided tension are shown, where in Table 26, the comparison between FEA and the existing set of design rules is given, and Table 27 provides the comparison between FEA and the set of adjusted design rules, as proposed in this research. It can be seen that for these geometrical parameter configurations, the design rules from the EC (Table 26) predict the correct failure mechanism, and that the plastic design resistance for brace cross-section failure corresponds to the plastic capacity obtained in the FEA. However, for geometries failing in chord face failure, differences are observed between the FEA plastic capacity and the EC plastic design resistance. For the adjusted set of design rules for non-penetrated CHS X-joints subjected to single-sided loading, for which the comparison of the failure modes is given in Table 27, the basic cross-section design are retained, but for the joint failures, the proposed “X-joint improved” design rule is applied. It can be seen that again the correct failure mechanisms are predicted by the set of design rules, but for chord face failure, the plastic design resistances calculated with the adjusted set of design rules, approximates the FEA plastic capacity better.

### 5.2.1.4 Conclusion design rule non-penetrated geometries

For the non-penetrated CHS X-joints subjected to single-sided tension ( $F_x$ ) can be concluded that the EC design rule for chord face failure of X-joints, with an average RR of 1.46, slightly underpredicts the plastic capacity and is therefore conservative. In addition, it can be concluded that the design rule for T-joints better fits the FEA results, with an average RR of 1.12, but there are some overpredicted yield loads, which is unsafe and undesirable. Therefore, this design rule in such a way, that in unsafe cases, the RR deviates from 1 by a maximum of about 5%, resulting in the design rule “T-joint adjusted” with an average RR of 1.19. The final design rule, which best fits the FEA plastic capacity, is the “X-joint improved” design rule, which is given in Equation 5.26. This design rule has an average RR of 1.12 and a lowest and highest RR of 0.97 and 1.32, respectively.

The improved design rule is based on the EC design rules for joints subjected to single-sided tension ( $F_x$ ), for which the current design rules well predicted the failure mechanisms, but for chord face failure the approximated design resistances are conservative. With the new improved design rules, less conservative plastic resistances are predicted, while still the correct failure mechanism is predicted.

The design rules for the load-case single-sided tension, are also applicable for the load-case single-sided compression.

Table 25: Example EC design rules failure mechanism calculation

Model			Failure mechanisms					Comparison EC - FEA			
$\beta$	$2\gamma$	$2\delta$	1 B cs	1 C bm	2 C ff (X- and T-joint)		2 C ps	Governing Eurocode		FEA	
(-)	(-)	(-)	$N_{1,Rd}^*$ (kN)	$N_{1,Rd}^*$ (kN)	$N_{X,1,Rd}^*$ (kN)	$N_{T,1,Rd}^*$ (kN)	$N_{1,Rd}^*$ (kN)	$N_{1,Rd}$ (kN)	Failure mode	$N_{1,FEA}$ (kN)	Failure mode
0.2	10	10	<b>2331</b>	21632	12791	9579	7478	<b>2331.3</b>	1 B cs	<b>2339.1</b>	1 B cs
0.2	10	30	<b>835</b>	21632	12791	9579	7478	<b>834.6</b>	1 B cs	<b>837.6</b>	1 B cs
0.2	10	50	<b>508</b>	21632	12791	9579	7478	<b>507.7</b>	1 B cs	<b>512.4</b>	1 B cs
0.2	30	10	2331	8288	1421	<b>1326</b>	2493	<b>1325.8</b>	2 C ff	<b>1519.4</b>	2 C ff
0.2	30	30	<b>835</b>	8288	1421	1326	2493	<b>834.6</b>	1 B cs	<b>846.2</b>	1 B cs
0.2	30	50	<b>508</b>	8288	1421	1326	2493	<b>507.7</b>	1 B cs	<b>512.6</b>	1 B cs
0.2	50	10	2331	5110	<b>512</b>	529	1496	<b>511.6</b>	2 C ff	<b>660.2</b>	2 C ff
0.2	50	30	835	5110	<b>512</b>	529	1496	<b>511.6</b>	2 C ff	<b>641.8</b>	2 C ff
0.2	50	50	<b>508</b>	5110	512	529	1496	<b>507.7</b>	1 B cs	<b>510.8</b>	1 B cs

Table 26: Failure mechanism calculation results for existing EC design rules for non-penetrated joints

Model		$\beta$ 0.8				$\beta$ 0.6				$\beta$ 0.4				$\beta$ 0.2			
$2\gamma$	$2\delta$	EC		FEA		EC		FEA		EC		FEA		EC		FEA	
(-)	(-)	$N_{1,Rd}$ (kN)	Failure mode	$N_{1,FEA}$ (kN)	Failure mode	$N_{1,Rd}$ (kN)	Failure mode	$N_{1,FEA}$ (kN)	Failure mode	$N_{1,Rd}$ (kN)	Failure mode	$N_{1,FEA}$ (kN)	Failure mode	$N_{1,Rd}$ (kN)	Failure mode	$N_{1,FEA}$ (kN)	Failure mode
10	10	19724	1 C bm	23943	1 C bm	20321	1 C bm	21054	1 C bm	9325	1 B cs	9353	1 B cs	2331	1 B cs	2339	1 B cs
10	30	13354	1 B cs	13379	1 B cs	7512	1 B cs	7533	1 B cs	3339	1 B cs	3347	1 B cs	835	1 B cs	838	1 B cs
10	50	8123	1 B cs	8153	1 B cs	4569	1 B cs	4587	1 B cs	2031	1 B cs	2038	1 B cs	508	1 B cs	512	1 B cs
30	10	3383	2 C ff	5775	3 C ff	2317	2 C ff	3177	3 C ff	1762	2 C ff	2218	3 C ff	1326	2 C ff	1519	3 C ff
30	30	3383	2 C ff	6010	3 C ff	2317	2 C ff	3135	3 C ff	1762	2 C ff	2136	3 C ff	835	1 B cs	846	1 B cs
30	50	3383	2 C ff	5639	3 C ff	2317	2 C ff	2899	3 C ff	1762	2 C ff	1874	3 C ff	508	1 B cs	513	1 B cs
50	10	1218	2 C ff	2385	3 C ff	834	2 C ff	1317	3 C ff	634	2 C ff	787	3 C ff	512	2 C ff	660	3 C ff
50	30	1218	2 C ff	2615	3 C ff	834	2 C ff	1381	3 C ff	634	2 C ff	699	3 C ff	512	2 C ff	642	3 C ff
50	50	1218	2 C ff	2583	3 C ff	834	2 C ff	1344	3 C ff	634	2 C ff	674	3 C ff	508	1 B cs	511	1 B cs

Table 27: Failure mechanism calculation results for the improved design rules for non-penetrated joints

Model		$\beta$ 0.8				$\beta$ 0.6				$\beta$ 0.4				$\beta$ 0.2			
$2\gamma$	$2\delta$	EC / Pen		FEA		EC / Pen		FEA		EC / Pen		FEA		EC / Pen		FEA	
(-)	(-)	$N_{1,Rd}$ (kN)	Failure mode	$N_{1,FEA}$ (kN)	Failure mode	$N_{1,Rd}$ (kN)	Failure mode	$N_{1,FEA}$ (kN)	Failure mode	$N_{1,Rd}$ (kN)	Failure mode	$N_{1,FEA}$ (kN)	Failure mode	$N_{1,Rd}$ (kN)	Failure mode	$N_{1,FEA}$ (kN)	Failure mode
10	10	19724	1 C bm	23943	1 C bm	20321	1 C bm	21054	1 C bm	9325	1 B cs	9353	1 B cs	2331	1 B cs	2339	1 B cs
10	30	13354	1 B cs	13379	1 B cs	7512	1 B cs	7533	1 B cs	3339	1 B cs	3347	1 B cs	835	1 B cs	838	1 B cs
10	50	8123	1 B cs	8153	1 B cs	4569	1 B cs	4587	1 B cs	2031	1 B cs	2038	1 B cs	508	1 B cs	512	1 B cs
30	10	5795	3 C ff	5775	3 C ff	2897	3 C ff	3177	3 C ff	1932	3 C ff	2218	3 C ff	1449	3 C ff	1519	3 C ff
30	30	5795	3 C ff	6010	3 C ff	2897	3 C ff	3135	3 C ff	1932	3 C ff	2136	3 C ff	835	1 B cs	846	1 B cs
30	50	5795	3 C ff	5639	3 C ff	2897	3 C ff	2899	3 C ff	1932	3 C ff	1874	3 C ff	508	1 B cs	513	1 B cs
50	10	2086	3 C ff	2385	3 C ff	1043	3 C ff	1317	3 C ff	695	3 C ff	787	3 C ff	522	3 C ff	660	3 C ff
50	30	2086	3 C ff	2615	3 C ff	1043	3 C ff	1381	3 C ff	695	3 C ff	699	3 C ff	522	3 C ff	642	3 C ff
50	50	2086	3 C ff	2583	3 C ff	1043	3 C ff	1344	3 C ff	695	3 C ff	674	3 C ff	508	1 B cs	511	1 B cs

## 5.2.2 Penetrated CHS X-joints

With the knowledge gained from comparing the non-penetrated results, the existing EC design rules and the improved design rules, the penetrated joints are examined. In this paragraph, the results from the parameter study are provided and compared, various design rules and steps taken in order to arrive at these design rules are given, and the governing failure mechanism obtained with the improved set of design rules is verified.

### 5.2.2.1 Design rules

In Table 28, the plastic capacity according to FEA and the influences of the geometrical parameters on these results are given for penetrated joint configurations subjected to single-sided tension. Next to that, the plastic design resistances as calculated with five different design rules are shown. The first two design rules are the existing EC design rules for non-penetrated joints and the other three design rules are adjustments on the existing design rules proposed in this graduation research. The formulas for the first design rule “Eurocode X-joint” and the second design rule “Eurocode T-joint”, are provided in Equation 5.24 and Equation 5.25, respectively. In the associated columns in Table 28, it can be seen that for both design rules, a significantly lower plastic design resistance is calculated than the plastic capacity that is observed in FEA. With an average RR for the EC X-joint and

EC T-joint, of 3.32 and 2.45, respectively, the design rules are considered to be very conservative, which can also be seen in the boxplot of the RR's in Figure 42. Using these two design rules and a similar procedure as used to create the improved and adjusted design rules for non-penetrated joints, as provided in Equation 5.26 and 5.27, the design rules "X-joint improved", presented in Equation 5.28, and "T-joint improved", presented in Equation 5.29, are created.

X-joint improved for penetrated joints

$$N_{1,Rd} = 1.1 * \frac{k_p * f_{y0} * f_{\delta} * t_0^2}{\sin \theta_1} * \frac{9.0}{(1 - 0.81 * f_{\beta} * \beta)} / \gamma_{M5}, \quad (5.28)$$

$$\text{where } f_{\delta} = 1 + (50 - 2\delta)/200,$$

$$\text{where } f_{\beta} = 1.8 * \beta + 2.3.$$

T-joint improved for penetrated joints

$$N_{1,Rd} = \frac{\gamma^{0.2} * k_p * f_{y0} * t_0^2}{\sin \theta_1} * (6.8 + 14.2 * f_{\beta} * \beta^2) / \gamma_{M5} \quad (5.29)$$

In the improved design rule for penetrated CHS X-joints, a factor  $f_{\delta}$  is applied to describe the influence of  $\delta$  on the plastic capacity of the joints. This factor is created in such a way, that it fits the influences of  $2\delta$  as given in the associated column of Table 28, i.e. it approximates the values 1.2, 1.1 and 1.0 for  $2\delta$  factors of 10, 30 and 50, respectively. The same is done for  $f_{\beta}$ , with which the influence of  $\beta$  is described in the design rule. The factors 1.1 and 9.0 in the formula, are adjusted to improve the fit of the plastic design resistances of the design rule to the observed plastic capacity in the FEA.

In the improved design rule for penetrated CHS T-joints, merely the factor  $f_{\beta}$  is included and by changing the factor 2.8 (as found in the original EC design rule) to 6.8, the plastic design resistance is fitted to the plastic capacity. Table 28 and the left graph in Figure 42, show the design resistances and associated resistance ratios of these five design rules. It can be seen that the design rule "X-joint improved" has some conservative results, which are indicated by a grey square about the result, and one overpredicted design resistance, which is indicated by a black square. The design rule has an average RR of 1.39, for which the lowest and highest RR are 0.83 and 2.15, respectively. For the improved design rule for T-joints there are no overpredicted results. However, more results are considered to be conservative. For the design rule an average, lowest and highest RR is found of 1.47, 0.95 and 2.03, respectively.

The fifth design rule "Stress pattern", is not based on the existing EC design rules for non-penetrated X- or T-joints, but is created by examination of the, in FEA observed, stress pattern in the chord member. The geometrical parameters that partially describe the stress pattern observed, have an influence on the height of the stresses in the joints and therefore on the final plastic capacity. The chord diameter ( $d_0$ ), chord wall thickness ( $t_0$ ),  $\beta$  factor and  $\pi$  are used to describe the stress pattern for chord face failure on the chord wall, finally resulting in a new design formula that is presented in Equation 5.30. To improve the fit of the design rule results to the plastic capacity found in FEA, a factor of 0.35 is included. With this formula, an average, lowest and highest RR for the investigated parametrical geometries is achieved of 1.19, 0.95, and 1.52, respectively. It is observed that, in particular for models with a  $\beta$  factor of 0.4 and 0.6, some plastic design resistances may be considered as conservative, with a RR between 1.3 and 1.5.

Stress pattern

$$N_{1,Rd} = 0.35 * \frac{k_p * f_{y0} * t_0 * \beta * d_0 * \pi * f_{\delta}}{\sin \theta_1} / \gamma_{M5} \quad (5.30)$$

The design rule represented in Equation 5.30 is simplified by replacing  $\beta \cdot d_0$  by the brace diameter ( $d_1$ ) and combining the factor 0.35 with  $\pi$  into a factor of 1.1, which resulted in the sixth design rule "Stress pattern 1", shown in Equation 5.31. The plastic design resistances obtained with this design rule are nearly the same as obtained with the original formula, and are presented in Table 29 and the right graph in Figure 42.

Stress pattern 1

$$N_{1,Rd} = 1.1 * \frac{k_p * f_{y0} * t_0 * d_1 * f_{\delta}}{\sin \theta_1} / \gamma_{M5} \quad (5.31)$$

The simplified formula is used as a starting point for further improvements of the conservative approximations of the plastic capacity for joint configurations with a  $\beta$  factor of 0.4 and 0.6. Since for geometries with  $\beta$  factor 0.8 and 0.2, the RR's do approach 1, the way the influence of the  $\beta$  factor is processed in the design formula is reviewed again.

Two additional design rules are created, that describe the influence that  $\beta$  has on the plastic resistance more accurate. In Equation 5.32 and 5.33, the adjusted design rules “Stress pattern 2a” and “Stress pattern 2b” are presented, for which the adjustments with respect to Equation 5.31 are shown in bold. With these improved design rules, the average RR is decreased from 1.19 to 1.11 for design rule 2a and to 1.09 for design rule 2b, as can be seen in the third and fourth column of Table 29 and the right graph in Figure 42. Next to that, the highest RR for stress pattern 2a is decreased from 1.52 to 1.35, and for design rule 2b from 1.52 to 1.34.

Stress pattern 2a

$$N_{1,Rd} = \mathbf{1.05} * \frac{k_p * f_{y0} * t_0 * d_1 * f_{\delta}}{\sin \theta_1} * (-2 * (\beta - 0.5)^2 + 1.2) / \gamma_{M5} \quad (5.32)$$

Stress pattern 2b

$$N_{1,Rd} = 1.1 * \frac{k_p * f_{y0} * t_0 * d_1 * f_{\delta}}{\sin \theta_1} * (\sin(\mathbf{0.65} * \beta * \pi) - \beta + \mathbf{0.8}) / \gamma_{M5} \quad (5.33)$$

Lastly, a design rule is considered that is completely constructed using the influences of the geometrical parameters as given in the table next to the plastic capacity from FEA. For this design rule, a basic value for the plastic resistance is back-calculated by dividing the plastic capacity through the corresponding influences of  $\beta$ ,  $2\gamma$ ,  $2\delta$ . This resulted in an almost stable value for all considered geometrical parameter configurations, which has to be described by the parameters that are fixed in this study, like the yield strength ( $f_{y0}$ ) and chord diameter ( $d_0$ ) (as only the brace diameter is valued using the  $\beta$  factor). Once this stable part has been formulated, the influences of the geometrical parameters are formulated in three independent formula parts, by fitting these parts on the influence factors shown in the table. The independent parts are then combined in a single design rule that is shown in Equation 5.34.

Result factors

$$N_{1,Rd} = \frac{100}{2\delta + 75} * \frac{k_p * f_{y0} * d_1 * \gamma^{0.1} * t_0}{\sin \theta_1} / \gamma_{M5} \quad (5.34)$$

This design rule approximates the plastic capacity (according to FEA) with an average, lowest and highest RR of 1.09, 0.88, and 1.30, respectively. However, two of the geometrical parameter configurations resulted in a plastic design resistance that overpredicts the plastic capacity and are therefore unsafe. Adjusting the formula in such a way that the lowest RR was 0.95, resulted in the highest RR to be larger than 1.3, causing this design rule to become less interesting than the design rules Stress pattern 2a and 2b.

Table 29 and Figure 42 (right graph), shows the results of the extra four design rules that were just elaborated. It can be seen that design rules stress pattern 2a and stress pattern 2b best approximates the plastic capacity.

Table 28: Results design rules for penetrated joints - Single-sided tension ( $F_x$ ) – part 1

Model			FEA results			EC X-joint		EC T-joint		X-joint impr.		T-joint impr.		Stress pattern		
$\beta$	$2\gamma$	$2\delta$	$N_{1,FEA}$	Infl $\beta$	Infl $2\gamma$	Infl $2\delta$	$N_{1,Rd}$	RR	$N_{1,Rd}$	RR	$N_{1,Rd}$	RR	$N_{1,Rd}$	RR	$N_{1,Rd}$	RR
0.8	30	30	6575.6	1.005	1.508	1.143	3383	1.943	4680	1.405	5634	1.167	5754	1.143	6648	0.989
0.8	30	50	5752.6		1.518		3383	1.700	4680	1.229	5122	1.123	5754	1.000	6044	0.952
0.8	50	30	4361.5	1.083		1.151	1218	3.581	1866	2.337	2028	2.150	2294	1.901	3989	1.093
0.8	50	50	3789.7	1.065			1218	3.111	1866	2.031	1844	2.055	2294	1.652	3626	1.045
0.6	30	10	8019.2	1.458	1.934	1.226	2317	3.461	3115	2.575	6684	1.200	5132	1.563	5440	1.474
0.6	30	30	6540.1		1.623		2317	2.823	3115	2.100	6127	1.067	5132	1.274	4986	1.312
0.6	50	10	4147.2	1.737		1.029	834	4.972	1242	3.340	2406	1.724	2046	2.027	3264	1.271
0.6	50	30	4028.7	1.896		1.132	834	4.830	1242	3.244	2206	1.826	2046	1.969	2992	1.347
0.6	50	50	3557.8	1.751			834	4.265	1242	2.865	2005	1.774	2046	1.739	2720	1.308
0.4	30	10	5500.2		2.303		1762	3.122	1997	2.755	5575	0.987	4090	1.345	3626	1.517
0.4	50	10	2388.2	2.027		1.124	634	3.765	796	3.000	2007	1.190	1631	1.464	2176	1.098
0.4	50	30	2124.8			1.046	634	3.350	796	2.669	1840	1.155	1631	1.303	1995	1.065
0.4	50	50	2032.1				634	3.204	796	2.553	1672	1.215	1631	1.246	1813	1.121
0.2	50	10	1178.1				512	2.303	529	2.229	1428	0.825	1240	0.950	1088	1.083
							<b>Mean</b>	<b>3.316</b>	<b>Mean</b>	<b>2.452</b>	<b>Mean</b>	<b>1.390</b>	<b>Mean</b>	<b>1.470</b>	<b>Mean</b>	<b>1.191</b>
							Lowest	1.700	Lowest	1.229	Lowest	0.825	Lowest	0.950	Lowest	0.952
							Highest	4.972	Highest	3.340	Highest	2.150	Highest	2.027	Highest	1.517

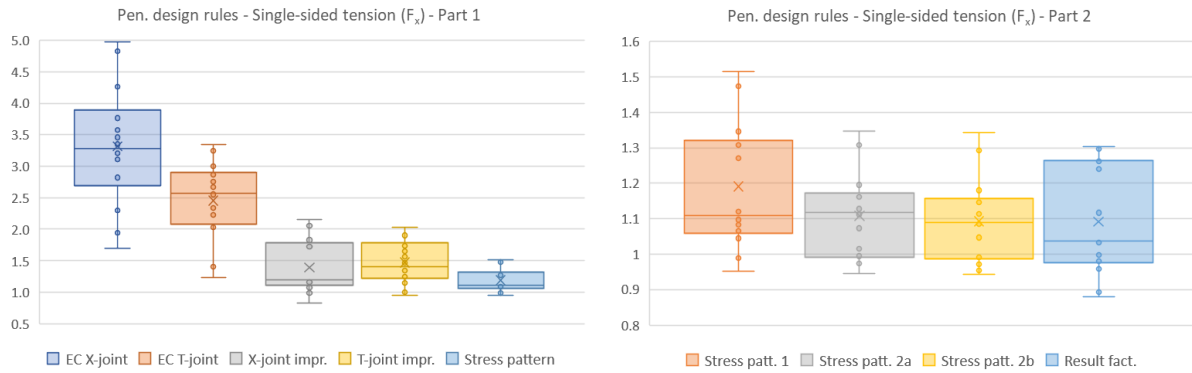


Figure 42: RR design rules for penetrated joints – Single-sided tension ( $F_x$ ) – Part 1 (left) & 2 (right)

Table 29: Results design rules for penetrated joints - Single-sided tension ( $F_x$ ) – part 1

Model			FEA results				Stress patt. 1		Stress patt. 2a		Stress patt. 2b		Result factors	
$\beta$	$2\gamma$	$2\delta$	$N_{1,FEA}$	Infl $\beta$	Infl $2\gamma$	Infl $2\delta$	$N_{1,Rd}$	RR	$N_{1,Rd}$	RR	$N_{1,Rd}$	RR	$N_{1,Rd}$	RR
0.8	30	30	6575.6	1.005	1.508	1.143	6651	0.989	6476	1.015	6638	0.991	6863	0.958
0.8	30	50	5752.6		1.518		6046	0.951	5887	0.977	6035	0.953	5765	0.998
0.8	50	30	4361.5	1.083		1.151	3991	1.093	3885	1.123	3983	1.095	4334	1.006
0.8	50	50	3789.7	1.065			3628	1.045	3532	1.073	3621	1.047	3640	1.041
0.6	30	10	8019.2	1.458	1.934	1.226	5442	1.474	6129	1.308	6208	1.292	6359	1.261
0.6	30	30	6540.1		1.623		4988	1.311	5619	1.164	5691	1.149	5147	1.271
0.6	50	10	4147.2	1.737		1.029	3265	1.270	3678	1.128	3725	1.113	4015	1.033
0.6	50	30	4028.7	1.896		1.132	2993	1.346	3371	1.195	3415	1.180	3250	1.239
0.6	50	50	3557.8	1.751			2721	1.308	3065	1.161	3104	1.146	2730	1.303
0.4	30	10	5500.2		2.303		3628	1.516	4086	1.346	4096	1.343	4239	1.298
0.4	50	10	2388.2	2.027		1.124	2177	1.097	2452	0.974	2457	0.972	2677	0.892
0.4	50	30	2124.8			1.046	1995	1.065	2247	0.945	2253	0.943	2167	0.981
0.4	50	50	2032.1				1814	1.120	2043	0.995	2048	0.992	1820	1.116
0.2	50	10	1178.1				1088	1.082	1060	1.112	1085	1.086	1338	0.880
							<b>Mean</b>	<b>1.190</b>	<b>Mean</b>	<b>1.108</b>	<b>Mean</b>	<b>1.093</b>	<b>Mean</b>	<b>1.091</b>
							Lowest	0.951	Lowest	0.945	Lowest	0.943	Lowest	0.880
							Highest	1.516	Highest	1.346	Highest	1.343	Highest	1.303

### 5.2.2.2 Verification of the governing failure mechanism

In Paragraph 5.2.1.3 the principles are explained for the verification of the governing failure mechanism. In this paragraph the same principles are applied to verify the governing failure mechanism for penetrated CHS X-joints subjected to single-sided tension. In Table 30 the results for the existing set of EC design rules (intended for non-penetrated CHS joints) are given. The basic cross-section design rules and the existing EC design rules for non-penetrated joints are applied to approximate the plastic design resistance and governing failure mechanism. In Table 31 the results for the improved penetrated set of design rules are given. The existing basic cross-section design rules and the joint failure design rule Stress pattern 2b, as provided in Equation 5.33, are used. In the tables the results of the joint configurations for which the governing failure mechanisms as calculated with the set of design rules deviates from the governing mechanism observed in FEA, are marked. It can be seen that the improved penetrated set of design rules, predict the correct failure mechanism more often than the existing set of EC design rules. Moreover, it can be seen that for the penetrated set of design rules, the plastic design resistances for chord face failure deviate significantly less from the plastic capacity, compared to the resistances calculated with the set of EC design rules for non-penetrated joints. The calculations with the design set containing the new design rules for penetrated joints, still deviates from the results observed in FEA for some parameter configurations. This can however be explained by the slight conservatism of the new chord face failure rule and the fact that for these particular configurations, the differences in plastic design resistance to the different failure mechanisms are minimal.

Table 30: Failure mechanism calculation results for existing EC design rules for non-penetrated joints

Model		$\beta$ 0.8				$\beta$ 0.6				$\beta$ 0.4				$\beta$ 0.2			
2 $\gamma$ (-)	2 $\delta$ (-)	EC		FEA		EC		FEA		EC		FEA		EC		FEA	
		N <sub>1,Rd</sub> (kN)	Failure mode	N <sub>1,FEA</sub> (kN)	Failure mode	N <sub>1,Rd</sub> (kN)	Failure mode	N <sub>1,FEA</sub> (kN)	Failure mode	N <sub>1,Rd</sub> (kN)	Failure mode	N <sub>1,FEA</sub> (kN)	Failure mode	N <sub>1,Rd</sub> (kN)	Failure mode	N <sub>1,FEA</sub> (kN)	Failure mode
10	10	19724	1 C bm	20221	1 C bm	20321	1 C bm	20373	1 C bm	9325	1 B cs	9334	1 B cs	2331	1 B cs	2331	1 B cs
10	30	13354	1 B cs	13369	1 B cs	7512	1 B cs	7515	1 B cs	3339	1 B cs	3342	1 B cs	835	1 B cs	834	1 B cs
10	50	8123	1 B cs	8126	1 B cs	4569	1 B cs	4574	1 B cs	2031	1 B cs	2032	1 B cs	508	1 B cs	508	1 B cs
30	10	3383	2 C ff	8742	1 C bm	2317	2 C ff	8019	3 C ff	1762	2 C ff	5500	3 C ff	1326	2 C ff	2345	1 B cs
30	30	3383	2 C ff	6576	3 C ff	2317	2 C ff	6540	3 C ff	1762	2 C ff	3348	1 B cs	835	1 B cs	843	1 B cs
30	50	3383	2 C ff	5753	3 C ff	2317	2 C ff	4555	1 B cs	1762	2 C ff	2029	1 B cs	508	1 B cs	509	1 B cs
50	10	1218	2 C ff	5040	1 C bm	834	2 C ff	4147	3 C ff	634	2 C ff	2388	3 C ff	512	2 C ff	1178	3 C ff
50	30	1218	2 C ff	4362	3 C ff	834	2 C ff	4029	3 C ff	634	2 C ff	2125	3 C ff	512	2 C ff	838	1 B cs
50	50	1218	2 C ff	3790	3 C ff	834	2 C ff	3558	3 C ff	634	2 C ff	2032	3 C ff	508	1 B cs	513	1 B cs

Table 31: Failure mechanism calculation results for new design rules for penetrated joints

Model		$\beta$ 0.8				$\beta$ 0.6				$\beta$ 0.4				$\beta$ 0.2			
2 $\gamma$ (-)	2 $\delta$ (-)	EC / Pen		FEA		EC / Pen		FEA		EC / Pen		FEA		EC / Pen		FEA	
		N <sub>1,Rd</sub> (kN)	Failure mode	N <sub>1,FEA</sub> (kN)	Failure mode	N <sub>1,Rd</sub> (kN)	Failure mode	N <sub>1,FEA</sub> (kN)	Failure mode	N <sub>1,Rd</sub> (kN)	Failure mode	N <sub>1,FEA</sub> (kN)	Failure mode	N <sub>1,Rd</sub> (kN)	Failure mode	N <sub>1,FEA</sub> (kN)	Failure mode
10	10	19724	1 C bm	20221	1 C bm	18625	3 C ff	20373	1 C bm	9325	1 B cs	9334	1 B cs	2331	1 B cs	2331	1 B cs
10	30	13354	1 B cs	13369	1 B cs	7512	1 B cs	7515	1 B cs	3339	1 B cs	3342	1 B cs	835	1 B cs	834	1 B cs
10	50	8123	1 B cs	8126	1 B cs	4569	1 B cs	4574	1 B cs	2031	1 B cs	2032	1 B cs	508	1 B cs	508	1 B cs
30	10	7241	3 C ff	8742	1 C bm	6208	3 C ff	8019	3 C ff	4096	3 C ff	5500	3 C ff	1809	3 C ff	2345	1 B cs
30	30	6638	3 C ff	6576	3 C ff	5691	3 C ff	6540	3 C ff	3339	1 B cs	3348	1 B cs	835	1 B cs	843	1 B cs
30	50	6035	3 C ff	5753	3 C ff	4569	1 B cs	4555	1 B cs	2031	1 B cs	2029	1 B cs	508	1 B cs	509	1 B cs
50	10	4345	3 C ff	5040	1 C bm	3725	3 C ff	4147	3 C ff	2457	3 C ff	2388	3 C ff	1085	3 C ff	1178	3 C ff
50	30	3983	3 C ff	4362	3 C ff	3415	3 C ff	4029	3 C ff	2253	3 C ff	2125	3 C ff	835	1 B cs	838	1 B cs
50	50	3621	3 C ff	3790	3 C ff	3104	3 C ff	3558	3 C ff	2031	1 B cs	2032	3 C ff	508	1 B cs	513	1 B cs

### 5.2.2.3 Conclusion design rule for penetrated CHS X-joints subjected to single-sided tension (F<sub>x</sub>)

For penetrated CHS X-joints subjected to single-sided tension (F<sub>x</sub>) can be concluded that the existing EC design rules for non-penetrated T- and X-joints, with an average RR of 3.32 and 2.45, underpredict the plastic capacity observed in FEA. The improved design rules “X-joint impr.” and “T-joint impr.”, which are based on the existing EC design rules for non-penetrated T- and X-joints, better approximate the plastic design capacity, however, with an average RR of 1.39 and 1.47, they are still considered to be too conservative and some results deviate too much. Therefore five alternative design rules are created of which four are based on the stress pattern observed in FEA and the other one is based on the influences of the parameter factors on the plastic capacity. Although this latter design rule “Result factors”, is easier to interpret and can be deduced more clearly from the applied geometrical parameters, this design rule predicts design resistances with larger deviations from the plastic capacity observed in FEA. Based on the RR’s, it is therefore proposed to use the design rule “Stress Pattern 2b”, which is provided in Equation 5.33, for calculating the plastic design resistance of penetrated CHS X-joints subjected to single-sided tension (F<sub>x</sub>). For this design rule an average, lowest and highest RR of 1.09, 0.94, and 1.34, respectively, are obtained.

From the verification of the governing failure mechanisms, for which the results are shown in Table 30 and Table 31, it can be concluded that for the set of improved design rules for penetrated joints, in which the design rule Stress pattern 2b is included, more often the correct failure mechanism is approximated compared to the set of existing EC design rules for non-penetrated joints. Next to that, can be concluded that for geometries failing in chord face failure, the plastic design resistance calculated by the improved design rules, deviates less from the plastic capacity obtained by FEA, as the plastic design resistance calculated with the existing EC design rules for non-penetrated joints did. However, also for the new set of design rules, some deviations in governing failure mechanism are observed in Table 31, but this can be explained by the slight conservatism of the new chord face failure rule and the fact that for the particular configurations for which the failure mechanism deviates from the one observed in FEA, the differences in plastic design resistance to the different possible failure mechanisms are minimal.

### 5.2.2.4 Compression

The parameter study for penetrated configurations subjected to single-sided compression is provided only for the geometries with a  $\beta$  factor of 0.2 and 0.8. From these parameter configurations it has been concluded that geometries subjected to single-sided compression have plastic capacity that are almost equal to the capacity of geometries subjected to single-sided tension. Therefore, no simulations have been performed for additional parameter configurations. To confirm the validity of the new proposed design rules for compression as well, the plastic capacity observed in FEA are compared with the new design rules for penetrated joints, as is also done in Table 29 for tension. The results of the comparisons are given in Table 32 and in the left graph of Figure 43. In the table, it can be seen that the new design rules for penetrated joints are also suitable for geometries subjected to single-sided compression, since an average, lowest and highest RR for stress pattern 2b of 1.03, 0.95, and 1.12, respectively, is found. The average and highest RR depicted in the table are slightly lower compared to those of the geometries subjected to single-sided tension. This can however, be explained by the fact that  $\beta$  0.4 and 0.6 are omitted for geometries subjected to single-sided compression, while they cause produce the highest RR's and an increase of the average RR for the geometries subjected to single-sided tension.

Table 32: Result design rules for penetrated joints – single-sided compression ( $F_x$ )

Model			FEA results			Stress patt. 1		Stress patt. 2a		Stress patt. 2b		Result factors		
$\beta$	$2\gamma$	$2\delta$	$N_{1,FEA}$	Infl $\beta$	Infl $2\gamma$	Infl $2\delta$	$N_{1,Rd}$	RR	$N_{1,Rd}$	RR	$N_{1,Rd}$	RR	$N_{1,Rd}$	RR
0.8	30	30	6312.1		1.418	1.107	6651	0.949	6476	0.975	6638	0.951	6863	0.920
0.8	30	50	5699.8		1.480		6046	0.943	5887	0.968	6035	0.945	5765	0.989
0.8	50	30	4449.6			1.155	3991	1.115	3885	1.145	3983	1.117	4334	1.027
0.8	50	50	3850.9				3628	1.061	3532	1.090	3621	1.064	3640	1.058
0.2	50	10	1165.5				1088	1.071	1060	1.100	1085	1.074	1338	0.871
							<b>Mean</b>	<b>1.028</b>	<b>Mean</b>	<b>1.056</b>	<b>Mean</b>	<b>1.030</b>	<b>Mean</b>	<b>0.973</b>
							Lowest	0.943	Lowest	0.968	Lowest	0.945	Lowest	0.871
							Highest	1.115	Highest	1.145	Highest	1.117	Highest	1.058

### 5.2.2.5 Reduction factor $k_p$

For geometries where the brace is subjected to single-sided compression, the influence of the reduction factor  $k_p$  is evaluated. This factor takes into account the reduction of the plastic joint capacity when the chord member is subjected to initial compression stresses, arising from compression or bending moments on the chord member. This reduction factor is based on the  $n_p$  factor, which takes into account the stress ratio between the acting stress ( $N_{p,Ed}$ ) in the chord divided by the yield strength ( $f_{y0}$ ), as shown in Equation 5.35. The factor  $k_p$  to consider, can be calculated with the following design rule:

$$\begin{aligned}
 &\text{For } n_p > 0 \text{ (compression): } k_p = 1 - 0.3 * n_p * (1 + n_p), \quad \text{but } k_p \leq 1.0 \\
 &\text{For } n_p \leq 0 \text{ (tension): } k_p = 1.0 \\
 &n_p = (\sigma_{p,Ed} / f_{y0}) / \gamma_{M5}, \quad (5.35)
 \end{aligned}$$

where  $\sigma_{p,Ed}$  is the maximum compressive stress in the chord at the joint, excluding the stress due to the axial forces in the brace at that joint. The stress can be calculated by  $\sigma_{p,Ed} = N_{p,Ed} / A_0 + M_{0,Ed} / W_{el,0}$ , where  $N_{p,Ed}$  is the design value of the internal axial force,  $A_0$  is the chord surface,  $M_{0,Ed}$  is the bending moment design value of the chord and  $W_{el,0}$  is the elastic section modulus of the chord member. [2] To calculate the maximum compressive stress in the chord at the joint, the bending moment present in the chord, which is due to the normal force in the brace, is implemented within the formula.

Taking into account the reduction factor  $k_p$  has significant influences on the plastic design resistances for penetrated CHS X-joints subjected to single-sided compression. Table 33 and the right graph of Figure 43, shows the results for the final four penetrated design rules for single-sided tension, where the reduction factor  $k_p$  is included. In the table can be seen that the calculated average RR of the design rules are between 1.45 to 1.52, which means that the plastic design resistances become very conservative. Comparing the results with the non-reduced resistances, provided in Table 32 and in the left graph of Figure 43, an average, lowest and highest RR of 1.03, 0.95, and 1.12, respectively, is found for the non-reduced design rule stress pattern 2b, whereas the reduction factor decreases the plastic design resistance to an average, lowest and highest RR to 1.50, 1.19, and 1.75, respectively.



It can be concluded that for geometries subjected to single-sided compression, the design rules “Stress pattern 2a” and “Stress pattern 2b”, well predict the plastic capacity obtained from FEA, with an average RR of 1.06 and 1.03, respectively, and that applying the reduction factor  $k_p$  to the design rules for the calculation of the plastic design resistances for geometries subjected to single-sided compression, results in significant underpredictions of the true plastic capacity, as follows from the average RR’s of approximately 1.50.

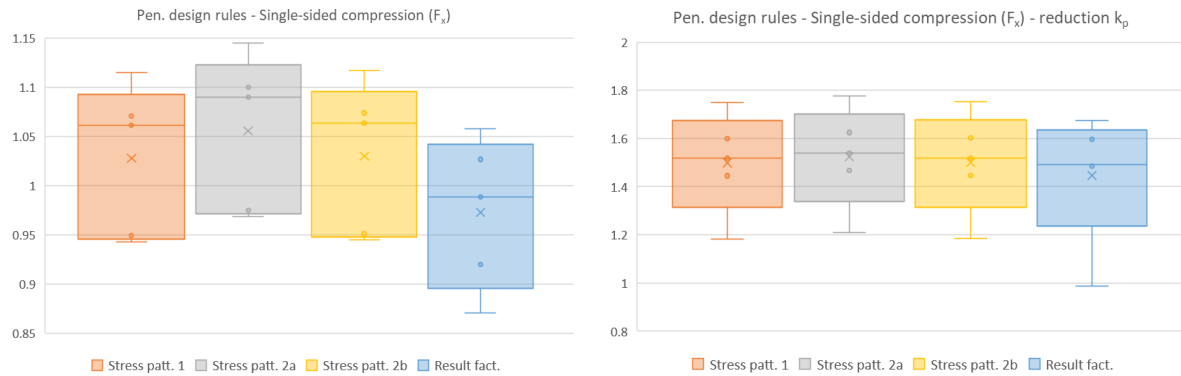


Figure 43: RR of the design rules for penetrated joints – Single-sided compression ( $F_x$ ) – standard (left) & reduced  $k_p$  (right)

Table 33: Results design rules for penetrated joints reduced by  $k_p$  factor – Single-sided compression ( $F_x$ )

Model			FEA results			Stress patt. 1		Stress patt. 2a		Stress patt. 2b		Result factors		
$\beta$	$2\gamma$	$2\delta$	$N_{1,FEA}$	Infl $\beta$	Infl $2\gamma$	Infl $2\delta$	$N_{1,Rd}$	RR	$N_{1,Rd}$	RR	$N_{1,Rd}$	RR	$N_{1,Rd}$	RR
0.8	30	30	6312.1		1.418	1.107	4159	1.518	4099	1.540	4154	1.519	4229	1.492
0.8	30	50	5699.8		1.480		3944	1.445	3884	1.467	3940	1.447	3837	1.486
0.8	50	30	4449.6			1.155	2541	1.751	2504	1.777	2539	1.753	2657	1.675
0.8	50	50	3850.9				2407	1.600	2370	1.625	2404	1.602	2412	1.597
0.2	50	10	1165.5				986	1.182	963	1.211	984	1.185	1182	0.986
							<b>Mean</b>	<b>1.499</b>	<b>Mean</b>	<b>1.524</b>	<b>Mean</b>	<b>1.501</b>	<b>Mean</b>	<b>1.447</b>
							Lowest	1.182	Lowest	1.211	Lowest	1.185	Lowest	0.986
							Highest	1.751	Highest	1.777	Highest	1.753	Highest	1.675

### 5.3 SHEAR $F_y$ (CHORD BENDING MOMENT)

To create a design rule for CHS X-joints subjected to shear  $F_y$  (chord bending moment), similar steps have been performed as for joints subjected to single-sided tension. In this paragraph, some additional simulations are performed and the results are evaluated, the steps to acquire the design rule are presented and the approximated failure mechanisms are verified.

#### 5.3.1 Additional simulations

The results of the parameter study for geometries subjected to shear  $F_y$  (chord bending moment), are elaborated in Paragraph 0. It has been seen that only three penetrated parameter configurations fail in chord face failure, which is too limited to design and fit a design rule on. With only three geometries to calibrate the design rule, it will very likely that the design rule does not describe the behavior and plastic design resistance of the geometries correctly. Therefore, additional simulations are performed for geometries with  $\beta$  factors 0.6 and 0.8,  $2\gamma$  factors 30, 40 and 50, and  $2\delta$  factors 10, 15 and 20. These geometrical parameters are chosen based on the three parameter configurations that fail in chord face failure, to ensure the boundaries of the critical areas where joint failures are common can be identified and more results are available for the creation and calibration of the new design rule. Table 34 shows the results for the additional simulations, of which eight parameter configurations are identified that fail in chord face failure.

Table 34: Additional simulations geometries subjected to shear  $F_y$

Model			$2\gamma$ 30				$2\gamma$ 40				$2\gamma$ 50			
Load	$\beta$	$2\delta$	$F_{y,FEA}$ (kN)	$F_{y,Rd}$ (kN)	RR	Failure mech.	$F_{y,FEA}$ (kN)	$F_{y,Rd}$ (kN)	RR	Failure mech.	$F_{y,FEA}$ (kN)	$F_{y,Rd}$ (kN)	RR	Failure mech.
Shear $F_y$ (Chord bending moment)	0.8	10	11165.0	2503	4.461	3 C ff	8181.7	1626	5.032	3 C ff	6380.1	1163	5.486	3 C ff
	0.8	15	8424.0	8105	1.039	1 B bm	8072.0	1626	4.964	3 C ff	6459.4	1163	5.554	3 C ff
	0.8	20	6444.8	6293	1.024	1 B bm	6353.2	6293	1.010	1 B bm	6284.2	1163	5.403	3 C ff
	0.6	10	6491.8	5637	1.152	1 B bm	6411.1	967	6.630	3 C ff	5255.9	692	7.595	3 C ff
	0.6	15	4593.3	4032	1.139	1 B bm	4475.1	4043	1.107	1 B bm	4443.6	4043	1.099	1 B bm
	0.6	20	3537.5	3131	1.130	1 B bm	3377.4	3131	1.079	1 B bm	3465.0	3131	1.107	1 B bm

#### 5.3.2 Design rule

After a first evaluation of the results presented in Table 34, it was concluded that the location at which the shear force is applied, has a significant influence on the joint capacity as well. Therefore, besides the standard varied geometrical parameters, also the lever arm of the shear force with respect to the chord member is varied, i.e. the eccentricity of the shear force with respect to the chord center axis,  $e_x$ , is varied. The results from the parameter and lever arm study for penetrated CHS X-joints subjected to shear  $F_y$ , are presented Table 35, Table 36 respectively and are both illustrated in Figure 45. In the tables, the plastic capacity observed in FEA and the influences of the geometrical parameters on the plastic capacity are shown. Next to that, the plastic design resistances according to the existing EC design rule for non-penetrated joint chord face failure (EC C ff) are shown, for which formula is provided in Equation 2.7. This design rule is actually meant for joints of which the brace is subjected to a moment, but is converted to a formula force formula by dividing the design moment resistance through the eccentricity of the shear force with respect to the chord center axis,  $e_x$ . With the converted design rule, the plastic design resistance to a shear force in y direction is calculated, and compared to the plastic capacity observed in FEA. An average, lowest and highest RR is observed of 5.64, 4.46 and 7.59, respectively, in case the geometrical parameters are varied (Table 35). While varying the lever arms,  $l_x$ , (Table 36), an average, lowest and highest RR of 6.20, 4.28, and 7.59, respectively, are found. This means that the design rules result in plastic design resistances that could on average be approximately 5.5 times as high.

To create a design rule that approximates the plastic capacity, the design rule “result factors” from Equation 5.34, is used as a basis. To take into account the influence of the application point of the force, the ratio between the chord diameter ( $d_0$ ) and the length between the point of application of the force and the farthest chord wall, as shown as  $L_1$  in Figure 44, is included. Next, the plastic design resistance of the design rule are fitted on the plastic capacity obtained from FEA, which is in this case done by including a factor 3 to the design rule. The established formula is then rewritten into a moment formulation, resulting in the design rule “Result factors shear  $F_y$ ”, which is provided in Equation 5.36. In Table 35, Table 36 and Figure 45 the results for this design rule are shown. It can be seen that the “Result factors shear  $F_y$ ” design rule results in an average RR of approximately 1.05.

Shear  $F_y$  (chord bending moment) – design rule “Result factors shear  $F_y$ ” for penetrated joints

$$F_{y,1,Rd} * L_1 = 3 * \frac{k_p * f_{y0} * t_0 * d_1 * d_0}{\sin \theta_1} / \gamma_{M5} \quad (5.36)$$

Table 35: Results design rules for penetrated joints – shear  $F_y$  – varied geometrical parameters

Model				FEA results			EC C ff		Result factors $F_y$		
$\beta$	$2\gamma$	$2\delta$	$e_x$	$F_{y,FEA}$	Infl $\beta$	Infl $2\gamma$	Infl $2\delta$	$F_{y,Rd}$	RR	$F_{y,Rd}$	RR
0.8	30	10	838	11165.0			1.364	2503	4.461	10306	1.083
0.8	40	10	838	8181.7			1.282	1626	5.032	7730	1.058
0.8	40	15	838	8072.0			1.250	1626	4.965	7730	1.044
0.8	50	10	838	6380.1			0.987	1163	5.484	6184	1.032
0.8	50	15	838	6459.4			1.027	1163	5.553	6184	1.045
0.8	50	20	838	6284.2				1163	5.402	6184	1.016
0.6	40	10	792	6411.1			1.220	967	6.628	6023	1.064
0.6	50	10	792	5255.9				692	7.594	4819	1.091
								<b>Mean</b>	<b>5.640</b>	<b>Mean</b>	<b>1.054</b>
								Lowest	4.461	Lowest	1.016
								Highest	7.594	Highest	1.091

Table 36: Results design rules for penetrated joints – shear  $F_y$  – varied eccentricity  $e_x$

Model				FEA results			EC C ff		Result factors $F_y$		
$\beta$	$2\gamma$	$2\delta$	$e_x$	$F_{y,FEA}$	Infl $\beta$	Infl $2\gamma$	Infl $2\delta$	$F_{y,Rd}$	RR	$F_{y,Rd}$	RR
0.8	50	10	381	10958.0				2559	4.282	9894	1.108
0.8	50	10	587	8369.6	1.294			1663	5.034	7793	1.074
0.8	50	10	792	6705.0	1.276			1231	5.446	6427	1.043
0.8	50	10	838	6380.1	1.287			1163	5.484	6184	1.032
0.8	50	10	938	5851.6				1039	5.630	5715	1.024
0.8	50	10	1038	5306.9	1.328			939	5.650	5312	0.999
0.6	40	10	792	6411.1			1.220	967	6.628	6023	1.064
0.6	40	10	838	6039.9			1.218	915	6.603	5798	1.042
0.6	50	10	587	6468.8				935	6.917	5844	1.107
0.6	50	10	792	5255.9				692	7.594	4819	1.091
0.6	50	10	838	4958.0				655	7.575	4639	1.069
0.6	50	10	1038	3995.3				528	7.561	3985	1.003
								<b>Mean</b>	<b>6.200</b>	<b>Mean</b>	<b>1.055</b>
								Lowest	4.282	Lowest	0.999
								Highest	7.594	Highest	1.108

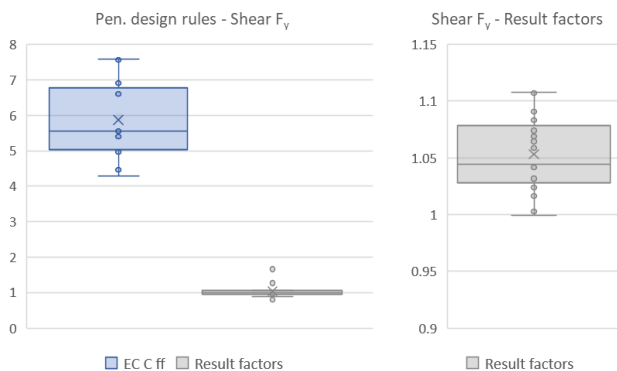


Figure 45: RR design rules for penetrated joints – Shear  $F_y$

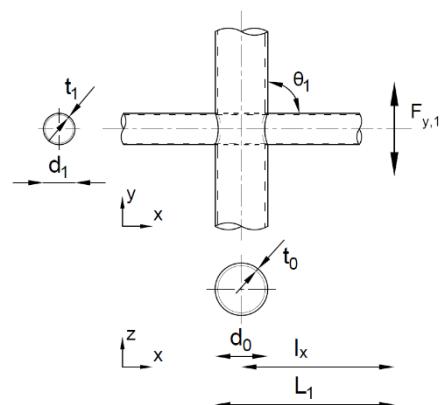


Figure 44: CHS X-joint subjected to shear  $F_y$

### 5.3.3 Verification of the governing failure mechanism

Table 37 and Table 38 shows the verification of the governing failure mechanism for geometries subjected to shear  $F_y$  for the design calculations executed according to the EC design rules for non-penetrated joints and the new improved design rules for penetrated joints, by comparing their results with the failure mechanisms and plastic capacity obtained by FEA. While in the existing EC design rules for non-penetrated joints the EC design rule for chord face failure is applied, in the new design rules for penetrated joints the design rule “result factors shear  $F_y$ ” is applied. Table 37 shows that for the existing EC design rules for non-penetrated joints several failure mechanisms are incorrect and deviate from the ones observed in FEA, while for the new design rule for penetrated joints, shown in Table 38, all failure mechanisms correspond to the ones in FEA. Furthermore, it can also be concluded that the calculated plastic design resistances obtained with the improved design rules for penetrated joints, better approximate the plastic capacity obtained from FEA.

### 5.3.4 Conclusion design rule Shear $F_y$

For the penetrated CHS X-joints subjected to shear  $F_y$  (chord bending moment), it can be concluded that the existing EC design rules for non-penetrated joints, with an average RR of 5.64 and 6.40, underestimate the plastic capacity of the joints significantly. Therefore, an improved design rule “Result factors shear  $F_y$ ” is created, which is based on the design rule “Result factors” for geometries subjected to single-sided tension. The improved design rule, as shown in Equation 5.36, approximates the plastic capacity from FEA very well. With the design rule an average RR is found of 1.05. Furthermore, it is concluded that by taking into account the new design rule in the design set, the correct governing failure mechanism is predicted. It is therefore advised to use the design rule “Result factors shear  $F_y$ ”, as given in Equation 5.36, for the design check of penetrated CHS X-joints subjected to shear  $F_y$ .

Table 37: Failure mechanism calculation results for existing EC design rules for non-penetrated joints

Model $2\gamma$ (-)	$2\delta$ (-)	$\beta$ 0.8				$\beta$ 0.6				$\beta$ 0.4				$\beta$ 0.2			
		EC		FEA		EC		FEA		EC		FEA		EC		FEA	
		$F_{y,Rd}$ (kN)	Failure mode	$F_{y,FEA}$ (kN)	Failure mode	$F_{y,Rd}$ (kN)	Failure mode	$F_{y,FEA}$ (kN)	Failure mode	$F_{y,Rd}$ (kN)	Failure mode	$F_{y,FEA}$ (kN)	Failure mode	$F_{y,Rd}$ (kN)	Failure mode	$F_{y,FEA}$ (kN)	Failure mode
10	10	6924	2 C ps	12554	1 B bm	4120	2 C ps			2070	2 C ps			559	1 B bm	514	1 B bm
10	30	4342	1 B bm	4328	1 B bm	2160	1 B bm			890	1 B bm			214	1 B bm	183	1 B bm
10	50	2677	1 B bm	2598	1 B bm	1332	1 B bm			549	1 B bm			132	1 B bm	107	1 B bm
30	10	2308	2 C ps	11165	3 C ff	1373	2 C ps	6492	1 B bm	690	2 C ps	2597	1 B bm	214	2 C ps	584	1 B bm
30	30	2308	2 C ps	4405	1 B bm	1373	2 C ps	2303	1 B bm	690	2 C ps			214	1 B bm	207	1 B bm
30	50	2308	2 C ps	2614	1 B bm	1332	1 B bm			549	1 B bm			132	1 B bm	124	1 B bm
50	10	1163	2 C ff	6380	3 C ff	692	2 C ff	5256	3 C ff	348	2 C ff	2614	1 B bm	108	2 C ff	591	1 B bm
50	30	1163	2 C ff	4350	1 B bm	692	2 C ff	2374	1 B bm	348	2 C ff			108	2 C ff	208	1 B bm
50	50	1163	2 C ff	2596	1 B bm	692	2 C ff			348	2 C ff			108	2 C ff	127	1 B bm

Table 38: Failure mechanism calculation results for new design rules for penetrated joints

Model $2\gamma$ (-)	$2\delta$ (-)	$\beta$ 0.8				$\beta$ 0.6				$\beta$ 0.4				$\beta$ 0.2			
		EC / Pen		FEA		EC / Pen		FEA		EC / Pen		FEA		EC / Pen		FEA	
		$F_{y,Rd}$ (kN)	Failure mode	$F_{y,FEA}$ (kN)	Failure mode	$F_{y,Rd}$ (kN)	Failure mode	$F_{y,FEA}$ (kN)	Failure mode	$F_{y,Rd}$ (kN)	Failure mode	$F_{y,FEA}$ (kN)	Failure mode	$F_{y,Rd}$ (kN)	Failure mode	$F_{y,FEA}$ (kN)	Failure mode
10	10	11332	1 B bm	12554	1 B bm	5637	1 B bm			2322	1 B bm			559	1 B bm	514	1 B bm
10	30	4342	1 B bm	4328	1 B bm	2160	1 B bm			890	1 B bm			214	1 B bm	183	1 B bm
10	50	2677	1 B bm	2598	1 B bm	1332	1 B bm			549	1 B bm			132	1 B bm	107	1 B bm
30	10	10306	3 C ff	11165	3 C ff	5637	1 B bm	6492	1 B bm	2322	1 B bm	2597	1 B bm	559	1 B bm	584	1 B bm
30	30	4342	1 B bm	4405	1 B bm	2160	1 B bm	2303	1 B bm	890	1 B bm			214	1 B bm	207	1 B bm
30	50	2677	1 B bm	2614	1 B bm	1332	1 B bm			549	1 B bm			132	1 B bm	124	1 B bm
50	10	6184	3 C ff	6380	3 C ff	4819	3 C ff	5256	3 C ff	2322	1 B bm	2614	1 B bm	559	1 B bm	591	1 B bm
50	30	4342	1 B bm	4350	1 B bm	2160	1 B bm	2374	1 B bm	890	1 B bm			214	1 B bm	208	1 B bm
50	50	2677	1 B bm	2596	1 B bm	1332	1 B bm			549	1 B bm			132	1 B bm	127	1 B bm

## 5.4 SHEAR $F_z$ (CHORD TORSIONAL MOMENT)

For the design rule for joints subjected to shear  $F_z$  (chord torsional moment), similar steps have been performed as for joints subjected to shear  $F_y$  (chord bending moment). In this paragraph, some additional simulations are performed and provided, the results are evaluated, the steps to acquire the design rule are presented and the governing failure mechanisms are verified.

### 5.4.1 Additional simulations

The results of the basic parameter study for geometries subjected to shear  $F_z$  (chord torsional moment), are shown in Paragraph 4.8. The results show that only four penetrated parameter configurations fail in chord face failure, which is too limited to create, fit and calibrate a design rule on. Therefore, similarly as done for the load case Shear  $F_y$ , additional simulations are performed, for which the results are shown in Table 39. In the table it can be seen that fourteen geometrical configurations fail in chord face failure.

### 5.4.2 Design rules

In Table 40, Table 41 and Figure 47 the results from the FEA and design rules are shown, including the influences of the geometrical parameters on the plastic capacity (FEA). In Table 40 the geometrical parameters are varied and in Table 41 the eccentricity of the shear force with respect to the chord center axis,  $e_x$ , is varied. The first design rule presented in the tables, is the existing EC design rule for non-penetrated joint chord face failure (EC C ff), as provided in Equation 2.8. Similarly as done for shear  $F_y$ , this formula is converted such that the design resistance is expressed in a shear force in Z-direction. This design rule results in an average, lowest and highest RR of 7.86, 4.66, and 11.7 for varying geometrical parameters and an average, lowest and highest RR of 9.45, 6.48, and 12.3, respectively, when the eccentricity is varied. This means that the plastic design resistance underestimates the plastic capacity of the joints on average by a factor of approximately 8.5.

A new design rule is therefore created, for which the proposed design rule for penetrated joints subjected to shear in y-direction, provided in Equation 5.36, is used as a basis. To fit the results of the design rule to the plastic capacity for penetrated joints subjected to shear in Z-direction, the factor 3.0 is changed into 1.7. Implementing this single adaptation leads to an average, lowest and highest RR of 1.04, 1.01, and 1.10, respectively, in case the geometrical parameters are varied (Table 40) and an average, lowest and highest RR of 1.03, 0.97, and 1.07, respectively, in case the lever arm  $e_x$  is varied (Table 41). It is therefore concluded that this new design rule, which is provided in Equation 5.37, accurately describes the plastic capacity and that the difference with the original design rule for non-penetrated joints is substantial as is seen in Figure 47.

Shear  $F_z$  (chord torsional moment) – design rule “Result factors shear  $F_z$ ” for penetrated joints

$$F_{z,1,Rd} * L_1 = 1.7 * \frac{k_p * f_{y0} * t_0 * d_1 * d_0}{\sin \theta_1} / \gamma_{M5} \quad (5.37)$$

Table 39: Additional simulations geometries subjected to shear  $F_z$

Model			2γ 30				2γ 40				2γ 50			
Load	$\beta$	$2\delta$	$F_{z,FEA}$ (kN)	$F_{z,Rd}$ (kN)	RR	Failure mech.	$F_{z,FEA}$ (kN)	$F_{z,Rd}$ (kN)	RR	Failure mech.	$F_{z,FEA}$ (kN)	$F_{z,Rd}$ (kN)	RR	Failure mech.
Shear $F_z$ (Chord torsional moment)	0.8	10	5979.6	1278	4.679	3 C ff	4515.2	719	6.280	3 C ff	3575.7	460	7.773	3 C ff
	0.8	15	5984.8	1278	4.683	3 C ff	4508.2	719	6.270	3 C ff	3604.7	460	7.836	3 C ff
	0.8	20	5958.8	1278	4.663	3 C ff	4477.4	719	6.227	3 C ff	3596.0	460	7.817	3 C ff
	0.6	10	5644.4	5637	1.001	1 B bm	3725.5	390	9.553	3 C ff	2839.2	250	11.357	3 C ff
	0.6	15	4253.6	4032	1.055	1 B bm	3765.5	390	9.655	3 C ff	2912.7	250	11.651	3 C ff
	0.6	20	3219.9	3131	1.028	1 B bm	3203.3	3131	1.023	1 B bm	2926.8	250	11.707	3 C ff

Table 40: Results design rules for penetrated joints – shear  $F_z$  – varied geometrical parameters

Model				FEA results			EC C ff		Result factors $F_z$		
$\beta$	$2\gamma$	$2\delta$	$e_x$	$F_{z,FEA}$	Infl $\beta$	Infl $2\gamma$	Infl $2\delta$	$F_{z,Rd}$	RR	$F_{z,Rd}$	RR
0.8	30	10	838	5979.6		1.324	0.999	1278	4.680	5840	1.024
0.8	30	15	838	5984.8		1.327	1.004	1278	4.684	5840	1.025
0.8	30	20	838	5958.8		1.330		1278	4.664	5840	1.020
0.8	40	10	838	4515.2	1.212	1.262	1.001	719	6.283	4380	1.031
0.8	40	15	838	4508.2	1.197	1.250	1.006	719	6.273	4380	1.029
0.8	40	20	838	4477.4		1.245		719	6.230	4380	1.022
0.8	50	10	838	3575.7	1.197		0.991	460	7.774	3504	1.020
0.8	50	15	838	3604.7	1.238		1.002	460	7.837	3504	1.029
0.8	50	20	838	3596.0	1.229		1.012	460	7.818	3504	1.026
0.8	50	30	838	3551.3				460	7.721	3504	1.013
0.6	40	10	792	3725.5		1.247	0.989	390	9.542	3413	1.092
0.6	40	15	792	3765.5		1.292		390	9.645	3413	1.103
0.6	50	10	792	2839.2			1.025	250	11.363	2731	1.040
0.6	50	15	792	2912.7			0.995	250	11.657	2731	1.067
0.6	50	20	792	2926.8				250	11.713	2731	1.072
								<b>Mean</b>	<b>7.859</b>	<b>Mean</b>	<b>1.041</b>
								Lowest	4.664	Lowest	1.013
								Highest	11.713	Highest	1.103

Table 41: Results design rules for penetrated joints – shear  $F_y$  – varied eccentricity  $e_x$

Model				FEA results			EC C ff		Result factors $F_z$		
$\beta$	$2\gamma$	$2\delta$	$e_x$	$F_{z,FEA}$	Infl $\beta$	Infl $2\gamma$	Infl $2\delta$	$F_{z,Rd}$	RR	$F_{z,Rd}$	RR
0.8	50	10	587	4258.9	1.207			657	6.484	4414	0.965
0.8	50	10	838	3575.7	1.197			460	7.774	3504	1.020
0.8	50	10	1038	3100.4	1.325			371	8.347	3011	1.030
0.6	50	10	587	3528.8				337	10.461	3310	1.066
0.6	50	10	792	2839.2				250	11.363	2731	1.040
0.6	50	10	1038	2340.7				191	12.270	2258	1.037
								<b>Mean</b>	<b>9.450</b>	<b>Mean</b>	<b>1.026</b>
								Lowest	6.484	Lowest	0.965
								Highest	12.270	Highest	1.066

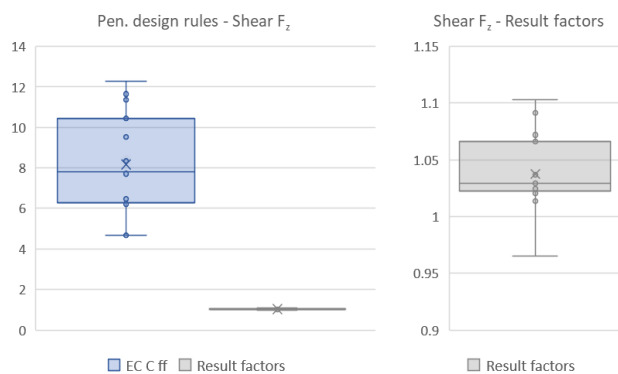


Figure 47: Results design rules for penetrated joints – Shear  $F_z$

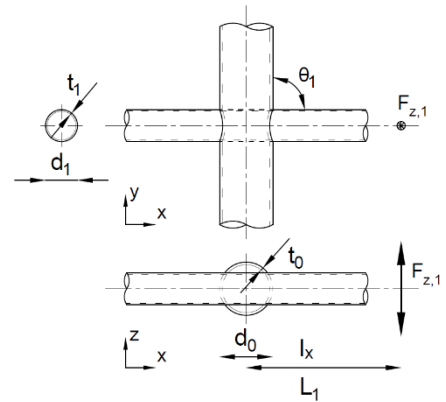


Figure 46: CHS X-joint subjected to shear  $F_z$

### 5.4.3 Verification of the failure mechanisms

In Table 42 and Table 43 the results of the verification procedure for the governing failure mechanisms as determined by the existing and new set of design rules, are shown. For the existing design set, of which the results are shown in Table 42, the non-penetrated EC chord face failure design rule is used, which is replaced by the “Result factors shear  $F_z$ ” design rule for shear ( $F_z$ ) (Equation 5.37) for the improved set of design rules for penetrated geometries (Table 43). Table 42 shows that with the existing EC design rules, an incorrect governing failure mechanism is predicted, while for the improved design rules for penetrated joints, most of the failure mechanisms are predicted correct, as can be seen in Table 43. For this set of design rules, only two failure mechanisms are predicted wrong, and for these geometries the design rule for chord face failure is slightly conservative, causing a failure mechanism with almost the same plastic design resistance to be selected as governing.

### 5.4.4 Conclusion design rule shear $F_z$

It can be concluded that for the penetrated CHS X-joints subjected to shear  $F_z$  (chord torsional moment), the existing EC design rules for non-penetrated joints, with an average of 7.86 and 9.45, underestimate the plastic capacity of penetrated CHS X-joints significantly. Therefore, a new design rule “Result factors shear  $F_z$ ” is created, which is provided in Equation 5.37. With this new design rules for penetrated joints, the plastic capacity of the penetrated joints is approximated very well, as follows from an average RR of approximately 1.04.

Additionally it is concluded from the verification of the failure mechanisms, that for the set of design rules in which the new design rules for penetrated joints is included, not only the plastic design resistance is in accordance with the capacity observed in FEA, but also the calculated governing failure mechanisms often corresponds with the failure mechanism observed in FEA. It is therefore proposed to use the new design rule “Result factors shear  $F_z$ ”, which is given in Equation 5.37, to calculate the design resistance of penetrated CHS X-joints subjected to shear in Z-direction.

Table 42: Failure mechanism calculation results for existing EC design rules for non-penetrated joints

Model 2 $\gamma$ 2 $\delta$ (-) (-)	$\beta$ 0.8				$\beta$ 0.6				$\beta$ 0.4				$\beta$ 0.2			
	EC		FEA		EC		FEA		EC		FEA		EC		FEA	
	$F_{z,Rd}$ (kN)	Failure mode	$F_{z,FEA}$ (kN)	Failure mode	$F_{z,Rd}$ (kN)	Failure mode	$F_{z,FEA}$ (kN)	Failure mode	$F_{z,Rd}$ (kN)	Failure mode	$F_{z,FEA}$ (kN)	Failure mode	$F_{z,Rd}$ (kN)	Failure mode	$F_{z,FEA}$ (kN)	Failure mode
10 10	6924	2 C ps	11467	1 B bm	4120	2 C ps			2070	2 C ps			559	1 B bm	519	1 B bm
10 30	4342	1 B bm	4166	1 B bm	2160	1 B bm			890	1 B bm			214	1 B bm	190	1 B bm
10 50	2677	1 B bm	2480	1 B bm	1332	1 B bm			549	1 B bm			132	1 B bm	113	1 B bm
30 10	1278	2 C ff	5980	3 C ff	694	2 C ff	5644	1 B bm	398	2 C ff	2558	1 B bm	199	2 C ff	581	1 B bm
30 30	1278	2 C ff	4244	1 B bm	694	2 C ff	2156	1 B bm	398	2 C ff			199	2 C ff	217	1 B bm
30 50	1278	2 C ff	2553	1 B bm	694	2 C ff			398	2 C ff			132	1 B bm	133	1 B bm
50 10	460	2 C ff	3576	3 C ff	250	2 C ff	2986	3 C ff	143	2 C ff	2342	1 B bm	72	2 C ff	569	1 B bm
50 30	460	2 C ff	3551	3 C ff	250	2 C ff	2156	1 B bm	143	2 C ff			72	2 C ff	215	1 B bm
50 50	460	2 C ff	2596	1 B bm	250	2 C ff			143	2 C ff			72	2 C ff	132	1 B bm

Table 43: Failure mechanism calculation results for new design rules for penetrated joints

Model 2 $\gamma$ 2 $\delta$ (-) (-)	$\beta$ 0.8				$\beta$ 0.6				$\beta$ 0.4				$\beta$ 0.2			
	EC / Pen		FEA		EC / Pen		FEA		EC / Pen		FEA		EC / Pen		FEA	
	$F_{z,Rd}$ (kN)	Failure mode	$F_{z,FEA}$ (kN)	Failure mode	$F_{z,Rd}$ (kN)	Failure mode	$F_{z,FEA}$ (kN)	Failure mode	$F_{z,Rd}$ (kN)	Failure mode	$F_{z,FEA}$ (kN)	Failure mode	$F_{z,Rd}$ (kN)	Failure mode	$F_{z,FEA}$ (kN)	Failure mode
10 10	11332	1 B bm	11467	1 B bm	5637	1 B bm			2322	1 B bm			559	1 B bm	519	1 B bm
10 30	4342	1 B bm	4166	1 B bm	2160	1 B bm			890	1 B bm			214	1 B bm	190	1 B bm
10 50	2677	1 B bm	2480	1 B bm	1332	1 B bm			549	1 B bm			132	1 B bm	113	1 B bm
30 10	5840	3 C ff	5980	3 C ff	4551	2 C ff	5644	1 B bm	2322	1 B bm	2558	1 B bm	559	1 B bm	581	1 B bm
30 30	4342	1 B bm	4244	1 B bm	2160	1 B bm	2156	1 B bm	890	1 B bm			214	1 B bm	217	1 B bm
30 50	2677	1 B bm	2553	1 B bm	1332	1 B bm			549	1 B bm			132	1 B bm	133	1 B bm
50 10	3504	3 C ff	3576	3 C ff	2731	2 C ff	2986	3 C ff	1974	2 C ff	2342	1 B bm	559	1 B bm	569	1 B bm
50 30	3504	3 C ff	3551	3 C ff	2160	1 B bm	2156	1 B bm	890	1 B bm			214	1 B bm	215	1 B bm
50 50	2677	1 B bm	2596	1 B bm	1332	1 B bm			549	1 B bm			132	1 B bm	132	1 B bm

## 5.5 COMBINATION OF LOAD CASES

### 5.5.1 Introduction

In addition to the standard load cases, the behavior of CHS X-joints is analyzed for two combined load cases. The performance and validity of the newly created design rules for joint failures in penetrated geometries are evaluated for these combined load cases. Furthermore it is checked, whether the design rule provided in the EC for the combination of load cases as given in Equation 2.11, can be applied for the new design rules for penetrated joints as well. In this design rule, the unity checks, i.e. the ratios between the design values and the design resistances, of the normal force in the brace ( $F_x$ ) and bending moments on the brace about the Y- ( $M_y$ ) and Z- ( $M_z$ ) axis are used. However, since the newly created design rules for joint failures of penetrated geometries are created for tension/compression and a shear force in Y- or Z-direction, the design rule from the EC (Equation 2.11) is converted so the unity checks from the new design rules can be used.

The resulting converted design rule for joint failures of penetrated geometries subjected to a combination of loads, is provided in Equation 5.38. To verify the results from this combination rule, when using the design resistances obtained with the new design rules for penetrated joints proposed in this research, the resistance ratios are used and entered in the combination rule, instead of the unity checks. The true capacity of the joints subjected to combined loads is in that case, approximated correctly (i.e. safely) by the design rules, if the resulting Resistance Ratio (RR) is equal or above 1.0. The formula for the resistance ratio is given in Equation 5.39.

In this paragraph, first the combination of shear  $F_y$  and shear  $F_z$  is analyzed, and secondly the combination of single-sided tension ( $F_x$ ), shear  $F_y$  and shear  $F_z$  is analyzed. For both combinations, first the FEA results are compared with the existing EC design rules for non-penetrated joints and next with the improved design rules for penetrated joints. In this paragraph only the comparisons between FEA and the design rules are shown in the tables. A total overview of the FEA results for both load combinations are given in Appendix E.

The non-penetrated comparisons are performed to get an indication of the conservatism of the existing EC design rules for non-penetrated joints, applied to penetrated geometries. The geometries for which the combination design rule is analyzed are ( $\beta$  0.8,  $2\gamma$  30/40/50,  $2\delta$  10), for these geometries, joint failures are governing for the individual load cases. In the FEA, the models are subjected to displacements of 100 mm in the indicated directions.

Converted design rule for the combination compression/tension & shear in  $F_y$  and  $F_z$

$$\frac{N_{x,1,Ed}}{N_{x,1,Rd}} + \left[ \frac{F_{y,1,Ed}}{F_{y,1,Rd}} \right]^2 + \frac{|F_{z,1,Ed}|}{F_{z,1,Rd}} \leq 1,0, \quad (5.38)$$

Resistance ratio for the validation of the converted design rule in 5.38

$$\frac{N_{x,1,FEA}}{N_{x,1,Rd}} + \left[ \frac{F_{y,1,FEA}}{F_{y,1,Rd}} \right]^2 + \frac{|F_{z,1,FEA}|}{F_{z,1,Rd}} \geq 1,0, \quad (5.39)$$

where  $N_{x,1,Ed}$ ,  $F_{y,1,Ed}$ ,  $F_{z,1,Ed}$ , are the design values for single-sided compression or tension ( $F_x$ ), shear in Y-direction ( $F_y$ ) and shear in Z-direction ( $F_z$ ),  $N_{x,1,Rd}$ ,  $F_{y,1,Rd}$ ,  $F_{z,1,Rd}$ , are the plastic design resistances from the design rules for single-sided compression or tension ( $F_x$ ), Shear in Y-direction ( $F_y$ ) and shear in Z-direction ( $F_z$ ), and  $N_{x,1,FEA}$ ,  $F_{y,1,FEA}$ ,  $F_{z,1,FEA}$ , are the plastic capacity for single-sided compression or tension ( $F_x$ ), Shear in Y-direction ( $F_y$ ) and shear in Z-direction ( $F_z$ ) obtained from FEA.

### 5.5.2 Combination of Shear $F_y$ and Shear $F_z$

#### 5.5.2.1 Introduction

For the load combination of shear  $F_y$  and shear  $F_z$ , a representation in which the location and directions of the applied displacements are shown in Figure 48. In this paragraph, first the combination check is performed using the existing EC design rules for non-penetrated joints, and next using the new design rules for penetrated joints. The plastic design resistances obtained with the design rules will be entered as the denominators in Equation 5.39. Since no tension or compression is imposed on the brace, the first ratio in Equation 5.39 is omitted and only  $F_{y,1,Rd}$  and  $F_{z,1,Rd}$  will be used.

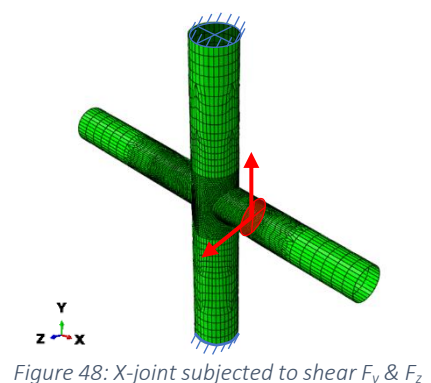


Figure 48: X-joint subjected to shear  $F_y$  &  $F_z$



### 5.5.2.2 Existing EC design rules for non-penetrated joints

In Table 44 the results of the FEA and the design rules are shown. From left to right the geometrical parameters, the plastic capacity according to FEA, the plastic design resistances to shear ( $F_y$ ) and shear ( $F_z$ ) as derived from the resistances to a bending moment in plane and out of plane, respectively, and the final RR for the combination rule are provided. The plastic capacity obtained from FEA are decomposed and provided in the Y-direction ( $F_y$ ) and Z-direction ( $F_z$ ). In the same rows, the plastic design resistances as calculated with the existing EC design rules for non-penetrated joints and the associated RR are given. The existing EC design rules for non-penetrated chord face failure (EC C ff) are applied, for which the moment design rules, as provided in Equation 2.7 and 2.8, are divided by  $e_x$ , the eccentricity of the shear force with respect to the chord center axis. In the last column, under “Combined RR”, the check for the combined resistance ratio, as provided in Equation 5.39, is applied. In this column it can be seen for each geometrical parameter configuration, to what extent the FEA capacity of the penetrated X-joint is approached by the design resistance according to the applied design set. At the bottom of the table, it can be seen that for these geometrical parameter configurations subjected to a combination of shear  $F_y$  and shear  $F_z$ , an average, lowest and highest RR is found of 22.2, 17.3, and 26.0, respectively. This means that the true plastic capacity of penetrated configurations are approximated very conservatively by the existing EC design rules for non-penetrated joints, and that plastic design resistances may have been obtained that are 22 times as high.

### 5.5.2.3 New design rules for penetrated joints

The improved design rules for penetrated joints are analyzed in a similar way as the EC design rules for non-penetrated joints. The results are shown in Table 45. For the combined design check, the new design rules for penetrated joints for shear  $F_y$  and shear  $F_z$ , which are provided in Equation 5.36 and 5.37, are applied. In the table, resistance ratios (RR) below 1.0 can be observed for the individual design rules. Though in normal cases, a RR value below 1 is undesired and considered unsafe, it is easily explainable and acceptable in this situation. The design rule calculates the plastic design resistance for joints subjected to merely a force in a single particular direction, while the capacity according to the FEA in these tables, is actually obtained for joints subjected to the evaluated load combination. Since the plastic capacity of the joint in a certain direction, is influenced by all imposed loads, it will be smaller as the capacity observed when subjected to only one of them, and therefore a partial RR below 1.0 is obvious and allowed, as long as the combined RR is above 1.0. When evaluating the combined RR, shown in the last column of the table, an average, lowest and highest combined RR of 1.34, 1.24, and 1.41, are found respectively. This means that the design rules has an average safety of 34%.

Table 44: Results existing EC design rules for non-penetrated joints – combination shear  $F_y$  and shear  $F_z$

Model				FEA results		ECc# M <sub>lp,1,Rd</sub> ( $F_y$ )		ECc# M <sub>op,1,Rd</sub> ( $F_z$ )		Combined RR	
$\beta$	$2\gamma$	$2\delta$	$e_x$		$F_{1,FEA}$	$F_{y,1,Rd}$	RR	$F_{z,1,Rd}$	RR	$\frac{(F_{y,1,FEA}/F_{y,1,Rd})^2 + F_{z,1,FEA}/F_{z,1,Rd}}{F_{z,1,FEA}/F_{z,1,Rd}}$	
0.8	30	10	838	$F_y$	9676.8	2503	3.866	1278	2.319	17.265	
				$F_z$	2962.4						
0.8	40	10	838	$F_y$	7326.5	1626	4.506	719	3.099	23.407	
				$F_z$	2226.9						
0.8	50	10	838	$F_y$	5544.7	1163	4.766	460	3.290	26.007	
				$F_z$	1513.1						
						Mean	4.380	Mean	2.902	Mean	22.226
						Lowest	3.866	Lowest	2.319	Lowest	17.265
						Highest	4.766	Highest	3.290	Highest	26.007

Table 45: Results design rules for penetrated joints – combination shear  $F_y$  and shear  $F_z$

Model				FEA results		Penc# Shear $F_y$		Penc# Shear $F_z$		Combined RR	
$\beta$	$2\gamma$	$2\delta$	$e_x$		$F_{1,FEA}$	$F_{y,1,Rd}$	RR	$F_{z,1,Rd}$	RR	$\frac{(F_{y,1,FEA}/F_{y,1,Rd})^2 + F_{z,1,FEA}/F_{z,1,Rd}}{F_{z,1,FEA}/F_{z,1,Rd}}$	
0.8	30	10	838	$F_y$	9676.8	10306	0.939	5840	0.507	1.389	
				$F_z$	2962.4						
0.8	40	10	838	$F_y$	7326.5	7730	0.948	4380	0.508	1.407	
				$F_z$	2226.9						
0.8	50	10	838	$F_y$	5544.7	6184	0.897	3504	0.432	1.236	
				$F_z$	1513.1						
						Mean	0.928	Mean	0.482	Mean	1.344
						Lowest	0.897	Lowest	0.432	Lowest	1.236
						Highest	0.948	Highest	0.508	Highest	1.407

### 5.5.3 Combination of Tension ( $F_x$ ), Shear $F_y$ and Shear $F_z$

#### 5.5.3.1 Introduction

In Figure 49 a representation is shown of a penetrated CHS X-joint subjected to a combination of tension ( $F_x$ ), shear  $F_y$ , and shear  $F_z$ . First the results from the FEA will be compared with the design resistances obtained with the existing EC design rules for non-penetrated joints, and next, the same analysis will be performed for the set of design rules for penetrated joints in which the new design rules created in this graduation research, are included. To obtain the overall RR for combined load cases, Equation 5.39 is used.

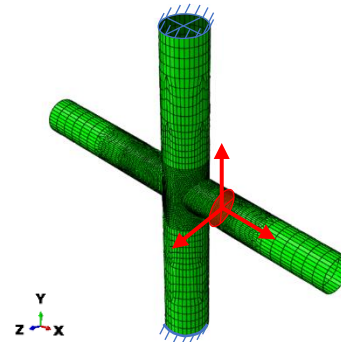


Figure 49: X-joint subjected to tension ( $F_x$ ), and shear  $F_y$  &  $F_z$

#### 5.5.3.2 Existing EC design rules for non-penetrated joints

Table 46 shows the results for the geometrical parameter configurations subjected to a combination of tension ( $F_x$ ), shear  $F_y$ , and shear  $F_z$ . In the table, next to the plastic capacity obtained from FEA, the design resistances according to the three relevant EC design rules are given; the EC design rule for chord face failure of non-penetrated geometries subjected to tension  $F_x$  ( $EC_{Cff} N_{1,Rd}(F_x)$ ), an in-plane bending moment ( $EC_{Cff} M_{ip,1,Rd}$  (converted to shear  $F_y$ )) and an out-of-plane bending moment ( $EC_{Cff} M_{op,1,Rd}$  (converted to shear  $F_z$ )), for which the EC design rules for non-penetrated joints are provided in Equation 2.5, 2.7 and 2.8. In the column “Combined RR”, it can be seen that for the geometrical parameter configurations, a combined RR is obtained with an average, lowest and highest value of 21.0, 16.5, and 25.5, respectively. This means that the plastic design resistances calculated with the EC design rules for non-penetrated joints could, on average, be 21 times as high.

#### 5.5.3.3 New design rules for penetrated joints

In a similar way as done for the EC design rules for non-penetrated joints, the results obtained with the new design rules for penetrated joints are evaluated, of which the results are shown in Table 47. The single-sided tension ( $F_x$ ) design rule, as given in Equation 5.33, the design rule for shear  $F_y$ , as given in Equation 5.36, and the design rule for shear  $F_z$ , as given in Equation 5.37, are applied. In Table 47, it can be seen that again the partial resistance ratios are below 1.0, as also was seen in Table 45 for the combined load case shear  $F_y$  and  $F_z$ . However, as explained in Paragraph 5.5.2.3, this is due to the interaction of the different load cases and the influence that has on the plastic capacity observed in FEA. It can be seen that the combination of the design rules for the geometrical configurations, results in an average, lowest and highest RR of 1.79, 1.71, and 1.86, respectively, which means that the combined design rules has an average safety factor of 79%.

Table 46: Results EC design rules for non-penetrated joints – combination single-sided tension ( $F_x$ ), shear  $F_y$  and shear  $F_z$

Model				FEA results		$EC_{Cff} N_{1,Rd}(F_x)$		$EC_{Cff} M_{ip,1,Rd}(F_y)$		$EC_{Cff} M_{op,1,Rd}(F_z)$		Combined RR	
$\beta$	$2\gamma$	$2\delta$	$e_x$	$N/F_{1,FEA}$	$N_{x,1,Rd}$	RR	$F_{y,1,Rd}$	RR	$F_{z,1,Rd}$	RR	$\frac{N_{x,1,FEA}/N_{x,1,Rd} + (F_{y,1,FEA}/F_{y,1,Rd})^2 + F_{z,1,FEA}/F_{z,1,Rd}}{N_{x,1,FEA}/N_{x,1,Rd} + (F_{y,1,FEA}/F_{y,1,Rd})^2 + F_{z,1,FEA}/F_{z,1,Rd}}$		
0.8	30	10	838	$N_x$	4471.8	4680	0.956					16.463	
				$F_y$	9174.1		2503	3.665					
				$F_z$	2650.5				1278	2.075			
0.8	40	10	838	$N_x$	3228.0	2788	1.158				21.087		
				$F_y$	6762.7		1626	4.160					
				$F_z$	1887.9				719	2.627			
0.8	50	10	838	$N_x$	2439.1	1866	1.307				25.470		
				$F_y$	5339.9		1163	4.590					
				$F_z$	1422.4				460	3.092			
					Mean	1.140	Mean	4.138	Mean	2.598	Mean	21.007	
					Lowest	0.956	Lowest	3.665	Lowest	2.075	Lowest	16.463	
					Highest	1.307	Highest	4.590	Highest	3.092	Highest	25.470	

Table 47: Results design rules for penetrated joints – combination single-sided tension ( $F_x$ ), shear  $F_y$  and shear  $F_z$

Model				FEA results		Penc# Tens. $F_x$		Penc# Shear $F_y$		Penc# Shear $F_z$		Combined RR	
$\beta$	$2\gamma$	$2\delta$	$e_x$		$N/F_{1,FEA}$	$N_{x,1,Rd}$	RR	$F_{y,1,Rd}$	RR	$F_{z,1,Rd}$	RR	$\frac{N_{x,1,FEA}/N_{x,1,Rd} + (F_{y,1,FEA}/F_{y,1,Rd})^2 + F_{z,1,FEA}/F_{z,1,Rd}}{}$	
0.8	30	10	838	$N_x$	4471.8	7241	0.618	10306	0.890	5840	0.454	1.864	
				$F_y$	9174.1								
				$F_z$	2650.5								
0.8	40	10	838	$N_x$	3228.0	5431	0.594	7730	0.875	4380	0.431	1.791	
				$F_y$	6762.7								
				$F_z$	1887.9								
0.8	50	10	838	$N_x$	2439.1	4345	0.561	6184	0.864	3504	0.406	1.713	
				$F_y$	5339.9								
				$F_z$	1422.4								
				Mean			0.591	Mean	0.876	Mean	0.430	<b>Mean</b>	<b>1.789</b>
				Lowest			0.561	Lowest	0.864	Lowest	0.406	Lowest	1.713
				Highest			0.618	Highest	0.890	Highest	0.454	Highest	1.864

#### 5.5.4 Conclusion combined load cases

For penetrated CHS X-joints subjected the a combination of compression/tension ( $F_x$ ), and shear in the Y- ( $F_y$ ) and Z- ( $F_z$ ) direction, several checks have been performed. First a check for the load combination shear  $F_y$  and shear  $F_z$  is performed for the existing EC design rules for non-penetrated joints and the new design rules for penetrated joints. In a similar way, the checks have been performed for the load combination single-sided tension ( $F_x$ ), shear  $F_y$ , and shear  $F_z$ .

It can be concluded that the combination rule (Equation 5.38) can be used with both the existing EC design rules for non-penetrated joints, as well as the new design rules for penetrated joints, to check the design resistance to the load combination of shear  $F_y$  and shear  $F_z$ , as well as to the load combination single-sided tension ( $F_x$ ), shear  $F_y$ , and shear  $F_z$ .

However, for X-joints subjected to a combination of shear  $F_y$  and shear  $F_z$ , the existing EC design rules for non-penetrated joints result in an average RR 22.2, which means that the design rule is very conservative and that the plastic design resistances could in fact be 22 times as high. Using the design rules for penetrated joints, an average RR of 1.34 is found, which means that the design rule will result in X-joints with an average overcapacity of 34%. For the combination of single-sided tension ( $F_x$ ), shear  $F_y$ , and shear  $F_z$ , the existing EC design rules for non-penetrated joints result in average RR of 21.0, which means that the resistances predicted could on average be 21 times higher. Using the new design rules for penetrated joints, an average RR of 1.79 is found, which means that with the new design rules a significant improvement in the approximation of the true capacity of CHS X-joints is obtained.

## 5.6 PENETRATED CHS X-JOINT DESIGN CHECKS

### 5.6.1 Introduction

To provide a complete overview of the various design checks to be performed, a calculation sheet has been created that includes the checks for joint, chord and brace failure mechanisms. The sheet from Witteveen+Bos, which was provided upon the start of this graduation project, has been used as the basis for this calculation sheet. This sheet contains the design checks for the brace and is, for the purpose of the calculation sheet supplemented by the design checks for the chord and joint failures. In this paragraph, the calculation sheet and the used design rules are explained. Furthermore, an extra calculation sheet is created for the casus of the mooring bollard from Witteveen+Bos, in which eccentricities are allowed for the application point of the imposed loads. The calculation sheet for penetrated CHS X-joints by which the design resistances for various load combinations are calculated for a certain geometrical parameter configuration is provided in Appendix G.1 and in Appendix G.2 the calculation sheet to verify the mooring bollard from Witteveen+Bos model is provided.

### 5.6.2 Penetrated CHS X-joint calculation sheet

For the computation of the plastic design resistance of a penetrated CHS X-joint, a calculation sheet is created that is divided into three parts. In the first part, the Design values are calculated, in the second part an overview of the material and sectional properties is given and in the third part the design checks are executed. Table 48 shows the first part concerning the design values, in which the applied load ( $F_{Ed}$ ), the eccentricity of the application point of the force the X-direction with respect to the chord axis ( $e_x$ ), and the chord length ( $L_0$ ) can be filled in. Based on these parameters, the load is applied in 5 directions in the horizontal plane ( $0^\circ, 45^\circ, 90^\circ, 135^\circ$  and  $180^\circ$ ), and in 3 directions in the vertical plane ( $m = 0^\circ, t = +45^\circ, b = -45^\circ$ ), causing the load to be applied to the brace in fifteen different directions. The applied load is then decomposed into the following axial loads and/or moments acting on the brace member: axial force ( $N_{Ed}$ ), shear force in Y- and Z-direction ( $V_{y,Ed}, V_{z,Ed}$ ), bending moment about the Z- and Y-axis ( $M_{z,Ed}, M_{y,Ed}$ ). Additionally, the sum of the bending moments ( $\sum M_{y,z,Ed}$ ), and the bending moment acting on the chord ( $M_{chord}$ ) are calculated and provided.

In the second part "Input material and sectional properties" the yield ( $f_y$ ) and ultimate ( $f_u$ ) strength, the chord and brace diameter and wall thickness ( $d_{0,1}, t_{0,1}$ ) and the joint properties ( $n_p, \theta_1$ , and  $\gamma_{M5}$ ) must be filled in. With these inputs, the material and sectional properties of the chord and brace member and the joint itself are calculated. For the material properties the yield strength ( $f_y$ ), tensile strength ( $f_u$ ), reduced yield strength for shear and torsion ( $f_{y,\tau}$ ), and partial safety factor M0 ( $\gamma_{M0}$ ) are calculated. For the sectional chord and brace properties the diameters ( $d_{0,1}$ ), wall thicknesses ( $t_{0,1}$ ), corrosion depth, effective diameters and wall thicknesses after reduction for corrosion ( $d', t'$ ) and diameter over thickness ratio for both members ( $2\gamma; 2\delta$ ) are given. Furthermore, the steel class, area ( $A$ ), shear area ( $A_v$ ), point of gravity, and the mechanical properties, i.e. the elastic and plastic section modulus ( $W_{el}, W_{pl}$ ), torsional modulus ( $W_T$ ), second moment of area ( $I_z; I_y$ ) and the polar moment of inertia ( $I_p$ ) are included for both the chord and the brace. To calculate the joint failures, the properties  $\beta, n_p$  and  $k_p$ , which takes into account the compression stresses in the chord member, the angle between the chord and the brace ( $\theta_1$ ) and partial safety factor M5 ( $\gamma_{M5}$ ) are added.

Table 48: Calculation of the Design values

Design values									
$F_{Ed}$	2190 kN		$e_x$	0.65 m		$L_0$	5.18 m		
nr	$\alpha_h$	$\alpha_v$	$N_{Ed}$	$V_{y,Ed}$	$V_{z,Ed}$	$M_{z,Ed}$	$M_{y,Ed}$	$\sum M_{y,z}$	$M_{chord}$
[-]	[°]	[°]	[kN]	[kN]	[kN]	[kNm]	[kNm]	[kNm]	[kNm]
m1	0	0	-2190	0	0	0	0	0	1418
m2	45	0	-1548	0	1548	0	1006	1006	1003
m3	90	0	0	0	2190	0	1423	1423	0
m4	135	0	1548	0	1548	0	1006	1006	1003
m5	180	0	2190	0	0	0	0	0	1418
t1	0	45	-1548	1548	0	1006	0	1006	1003
t2	45	45	-1095	1548	1095	1006	712	1233	709
t3	90	45	0	1548	1548	1006	1006	1423	0
t4	135	45	1095	1548	1095	1006	712	1233	709
t5	180	45	1548	1548	0	1006	0	1006	1003
b1	0	-45	-1548	-1548	0	-1006	0	1006	1003
b2	45	-45	-1095	-1548	1095	-1006	712	1233	709
b3	90	-45	0	-1548	1548	-1006	1006	1423	0
b4	135	-45	1095	-1548	1095	-1006	712	1233	709
b5	180	-45	1548	-1548	0	-1006	0	1006	1003

In the third part of the sheet, named “Design checks” which is shown in Table 49, the calculations for the brace, chord and joint design resistances are provided. For the calculation of the design resistances to gross cross-section failures of the chord and brace, the formulas as provided in chapter 6 from the NEN-EN 1993-1-1 are applied. [17] The resistances of the chord and brace cross-section are checked for the acting normal force ( $N_{Ed}$ ), Bending moment ( $M_{Ed}$ ), Shear force ( $V_{Ed}$ ), torsional moment ( $T_{Ed}$ ), combination of torsion and shear ( $V_{pl,T,Ed}$ ), combination of bending moment and normal force ( $M_{N,pl,Ed}$ ) and a combination of bending moment, shear force and normal force. For the calculation of the gross cross-section resistance of the brace, the torsional moment and combination of torsional moment and shear have been omitted, since these load combinations are not present in the brace member.

The normal force can be checked for a tension and compression force, for which in chapter 6.2.3 and 6.2.4 from the EC is stated that the design value of the normal force ( $N_{Ed}$ ) must be equal to or smaller than the plastic design resistance of the gross cross-section ( $N_{pl,Rd}$ ). The plastic design resistance of the gross cross-section can be calculated by multiplying the area ( $A$ ) with the yield strength ( $f_y$ ) divided by the partial safety factor ( $\gamma_{M0}$ ).

The design resistance check of the bending moment is provided in EC chapter 6.2.5, in which it is stated that the design value of the bending moment ( $M_{Ed}$ ) must be equal to or smaller than the plastic design resistance to a bending moment ( $M_{pl,Rd}$ ). The plastic design moment resistance can be calculated by multiplying the plastic section modulus ( $w_{pl}$ ) with the yield strength ( $f_y$ ) and the division by the partial safety factor ( $\gamma_{M0}$ ).

The shear force is calculated in the same manner, the design value of the shear force ( $V_{Ed}$ ) must be equal to or smaller than the plastic design shear resistance ( $V_{pl,Rd}$ ), as provided in chapter 6.2.6. The plastic design shear resistance can be calculated by multiplying the shear area ( $A_v$ ) by the reduced yield strength for shear and torsion ( $f_{y,\tau}$ ) and dividing it by the partial safety factor ( $\gamma_{M0}$ ). The shear area for circular hollow sections is two times the area divided by  $\pi$ , and the reduced yield strength for shear and torsion can be calculated by dividing the yield strength ( $f_y$ ) by the square root of 3 ( $\sqrt{3}$ ). [18]

Torsion is approached in the same way as shear, as stated in chapter 6.2.7, the torsional design value ( $T_{Ed}$ ), also called ( $M_x$ ), must be equal to or less than the torsional design resistance of the cross-section ( $T_{Rd}$ ). In the calculation sheet, the torsional design resistance is calculated by multiplying the torsional modulus ( $W_T$ ) with the reduced yield strength ( $f_{y,\tau}$ ) and dividing it by the partial safety factor ( $\gamma_{M0}$ ). Where the torsional section modulus ( $W_T$ ) equals two times the elastic section modulus ( $W_{el}$ ).

The combined torsional moment and shear force can be checked by dividing the design value of the shear force ( $V_{Ed}$ ) by the plastic shear resistance that is reduced due to the effects of the imposed torsional moment ( $V_{pl,T,Rd}$ ), as provided in EC chapter 6.2.7. For the reduced plastic shear resistance, the NEN-EN 1993-1-1 gives the following formula:

$$V_{pl,T,Rd} = \left[ 1 - \frac{\tau_{t,Ed}}{f_y/\sqrt{3}/\gamma_{M0}} \right] * V_{pl,Rd}, \quad (5.40)$$

where the torsional shear stress ( $\tau_{t,Ed}$ ) is calculated by multiplying the torsional design value ( $T_{Ed}$ ) with the radius ( $r$ ) and dividing that by the polar moment of inertia ( $I_p = 2 \cdot I_{y,z}$ ) [17]

The combination of a bending moment and an axial force can be checked by dividing the design value of the bending moment ( $M_{Ed}$ ) by  $M_{N,Rd}$ , for which, in the NEN-EN 1993-1-1 Dutch national annex [19] the following formula is given:

$$M_{N,Rd} = M_{pl,Rd} * 1,04 * \left[ 1 - (N_{Ed}/N_{pl,Rd})^{1,7} \right], \quad (5.41)$$

Where  $M_{pl,Rd}$  is the plastic moment resistance,  $N_{Ed}$  the normal force design value and  $N_{pl,Rd}$  the plastic normal force design resistance.

For the design check of the interaction between the bending moment, shear force and normal force the Dutch national annex of the NEN-EN 1993-1-1 [19] gives the following formula:

$$\frac{M_{Ed}}{1,04 * \frac{q * M_{pl,Rd}}{\gamma_{M0}}} + \left( \frac{N_{Ed}}{q * N_{pl,Rd}} \right)^{1,7} \leq 1,0, \quad (5.42)$$

where:

$$q = 1,03 * \sqrt{1 - \left( \frac{V_{Ed}}{V_{pl,Rd}} \right)^2}. \quad (5.43)$$

Where  $q$  represents a reduction factor based on the shear force present in the member. [19]

Next to checks for basic cross-section failures, joint failures are checked using the new design rules for penetrated joints as presented in this research. The design rule “Stress pattern 2b”, as provided in Equation 5.33, is calculate the design resistance to single-sided tension/compression ( $F_x$ ), and for the design resistance to shear in the Y-direction ( $F_y$ ) and Z-direction ( $F_z$ ), Equation 5.36 and Equation 5.37 are applied, respectively. Finally, Equation 5.38, is used to check the resistance joint failures under combined loads.

From the different chord and brace gross cross-section calculations and the joint failure calculations, the governing UC is provided as the final line of the calculation sheet.

Table 49: Design checks chord gross cross-section and joint failures

Chord gross cross-section	Joint failures
<p><b>Normal force (article 6.2.3)</b></p> $N_{Ed}$ $N_{pl,Rd} = f_y \cdot A / \gamma_{M0}$ $UC_{pl} = N_{Ed} / N_{pl,Rd}$	<p><b>Chord face failure tension (<math>F_x</math>)</b></p> $N_{Ed}$ Input ( $N_{Ed}$ ) $Pen_{Cff,x} = 1.1 \cdot (k_p \cdot f_{y0} \cdot t_0 \cdot d_1 \cdot f_\delta \cdot f_\beta) / \sin\theta_1 / \gamma_{M5}$ $f_\delta = 1 + (50 - 2\delta) / 200$ $f_\beta = (\sin(0.65 \cdot \beta \cdot \pi) - \beta) + 0.8$ $UC_{Cff,x} = N_{Ed} / Pen_{Cff,x}$
<p><b>Bending moment (article 6.2.5)</b></p> $M_{Ed,resultant}$ $M_{pl,Rd} = f_y \cdot W_{pl} / \gamma_{M0}$ $UC_{pl} = M_{Ed} / M_{pl,Rd}$	<p><b>Chord face failure shear <math>F_y</math></b></p> $V_{y,Ed,1}$ Input ( $V_{y,Ed}$ ) $Pen_{Cff,y} = 3 \cdot (k_p \cdot f_{y0} \cdot t_0 \cdot d_1 \cdot d_0) / (L_1 \cdot \sin\theta_1) / \gamma_{M5}$ $UC_{Cff,y} = V_{y,Ed} / Pen_{Cff,y}$
<p><b>Shear force (article 6.2.6)</b></p> $V_{Ed,resultant} = \sqrt{V_{z,Ed}^2 + V_{y,Ed}^2}$ $\tau_{v,Ed} = V_{Ed} \cdot \sqrt{3} / A_v$ $\tau_{v,Ed} = V \cdot S / I \cdot t = V_{Ed} \cdot A / 2 \cdot a_{grav} / t_{calc} \cdot 2 \cdot I_y$ $V_{pl,Rd} = A_v \cdot f_{y,t}$ $UC_{pl} = V_{Ed} / V_{pl,Rd}$	<p><b>Chord face failure shear <math>F_z</math></b></p> $V_{z,Ed,1}$ Input ( $V_{z,Ed}$ ) $Pen_{Cff,z} = 1.7 \cdot (k_p \cdot f_{y0} \cdot t_0 \cdot d_1 \cdot d_0) / (L_1 \cdot \sin\theta_1) / \gamma_{M5}$ $UC_{Cff,z} = V_{z,Ed} / Pen_{Cff,z}$
<p><b>Torsion (article 6.2.7)</b></p> $T_{Ed}$ Input ( $M_{y,Ed}$ ) $\tau_{t,Ed} = T_{Ed} \cdot r / I_p$ $T_{pl,Rd} = W_t \cdot f_y$ $UC_{pl} = T_{Ed} / T_{pl,Rd}$	
<p><b>Combination of torsion with shear force (article 6.2.7.9)</b></p> $V_{pl,T,Rd} = [1 - (\tau_{t,Ed} / f_{y,t}) \cdot V_{pl,Rd}]$ $UC_{pl} = V_{Ed} / V_{pl,T,Rd}$	
<p><b>Combination bending and normal force (article 6.2.9.1)</b></p> $M_{Ed,resultant}$ $M_{N,pl,Rd} = M_{pl,Rd} \cdot 1.04 \cdot (1 - (N_{Ed} / N_{c,Rd})^{1.7})$ $UC_{pl} = M_{Ed,res} / M_{N,pl,Rd}$	
<p><b>Combination bending, shear and normal force (article 6.2.10)</b></p> $q = 1.03 \cdot \sqrt{1 - (V_{Ed} / V_{pl,Rd})^2}$ $UC_{pl} = M_{Ed} / (1.04 \cdot (q \cdot M_{pl,Rd} / \gamma_{M0}) + (N_{Ed} / (q \cdot N_{pl,Rd} / \gamma_{M0})))^{1.7}$	<p><b>Combination tension (<math>F_x</math>), shear <math>F_y</math> and <math>F_z</math></b></p> $UC = UC_{Cff,x} + (UC_{Cff,y})^2 + UC_{Cff,z}$
<b>UC<sub>Chord gross cross-section</sub></b>	<b>UC<sub>joint failures</sub></b>

### 5.6.3 Combination design rule torsional moment and shear

The calculation sheet is validated by FE simulations for different geometrical parameter configurations and load cases. In the calculation sheet the maximum plastic design resistance can be derived by making use of the “solver” function in Excel, which in this case, increases or decreases the applied force till the governing UC equals 1.0. The plastic design resistances are compared with the plastic capacity obtained from FEA, where in most cases, the plastic capacity and the corresponding failure mechanisms are approximated quite well.

However, it has also been found that specifically for geometries loaded in shear  $F_z$  (chord torsional moment), a failure mechanism appears to be governing that was not taken into account in the parameter study: failing of the chord member due to a combination of a torsional moment and shear, as described in the NEN-EN 1993-1-8 [2] article 6.2.7.9. This failure mechanism was not included in the parameter study, as initially the failure mechanism did not appear to be governing, and the plastic design resistance ( $V_{T,Rd}$ ) to be calculated, depends on the design value of the shear force ( $V_{z,Ed}$ ), and could therefore not be calculated manually in advance.

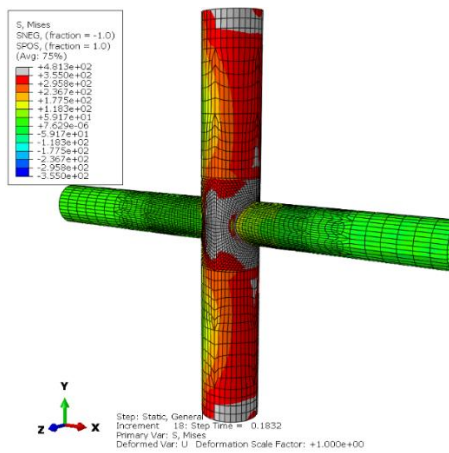


Figure 51: Geometry Von Mises stresses

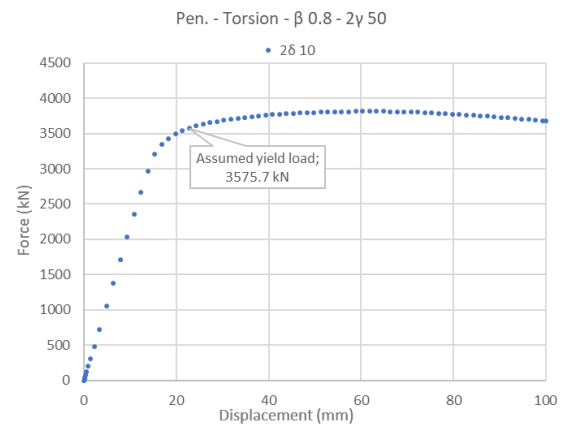


Figure 50: Load-displacement graph

An example of a geometrical parameter configuration where this load combination is governing is  $\beta$  0.8 –  $2\gamma$  50 –  $2\delta$  10. In Figure 51 the Von Mises stresses from Abaqus are shown and in Figure 49 the corresponding load-displacement graph is given.

In the graph it can be seen that for this geometry, a plastic capacity of 3575 kN is reached. Based on the principles for identifying the governing failure mechanism as outlined in Paragraph 4.3, chord face failure was assumed to be the governing failure mechanism for this geometry during the parameter study. Based on this result, and the other geometrical configurations failing on chord face failure, the design rules for penetrated joints for CHS X-joints subjected to shear  $F_z$  (chord torsional moment) is created, which for this specific geometry predicts a plastic design resistance of 3628 kN.

When using the calculation sheet, a governing plastic design resistance of 2190 kN is found instead, since also the design resistance to failure in a combination of a torsional moment and shear is calculated. However, when comparing this governing plastic design resistance to the true plastic capacity observed in FEA of 3575 kN, it is concluded that this true capacity is underpredicted significantly by the latter design rule (combination of torsional moment and shear) and approximated much better by the design resistance calculated with the new design rule for CFF in shear  $F_z$ .

This comparison has also been performed for all other geometrical parameter configurations evaluated in Paragraph 5.4.1, from which it is concluded that the combination of a torsional moment and shear (C T+S), is governing for more parameter configurations, especially for the ones with a higher  $\beta$  factor (0.6 or 0.8), since for these configurations, the brace and joint capacity are increased significantly due to the increase in brace diameter. This is illustrated for the parameter configurations with  $\beta$  factor 0.8 in Table 50.

For every geometrical parameter configuration in this table, it is checked whether the combination of torsional moment and shear would be governing over the failure mechanism that is initially predicted with the set of design rules for penetrated joints. This is done by calculating what the reduced plastic design resistance to C T+S ( $V_{pl,\tau,Rd}$ ) according to Equation 5.41 would have been, if the plastic design resistance according to the set of design rules for penetrated joints,  $F_{z,Rd}$ , would have been applied as  $V_{Ed}$ . With  $V_{Ed}$  the torsional moment and corresponding stress are calculated and these are used to reduce the  $V_{pl,Rd}$  to  $V_{pl,\tau,Rd}$ .

For the parameter configurations for which then the ratio  $F_{z,Rd}/V_{pl,\tau,Rd}$  is above 1.0, marked in Table 50, the plastic design resistance according to the design rules for penetrated joints can not be reached, since failure due to a C T+S will occur first. For these parameter configurations, the plastic design resistance for a combination of a torsional moment and shear is determined, by using the solver function in Excel to adjust the design value ( $V_{Ed}$ ) till the UC between this value and the reduced shear resistance ( $V_{pl,\tau,Rd}$ ) becomes 1.0. The resulting value for  $V_{pl,\tau,Rd}$  is given under "Design resist. 1 C T+S" (in which 1 refers to failure group 1). Additionally, in the last column of the table, the resistance ratio between the plastic capacity obtained from FEA ( $F_{z,FEA}$ ) and the approximated plastic design resistance for the failure due to a combination of a torsional moment and shear ( $V_{pl,\tau,Rd}$ ), is shown. It can be seen that the failure mechanism "combination of torsional moment and shear" approximates plastic design resistances with RR's of 1.19 to 1.69, which means that the calculated plastic design resistances should have been 19 to 69% higher.

Table 50: Results check combination torsional moment and shear

Model			FEA $F_{z,FEA}$ (kN)	Check governing failure mechanism Set design rules pen.		1 C T+S		Design resist. 1 C T+S	
$\beta$	$2\gamma$	$2\delta$		Failure mech.	$F_{z,Rd}$ (kN)	$V_{pl,T,Rd}$ (kN)	$F_{z,Rd}/V_{\tau,Rd}$	C T+S $V_{pl,T,Rd}$ (kN)	RR $F_{z,FEA} / V_{pl,T,Rd}$
0.8	10	10	11467.4	1 B bm	11332.0	6412.2	1.77	9215.5	1.26
0.8	10	30	4165.5	1 B bm	4341.5	15671.1	0.28		
0.8	10	50	2479.8	1 B bm	2676.6	17876.4	0.15		
0.8	30	10	5979.6	2 C ff	5840.3	650.1	9.30	3549.2	1.68
0.8	30	15	5984.8	2 C ff	5840.3	650.1	9.30		
0.8	30	20	5958.8	2 C ff	5840.3	650.1	9.30		
0.8	30	30	4244.3	1 B bm	4341.5	2629.3	1.65	3549.2	1.20
0.8	30	50	2552.9	1 B bm	2676.6	4562.2	0.59		
0.8	40	10	4515.2	2 C ff	4380.2	624.0	7.27	2708.8	1.67
0.8	40	15	4508.2	2 C ff	4380.2	624.0	7.27		
0.8	40	20	4477.4	2 C ff	4380.2	624.0	7.27		
0.8	50	10	3575.7	2 C ff	3504.2	564.2	6.43	2189.8	1.63
0.8	50	15	3604.7	2 C ff	3504.2	564.2	6.43		
0.8	50	20	3596.0	2 C ff	3504.2	564.2	6.43		
0.8	50	30	3551.3	2 C ff	3504.2	564.2	6.43	2189.8	1.62
0.8	50	50	2595.7	1 B bm	2676.6	1639.5	1.63		

The new design rule “Result factors – Shear  $F_z$ ” for penetrated joint failure is created, fitted and calibrated on the FEA results from Abaqus and therefore results in plastic design resistances that fit well to the plastic capacity observed in FEA. However, after the above finding it can be concluded that according to the complete set of design rules, the combination of a torsional moment and shear is governing for multiple geometrical parameter configurations. In Table 50 it can, however, be seen that this design rule underpredicts the true plastic capacity while this capacity is approximated correctly by the new design rule for penetrated chord face failure. It is therefore stated that this new CFF design rule for penetrated joints subjected to shear  $F_z$  also captures the resistances for failure due to a combination of torsional moment and shear and thus eliminates the existing (too conservative) rule for combined torsional moment and shear.



### 5.6.4 Case study | Mooring bollard Witteveen+Bos

To be able to check the mooring bollard of Witteveen+Bos, as shown in Figure 52, the calculation sheet has been adjusted to allow for eccentricities in the Y- and Z-direction ( $e_y = 375\text{mm}$ , and  $e_z = 450\text{mm}$ ). Due to these eccentricities, the additional bending and torsional moments are introduced in the joint. Figure 53 elaborates on the calculation of these additional bending and torsional moments. Eventually, the following forces & moments that are acting on the brace, have to be taken into account:

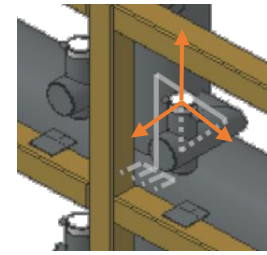


Figure 52: Model Witteveen+Bos

- |   |                                      |  |
|---|--------------------------------------|--|
| - Single-sided tension/compr. ( $F_x$ ) | - Shear $F_y$ (chord bending moment) | - Shear $F_z$ (chord torsional moment) |
| - $N_{Ed}$                              | - $V_{y,Ed}$                         | - $V_{z,Ed}$                           |
| - $M_{z,Ed}$ ( $F_{x,Ed} * e_y$ )       | - $M_{x,Ed}$ ( $V_{y,Ed} * e_z$ )    | - $M_{x,Ed}$ ( $V_{z,Ed} * e_y$ )      |
| - $M_{y,Ed}$ ( $F_{x,Ed} * e_z$ )       |                                      |  |

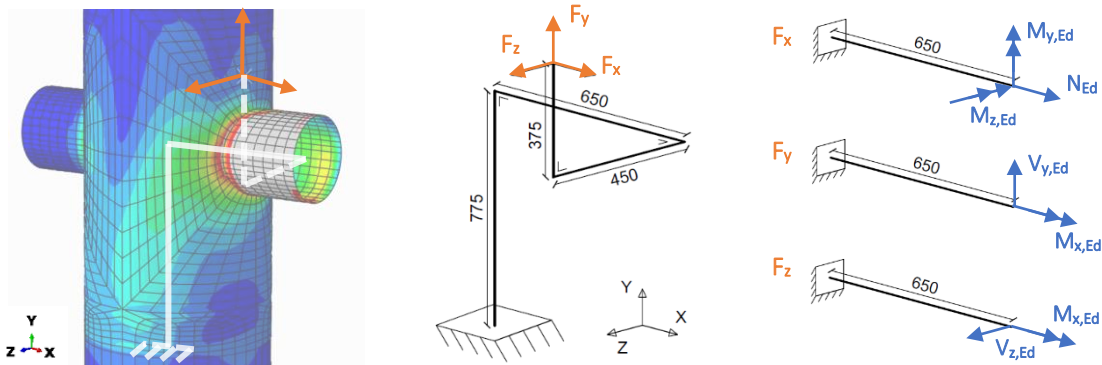


Figure 53: Mechanical scheme and acting forces

The influence of the design values  $N_{Ed}$ ,  $V_{y,Ed}$  and  $V_{z,Ed}$  on the resistance of the bollard to joint failures, is taken into account in the combination rule for joint failures of penetrated CHS X-joints given in Equation 5.38. However, for the additional bending and torsional moments ( $M_z$ ,  $M_y$ , and  $M_x$ ) acting on the brace member of the mooring bollard structure, no joint failure design rules are available. Therefore, two alternative methods have been determined to take into account the stresses caused by them.

The first method takes into account the additional bending moments about the Z- and Y-axis, by dividing the bending moment by the eccentricity in the X-direction. By doing so, additional forces in the Y- and Z-direction are obtained ( $V_{y,Ed,2} = M_z/e_x$  and  $V_{z,Ed,2} = M_y/e_x$ ), which can be coped for in the design rules for penetrated joints subjected to shear  $F_y$  and shear  $F_z$ . These additional forces are added to the initial shear forces  $V_{y,z,Ed,1}$ , as can be seen in the formulas in the left part of Table 51. The torsional moment ( $M_x$ ) on the brace, is taken into account by a bending moment about the X-axis that acts halfway the chord length. The UC for the bending moment on the chord can be calculated by dividing the acting bending moment ( $M_x$ ) by the bending moment resistance - ( $M_{pl,Rd}$ ). The computed value for the UC  $M_x/M_{pl,Rd}$ , is added to the combination rule, as can be seen at the bottom of the left part of Table 51. A disadvantage of this method is that for the bending moment about the Z- and Y-axis, also extra shear forces in Y- and Z-direction are introduced, which in reality do act on the brace member of the mooring bollard; those forces are in fact merely a byproduct of the way the bending moments  $M_y$  &  $M_z$  are accounted for.

For the second method, the bending moment  $M_x$  is processed exactly the same as for method one, but now the same procedure is used for the bending moment about the Z- and Y-axis as well. For bending moment about the Z-axis, a unity check is computed in a similar way as done for the bending moment about the X-axis; by dividing the acting bending moment ( $M_z$ ) by the bending moment resistance of the chord ( $M_{pl,Rd}$ ). For the bending moment about the Y-axis, which acts as a torsional moment on the chord, the unity check is calculated using the torsional moment resistance of the chord ( $T_{pl,Rd}$ ) instead of the bending moment resistance. The additional UC's for the bending moments  $M_x$  &  $M_y$  are included in the combination rule, and, in correspondence to the basic combination formulas provided in the EC, the square of the UC associated with  $M_z$  is added to the combination rule.

Table 51: Design checks – joint failures method 1 & 2

Joint failures method 1		Joint failures method 2	
<b>Chord face failure tension (<math>F_x</math>)</b>		<b>Chord face failure tension (<math>F_x</math>)</b>	
$N_{Ed}$	Input ( $N_{Ed}$ )	$N_{Ed}$	Input ( $N_{Ed}$ )
$Pen_{Cff,x}$	$1.1 \cdot (k_p \cdot f_{y0} \cdot t_0 \cdot d_1 \cdot f_\delta \cdot f_\beta) / \sin\theta_1 / \gamma_{M5}$	$Pen_{Cff,x}$	$1.1 \cdot (k_p \cdot f_{y0} \cdot t_0 \cdot d_1 \cdot f_\delta \cdot f_\beta) / \sin\theta_1 / \gamma_{M5}$
$f_\delta$	$1 + (50 - 2\delta) / 200$	$f_\delta$	$1 + (50 - 2\delta) / 200$
$f_\beta$	$(\sin(0.65 \cdot \beta \cdot \pi) - \beta) + 0.8$	$f_\beta$	$(\sin(0.65 \cdot \beta \cdot \pi) - \beta) + 0.8$
$UC_{Cff,x}$	$N_{Ed} / Pen_{Cff,x}$	$UC_{Cff,x}$	$N_{Ed} / Pen_{Cff,x}$
<b>Chord face failure shear <math>F_y</math></b>		<b>Chord face failure shear <math>F_y</math></b>	
$V_{y,Ed,1}$	Input ( $V_{y,Ed}$ )	$V_{y,Ed}$	Input ( $V_{y,Ed}$ )
$V_{y,Ed,2}$	$F_{x,Ed} \cdot e_y / e_x$	$Pen_{Cff,y}$	$3 \cdot (k_p \cdot f_{y0} \cdot t_0 \cdot d_1 \cdot d_0) / (L_1 \cdot \sin\theta_1) / \gamma_{M5}$
$V_{y,Ed,tot}$	$V_{y,Ed,1} + V_{y,Ed,2}$	$UC_{Cff,y}$	$V_{y,Ed} / Pen_{Cff,y}$
$Pen_{Cff,y}$	$3 \cdot (k_p \cdot f_{y0} \cdot t_0 \cdot d_1 \cdot d_0) / (L_1 \cdot \sin\theta_1) / \gamma_{M5}$	<b>Chord face failure shear <math>F_z</math></b>	
$UC_{Cff,y}$	$V_{y,Ed,tot} / Pen_{Cff,y}$	$V_{z,Ed}$	Input ( $V_{z,Ed}$ )
<b>Chord face failure shear <math>F_z</math></b>		$Pen_{Cff,z}$	$1.7 \cdot (k_p \cdot f_{y0} \cdot t_0 \cdot d_1 \cdot d_0) / (L_1 \cdot \sin\theta_1) / \gamma_{M5}$
$V_{z,Ed,1}$	Input ( $V_{z,Ed}$ )	$UC_{Cff,z}$	$V_{z,Ed} / Pen_{Cff,z}$
$V_{z,Ed,2}$	$F_{x,Ed} \cdot e_z / e_x$	<b>Chord bending moment <math>M_x</math> (torsional moment brace)</b>	
$V_{z,Ed,tot}$	$V_{z,Ed,1} + V_{z,Ed,2}$	$T_{Ed}$	Input ( $M_x$ )
$Pen_{Cff,z}$	$1.7 \cdot (k_p \cdot f_{y0} \cdot t_0 \cdot d_1 \cdot d_0) / (L_1 \cdot \sin\theta_1) / \gamma_{M5}$	$M_{pl}$	$W_{pl} \cdot f_{y0}$
$UC_{Cff,z}$	$V_{z,Ed,tot} / Pen_{Cff,z}$	$UC_{Cbm,x}$	$T_{Ed} / M_{pl}$
<b>Chord bending moment (torsional moment brace)</b>		<b>Chord bending moment <math>M_z</math> (<math>F_x \cdot e_y</math>)</b>	
$T_{Ed}$	Input ( $M_x$ )	$M_{z,Ed}$	$F_{x,Ed} \cdot e_y$
$M_{T,pl,Rd}$	$W_{pl} \cdot f_{y0}$	$M_{pl}$	$W_{pl} \cdot f_{y0}$
$UC_{Cbm}$	$T_{Ed} / M_{T,pl,Rd}$	$UC_{Cbm,z}$	$M_{z,Ed} / M_{pl}$
<b>Combination</b>		<b>Combination</b>	
$UC$	$UC_{Cff,x} + (UC_{Cff,y})^2 + UC_{Cff,z} + UC_{Cbm,x}$	$UC$	$UC_{Cff,x} + (UC_{Cff,y})^2 + UC_{Cff,z} + UC_{Cbm,x} + (UC_{Cbm,z})^2 + UC_{Ctm,y}$
$UC_{joint\ failures}$		$UC_{joint\ failures}$	

From the breasting dolphin column (chord) and steel arm (brace) of the mooring bollard, a representative FE model has been set up, which is shown in Figure 53 including its simplified mechanical model. In the FE model the design values of the load are applied in a force controlled simulation, on a reference point from which, by means of a constraint, the prescribed loads are transferred to normal forces, shear forces and bending moments on the brace edge.

From the calculation sheet the governing directions of the resultant force  $F_{res}$  are identified and the associated combinations of  $F_x$ ,  $F_y$  and  $F_z$  have been implemented and simulated in Abaqus. Both the FEA and the calculation sheet show that the load combination B3 (see Appendix G.2) is governing and fails on the combination of a torsional moment and shear force that are acting on the brace. With the design rule for C T+S, which is implemented in the calculation sheet, a plastic design resistance of 797.5 kN is found. While comparing to the plastic capacity of 901.5 kN that is obtained with FEA, a deviation of about 13% is observed due to some conservatism in the EC design rule for the combination of a torsional moment and shear.

The UC's for joint failures obtained using either of methods implemented in the calculation sheet, show that joint failures are not governing for this geometrical configuration of a mooring bollard. Calculation method 1 resulted in UC of 0.47 (at the moment the plastic design resistance of 797.5 kN due to C T+S is reached), which is higher than the UC resulting from method 2 with a value of 0.39. This difference in the values of the UC's is possibly due to the additional shear forces that are accounted for when applying calculation method 1.

## 5.7 SUMMARY AND CONCLUSION DESIGN RULES

This section aims to find a suitable design rules for penetrated geometries subjected to single-sided tension & compression ( $F_x$ ), shear in the Y-direction (Chord bending moment) and shear in the Z-direction (chord torsional moment). The results of the parameter study are used to create the new design rules. Additionally, some additional parameter configurations have been simulated for geometries subjected to shear  $F_y$  and shear  $F_z$ , as well. The plastic capacity observed in FEA and the geometrical parameters that have influence on them ( $\beta, 2\gamma, 2\delta$ ) have been evaluated. With the existing EC design rules for non-penetrated joints as a basis, and by curve fitting the influence of the geometrical parameters on the plastic capacity observed in FEA, seven new improved design rules are created for penetrated CHS X-joints failing due to joint failures (chord face failure).

For geometries subjected to single-sided tension, a start had been made on evaluating the results of penetrated geometries and the creation of a design rule. But, since for non-penetrated geometries more parameter configurations were failing in chord face failure, it was straightforward to start with evaluating the performance of the pre-existing EC design rules for non-penetrated joints in order to create a solid basis from which the new design rules for penetrated joints could be built on. It is concluded that both the design rule for non-penetrated X-joints and T-joints subjected to single-sided tension, underestimate the plastic capacity by an average factor of 1.46 or even overpredicts the plastic capacity for certain situations. Therefore, an improved design rule for X-joints is suggested that will lead to significant improvement in the approximation of the true plastic capacity of the non-penetrated CHS joints. This design rule is provided in Equation 5.26 and leads to an average RR of 1.12.

The process of creating a design rule for penetrated CHS X-joints subjected to single-sided tension ( $F_x$ ) is started with the knowledge gained from evaluating the non-penetrated CHS X-joints and their design rules. From the parameter study, it had already been concluded that the plastic capacity of penetrated joints are underestimated significantly by the existing EC design rules for non-penetrated X- and T-joints, as is confirmed by their average RR of 3.32 and 2.45, respectively.

To create a suitable design rule, several steps have been taken which have eventually resulted in two improved versions of the existing design rules, and five alternative design rules. Three of the latter are considered to be a suitable design rule for the determination of the plastic design resistance of penetrated CHS X-joints subjected to single-sided loadings. Two of them are based on the stress pattern observed in FEA and the other one is based on the influences of the parameter factors on the plastic capacity. Although this latter design rule “Result factors”, is easier to interpret and can be deduced more clearly from the applied geometrical parameters, this design rule predicts design resistances that deviate more from the observed plastic capacity and therefore, based on the RR’s, it is proposed to use the design rule “Stress Pattern 2b”, provided in Equation 5.33, for calculating the plastic design resistance of penetrated CHS X-joints subjected to single-sided tension ( $F_x$ ). For this design rule an average, lowest and highest RR of 1.09, 0.94, and 1.34, respectively, are obtained.

To check whether the existing EC design rules for non-penetrated joints and the new design rules for penetrated joints predict the failure mechanism well, a verification of the failure mechanisms and approximated plastic design resistances is done, which is provided in paragraph 5.2.2.2. For the verification of the new design rules for penetrated joints, the design rule “Stress pattern 2b” is included in a set of design rules. It can be seen that by including the new design rule for penetrated joints in the design set, the failure mechanism observed in FEA is also identified more often as the governing failure mechanism according to the set of design rules, as was done while using the existing EC design rules for non-penetrated joints. Furthermore, it is observed that for the geometries failing in chord face failure, the plastic design resistances obtained with the new design rules for penetrated joints deviate significantly less from the plastic capacity obtained with FEA than the resistances of the pre-existing EC design rules did.

As the three above mentioned design rules were created and fitted on the FEA results obtained for joints subjected to single-sided tension, their application to penetrated CHS X-joints subjected to single-sided compression ( $F_x$ ) is verified explicitly. For the calculated parameter configurations, an average, lowest and highest RR is achieved with “stress pattern 2a” of 1.06, 0.97, and 1.15, with “stress pattern 2b” of 1.03, 0.95, and 1.12, respectively, and with “result factors” of 0.97, 0.87, and 1.06, respectively, from which it can be concluded that the two design rules based on the stress patterns are suitable for the approximation of the plastic capacity in single-sided compression as well.

Furthermore, the reduction factor  $k_p$  that is prescribed in the EC for the reduction of the plastic capacity because of the pre-existing compression stresses in the chord member, due to an initial bending moment or compression force, is evaluated for the CHS X-joints subjected to single-sided compression, as it is known to have a significant influence for this load case. It is concluded that applying the  $k_p$  factor, causes the average RR to increase from 1.03 to 1.50, making the design rule unnecessarily conservative. It is therefore decided to still include  $k_p$  in the new design rules for penetrated joints, but set its value to 1.0 for the remaining of this research. Some additional follow-up research is however recommended to identify the importance of  $k_p$ .

Next, CHS X-joints subjected to shear in the Y- and Z-direction are researched, for which the same design principles and steps are applied to arrive at a new suitable design rule. For both load cases, additional simulations are performed to obtain more results based on which the design rule could be created, fitted and calibrated. First the performance of the existing EC design rules for non-penetrated joints is evaluated, for which an average value of RR is found to be 5.6 for shear  $F_y$  and 7.86 for shear  $F_z$ , indicating the design rules to be very conservative. Next, the earlier discussed design rule "Result factors" is fitted on the plastic capacity obtained for joints subjected to either force in Y- or Z-direction. Additionally, the influence of the eccentricity of the shear force with respect to the chord axis is taken into account. Resulting in the design rule for geometries subjected to shear  $F_y$  as provided in Equation 5.36 with an average, lowest and highest RR of 1.05, 1.02, and 1.09, respectively and the design rule for geometries subjected to shear  $F_z$  as provided in Equation 5.37 with an average, lowest and highest RR of 1.04, 1.01 and 1.10, respectively.

Lastly, the applicability of the new design rules for penetrated joints for combined joint failures is analyzed using the combination rule as provided in the EC. First the combination of shear  $F_y$  and shear  $F_z$  is analyzed and lastly a check is performed for the combination of single-sided tension ( $F_x$ ), shear  $F_y$  and shear  $F_z$ . To perform this check, the combination rule from the EC is converted into a combined Resistance Ratio (RR) for which the formula is provided in Equation 5.39. The new design rules for penetrated joints approximate the plastic capacity of joints failing due to a combination of shear  $F_y$  and shear  $F_z$  with an average RR of 1.34, and joints failing due to a combination of single-sided tension ( $F_x$ ), shear  $F_y$  and shear  $F_z$  with an average RR of 1.79. Which means that with the combination of the new design rules for penetrated joints significantly higher design resistances can be obtained, compared to the existing EC design rules for non-penetrated joints and their corresponding RR's of 22.2 and 21.0. While at the same time, the new rule does not lead to an overprediction of the plastic capacity of joints failing in chord face failure under combined loadings, and an average safety of 34 and 79% is maintained on the design resistance.

To create a complete overview of the various design checks to be performed for penetrated CHS X-joints, a calculation sheet has been created that includes all unity checks for the relevant joint, chord and brace failure mechanisms. In the calculation sheet, the design value of the applied force, the geometrical and the material properties of the joint can be filled in, from which the plastic design resistances to basic cross-section failures of the brace and the chord, joint failures single-sided tension ( $F_x$ ), shear  $F_y$ , shear  $F_z$  and a combination of these three joint failures is computed. This is done for 15 different load directions of the design force  $F_{Ed}$ .

The results from the calculation sheet are verified using FEA. For most simulations, corresponding failure mechanisms and plastic design resistances with merely small deviations from the FEA plastic capacity were observed, except for joints for which the shear  $F_z$  was dominating.

It seems that, e.g. the plastic design resistance for the combination of a torsional moment and shear on the chord member, 2190 kN, governs over the design resistance obtained with the new design rule for chord face failure ( $F_z$ ), 3628 kN, while in FEA in fact a plastic capacity of 3575 kN is observed for failure due to this last mechanism. The new penetrated chord face failure design rule for geometries subjected in shear  $F_z$  is thus resulting in the correct plastic design resistance, however, due to conservatism of the combination design rule of a torsional moment and shear, this last failure mechanism is falsely governing according to the calculation sheet. It is evaluated for which parameter configurations subjected to shear  $F_z$ , this issue arises. It seems that for multiple geometries with a relatively large brace compared to their chord, i.e. with  $\beta$  factors of 0.6 and 0.8, the combination of torsional moment and shear becomes governing and the plastic design resistance approximated with the set of

design rules becomes conservative with RR for the simulated geometries up to 1.70. It is concluded that the joint failure design rule for shear  $F_z$  underpredicts the true plastic capacity of these joints while their actual capacity are approximated correctly by the new design rule for penetrated chord face failure. It is therefore stated that this new CFF design rule for penetrated joints subjected to shear  $F_z$  also captures the resistances for failure due to a combination of torsional moment and shear and thus eliminates the existing (too conservative) rule for combined torsional moment and shear.

A case study has been done on the mooring bollard from Witteveen+Bos, for which the calculation sheet has been slightly adjusted to allow for eccentricities of the load application in Y- and Z-direction. The eccentricities cause additional bending and torsional moments, for which no joint failure design rules are readily available. Therefore, two alternative methods are applied to take into account the additional bending and torsional moments for the calculation of the joint failure. In the first method, the bending moments about the Z- and Y-axis are converted to shear forces in the Y- and Z-direction that are added to the shear forces initially acting on the brace. To take into account the torsional moment  $M_x$  on the brace, the unity check for the bending moment resistance of the chord member has been added to the combination rule. For the second method, next to the  $UC_{Cb_m,x}$ , also the unity check's for the resistance to a bending moment about the Z-, and a torsional moment about the Y-axis on the chord member, are included in the combination rule.

From the results of the calculation sheet, it can be concluded that joint failures are not governing for the mooring bollard structure and that the bollard is failing on a combination of a torsional moment and shear. For this load combination, a plastic design resistance of 797.5 kN is found using the calculation sheet, which deviates approximatel 13% from the plastic capacity of 901.5 kN as observed in FEA.

The first method for processing the additional bending moments resulted in a UC of 0.47 (at the moment the plastic design resistance of 797.5 kN due to C T+S is reached), which is higher than the UC resulting from the second processing method, 0.39. This difference in the values of the UC's is possibly due to the additional shear forces that are accounted for when applying calculation method 1.

It has thus been observed that the statement concerning the elimination of the existing (too conservative) rule for combined torsional moment and shear, as outlined in Paragraph 5.6.3, does not hold for penetrated CHS X-joints to which the load is applied with a certain eccentricity with respect to the Y- and/or Z-axis. For these joints, the existing design rule for a combination of a torsional moment and shear could indeed be governing, and the a correct plastic design resistance can be calculated with the design rule, albeit with some conservativeness.

Based on this case study, Witteveen+Bos can be advised to check more directions for application of the design force and, though joint failures may not be governing for the mooring bollard, the new design rules for joint failures of penetrated CHS X-joints could be included in their calculation sheet, to provide some extra insights into the behavior of the structure and to exclude the chance joint failures are governing as failure mechanism. The parameter study showed that this latter may be the case for relatively large brace members with a substantial wall thickness, in combination with chord member with a smaller wall thickness.

To be able to fully use the joint failure checks, additional research into the processing methods of the bending and torsional moments caused by the eccentricities should be performed.



## 6 CONCLUSION & RECOMMENDATION

### 6.1 CONCLUSIONS

In this research, the focus was to gain insight into and predicting the behavior of penetrated CHS X-joints. Analogous to studies into branched plate-structural hollow sections and the behavior of their penetrated equivalents, in this study, the behavior of penetrated CHS X-joints and the behavior of their non-penetrated equivalent, are evaluated and compared. For this purpose a finite element model is created using a python script. The script is imported in the FE software ABAQUS, which is used to perform a geometrical and material non-linear FE analysis. An elastic-plastic material model with linear strain hardening, as provided in EC EN 1993-1-5 is adopted within this research and the Von Mises yield criterion is used to evaluate when the geometry starts yielding and to determine the corresponding plastic capacity.

In the parameter study, the load case,  $\beta$ ,  $2\gamma$ , and  $2\delta$  are varied for penetrated, as well as for non-penetrated, CHS X-joints. Initially, only the boundary values of the geometrical parameters are simulated to identify the critical areas for which joint failures may be governing, and based on these results, additional parameter configurations have been evaluated using FEA. The parameter study is performed for the load cases “Double-sided compression and tension ( $F_x$ )”, “Single-sided compression and tension ( $F_x$ )”, “Bending moment about the Y-axis ( $M_y$ )”, “Bending moment about the Z-axis ( $M_z$ )”, “Shear  $F_y$  (chord bending moment)”, and “Shear  $F_z$  (chord torsional moment)”.

From the parameter study, it can be concluded that for the penetrated geometries subjected to double-sided compression and tension ( $F_x$ ), and bending moment about the Y- ( $M_y$ ) and Z- ( $M_z$ ) axis, the plastic capacity can be approximated with the basic cross-section design rules from the EC. Therefore, no new design rules are required and the existing joint failure design rules for non-penetrated geometries, which are chord face failure and punching shear failure, can be omitted in the calculation of the joint capacity for penetrated geometries. For the penetrated geometries that fail in basic cross-section failure, instead of chord face failure as their non-penetrated equivalents do, a plastic capacity of 1.25 till 35.8, and 1.21 till 12.1 times the plastic capacity of their non-penetrated equivalent is observed, for the load cases double-sided compression & tension ( $F_x$ ) and bending moment about the Y- ( $M_y$ ) & Z- ( $M_z$ ) axis, respectively. Their correct plastic design resistances can be calculated with the already available design rules for basic cross section failures.

However, several geometries with penetrated braces subjected to single-sided compression and tension ( $F_x$ ), shear  $F_y$  (chord bending moment), and shear  $F_z$  (chord torsional moment), fail in chord face failure for which the correct plastic design resistance can not be predicted correctly with existing design rules. Comparing the plastic capacity obtained in FEA from the penetrated geometries that fail in chord face failure, with the calculated design resistances obtained with the existing EC design rules for non-penetrated joints, i.e. evaluating the resistance ratio's (RR), an increase in plastic capacity can be observed for:

- single-sided compression and tension ( $F_x$ ), of 1.69 till 4.97 times the EC plastic design resistance;
- shear  $F_y$  (chord bending moment), of 4.46 till 7.49 times the EC plastic design resistance;
- shear  $F_z$  (chord torsional moment), of 4.68 till 11.9 times the EC plastic design resistance.

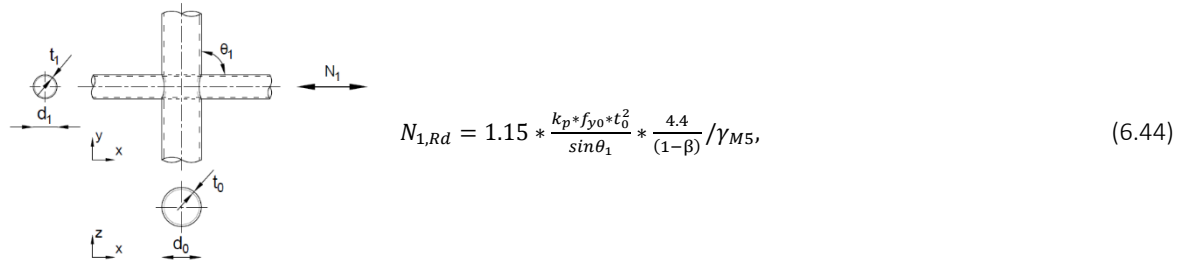
Moreover, for the penetrated geometries that fail in basic cross-section failures under tension & compression ( $F_x$ ), shear  $F_y$  and shear  $F_z$ , an increase of the plastic capacity is observed in FEA by a factor 1.04 till 3.15, 1.30 till 6.30, and 1.09 till 9.81 with respect to their non-penetrated equivalents that fail in chord face failure, respectively. Due to these significant increases in capacity of the penetrated joints with respect to their non-penetrated equivalents and the inaccurate prediction of these capacity by the existing EC design rules, new design rules for penetrated joints that fit the plastic capacity from FEA are recommended for these three load combinations ( $F_x$ ,  $F_y$  and  $F_z$ ).

To create design rules for penetrated joints for these three load combinations, the plastic capacity observed in FEA and the geometrical parameters that have an influence on them ( $\beta$ ,  $2\gamma$ ,  $2\delta$ ) have been evaluated. With the existing EC design rules for non-penetrated joints as a basis, and by curve fitting the influence of the geometrical parameters on the plastic capacity observed in FEA, several improved and new design rules are created.

For the non-penetrated geometries subjected to single-sided tension ( $F_x$ ) that fail in chord face failure, it is concluded that the EC design rules for X- and T-joints, do not approximate their plastic capacity very well. Therefore, an improved X-joint design rule is created, based on curve fitting of the plastic design resistance to the plastic capacity, as given in Table 52 Equation 6.44. This led to an improvement in the approximation of the plastic capacity observed in FEA by the calculated plastic design resistance, as appears from the average RR that has become 1.12 (and was 1.46 for the existing EC design rule for X-joints failing in chord face failure).

Table 52: Improved EC design rules for non-penetrated joints

Improved EC design rule “chord face failure” for non-penetrated joints – single-sided axial load ( $F_x$ )



$$N_{1,Rd} = 1.15 * \frac{k_p * f_{y0} * t_0^2}{\sin \theta_1} * \frac{4.4}{(1 - \beta)} / \gamma_{M5}, \quad (6.44)$$

With the knowledge gained while evaluating the non-penetrated CHS X-joints and their design rules, the process of creating design rules for penetrated CHS X-joints subjected to single-sided tension ( $F_x$ ) is started. The two existing EC design rules for non-penetrated joints are evaluated and two improvements are provided on these design rules. Additionally, 5 alternative design rules are created of which four are based on the stress pattern observed in the FEA results and the last one is based on the influences of the parameter factors on the plastic capacity. From the obtained design rules, “Stress pattern 2b” approximates the FEA plastic capacity best, with an average, lowest and highest RR of 1.09, 0.94, and 1.34, respectively. This design rule can also be used for penetrated CHS X-joints subjected to single-sided compression ( $F_x$ ), resulting in an average RR of 1.06. For both load cases the RR values indicate that the design rule approximates the joint capacity well, and therefore, the design rule “Stress pattern 2b”, as given in Table 53 Equation 6.45, is proposed as the design rule for penetrated CHS X-joints subjected to single-sided compression and tension ( $F_x$ ).

For the design rules of penetrated CHS X-joints subjected to shear in the Y- and Z-direction, the design rule “Result factors” from geometries subjected to single-sided tension ( $F_x$ ) is taken and fitted on the plastic capacity obtained for joints subjected to either a force in Y- or Z-direction. Additionally, the influence of the eccentricity of the shear force with respect to the chord axis is taken into account. With these steps the design rules “Result factors – shear  $F_y$ ”, as given in Equation 6.46, and “Result factors – shear  $F_z$ ”, as given in Equation 6.47, are created. The plastic design resistance obtained with these two design rules approximate the true plastic capacity of the joints accurately, as follows from the average, lowest and highest RR of 1.05, 1.02, and 1.09, for shear  $F_y$ , and 1.04, 1.01 and 1.10, respectively.

Lastly, the applicability of the new design rules for penetrated joints for combined joint failures is analyzed using the combined Resistance Ratio (RR) that is based on the EC combination rule and for which the formula is provided in Equation 5.39. First the performance of the design rules for penetrated joints for a load combination of shear  $F_y$  and shear  $F_z$  is analyzed, which resulted in an average RR of 1.34 in cases for which joint failures were governing. Next to that, the check is performed for the combination of single-sided tension ( $F_x$ ), shear  $F_y$  and shear  $F_z$ , where with the design rules for penetrated joints an average RR of 1.79 is found. From this it follows that the new design rules for penetrated joints can also be applied for calculation the plastic design resistance to joint failures under combined loadings.

A complete overview of the various design checks to be performed for penetrated CHS X-joints has been captured in a calculation sheet that includes all unity checks for the relevant joint, chord and brace failure mechanisms. In this calculation sheet, the plastic design resistances to basic cross-section failures of the brace and the chord, joint failures single-sided tension ( $F_x$ ), shear  $F_y$ , shear  $F_z$  and a combination of these three joint failures is computed for 15 different load directions of a given design force  $F_{Ed}$ .

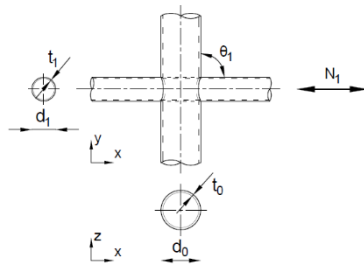


From the sheet and the corresponding FEA is concluded that the new design rules for penetrated joints approximate the plastic capacity well. However, for some geometrical parameter configurations subjected to shear  $F_z$ , the design rule for the combination of a torsional moment and shear is due to its conservatism, incorrectly governing over the joint failures. This issue arises specifically for several geometries with a relatively large brace compared to their chord ( $\beta$  0.6 / 0.8). It is concluded that the C T+S design rule underpredicts the true plastic capacity of these joints for shear  $F_z$ , while their actual capacity are approximated correctly by the new design rule for penetrated chord face failure. It is therefore stated that this new CFF design rule for penetrated joints subjected to shear  $F_z$  also captures the resistances for failure due to a combination of torsional moment and shear and thus eliminates the existing (too conservative) rule for combined torsional moment and shear.

From this graduation research, it is concluded that the pre-existing design rules for joint failures of non-penetrated CHS joints are not suitable for calculation of the design resistance to joint failures of penetrated CHS X-joints. For CHS X-joints subjected to double-sided compression and tension ( $F_x$ ) and bending moment about the Y- ( $M_y$ ) and Z- ( $M_z$ ) axis, the plastic capacity can be approximated well with the current basic cross-section design rules from the EC, however, the EC design rules for joint failures of non-penetrated CHS X-joints should be omitted to approximate the true plastic capacity correctly. For penetrated CHS X-joints subjected to single-sided compression and tension ( $F_x$ ), shear  $F_y$  and shear  $F_z$ , the plastic design resistance to joint failures can be calculated with Equation 6.45, 6.46 and 6.47.

Table 53: Penetrated CHS X-joint design rules

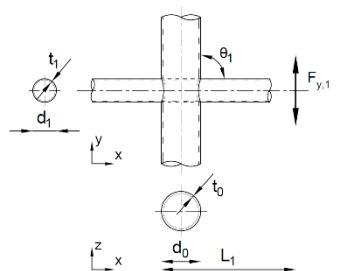
Single-sided axial load ( $F_x$ ) – design rule “stress pattern 2b” for penetrated joints



$$N_{1,Rd} = 1.1 * \frac{k_p * f_{y0} * t_0 * d_1 * f_\delta}{\sin \theta_1} * (\sin(0.65\beta * \pi) - \beta + 0.8) / \gamma_{M5} \quad (6.45)$$

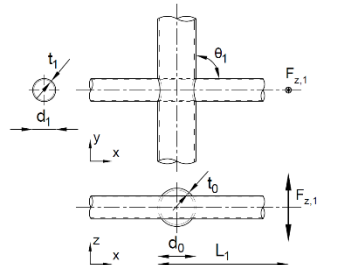
where  $f_\delta = 1 + (50 - 2\delta) / 200$

Shear  $F_y$  (chord bending moment) – design rule “Result factors shear  $F_y$ ” for penetrated joints



$$F_{y,1,Rd} * L_1 = 3 * \frac{k_p * f_{y0} * t_0 * d_1 * d_0}{\sin \theta_1} / \gamma_{M5} \quad (6.46)$$

Shear  $F_z$  (chord torsional moment) – design rule “Result factors shear  $F_z$ ” for penetrated joints



$$F_{z,1,Rd} * L_1 = 1.7 * \frac{k_p * f_{y0} * t_0 * d_1 * d_0}{\sin \theta_1} / \gamma_{M5} \quad (6.47)$$

## 6.2 RECOMMENDATIONS

In this graduation research, a clear and uniform set of design rules that can be used for the calculation of joint failures of penetrated CHS X-joints was aimed for. Although it resulted in three clear new design rules, as presented in the previous paragraph. Several recommendations are done for follow-up research.

To create the new design rules, a parameter study has been carried out for penetrated CHS X-joints subjected to multiple load cases, however no research was conducted into the load case “Bending moment about the X-axis ( $M_x$ )”, and it is recommended to investigate this load case as well.

Next to that, for the load cases bending moment about the Y- and Z-axis, all penetrated geometrical parameter configurations fail in brace bending moment. The plastic capacity related to this failure mechanism can be approximated well with the current EC design rules and therefore, it was concluded that no additional design rules are required for this load case. However, for the prediction of the joint capacity subjected to a combination of loads, the influence of the bending moment needs to be taken into account, which is not possible with the current set of design rules. It is recommended to investigate the possibilities to implement the stresses from bending moments in the various directions within the combination rule of the different load cases. Two processing methods have been proposed for this in the case study to the mooring bollard from Witteveen+Bos.

In both methods, the torsional moment  $M_x$  is accounted for by adding the UC for the bending moment resistance of the chord member to the combination rule. The bending moments about the Z- and Y-axis are in the first method converted to shear forces in the Y- and Z-direction that are added to the shear forces what were already acting on the brace, and for the second method, the UC's from basic cross-section moment resistances (bending and torsional for  $M_z$  and  $M_y$  respectively) are added to the combination rule. A disadvantage of the first method is that, due to the way the bending moments are converted to shear forces, extra shear forces in the Y- and Z-direction are included within the design check. The two proposed methods, therefore, need to be checked and validated, and when they do not satisfy, additional research needs to be performed into the way the stresses resulting from additional bending moments, should be accounted for.

In the design rules presented in Table 53, the factor  $k_p$  is applied, which is prescribed in the EC to reduce the plastic capacity of the CHS joint when the chord member is subjected to compression or a bending moment. It is concluded that applying the  $k_p$  factor, causes the average RR to increase from 1.03 to 1.50, making the design rule unnecessarily conservative. It is therefore decided to include  $k_p$  in the new design rules for penetrated joints, but set its value to 1.0 for the remaining of the research. Additional follow-up research is recommended to identify the importance, verify the formulation and application of the reduction factor  $k_p$ .

Besides, the new design rules for penetrated CHS X-joints need to be evaluated and verified by experimental tests, since the design rules are only calibrated on FEA. Next to that, additional research must confirm whether the design rule can also be applied to other steel strengths, as in this study, only circular hollow sections with steel strength S355 are evaluated. As a follow-up step, the material model could be extended by the integration of damage in the FEA. Damage and crack initiation in regions with peak stresses can then be taken into account for the plastic capacity allowing the failure mechanism to be described in more detail. Also the influence of the weld, which in this study is omitted and is the subject of a separate graduation research, should be evaluated and when needed, taken into account. Obviously, the new design rules should also be further evaluated on, e.g. their reliability and the required safety factors, before they may be included in a public code or guideline.

Furthermore, some issues concerning the EC design rule for the combination of a torsional moment and a shear force, are elaborated in Paragraph 5.7. To conclude, it has been observed that when a combination of loads is imposed directly on the brace the existing rule for combined torsional moment and shear is too conservative and should be omitted (Paragraph 5.6.3), while a combination of loads that is applied to the brace with a certain eccentricity in the Y- and/or Z-axis, this design rule is governing and may therefore certainly not be omitted. Further research into these issues is necessary.

Engineering firms working with penetrated CHS X-joints in mooring bollard structures, are advised to ensure that they include a sufficient amount of directions of the design force in their calculation sheet and, though joint failures may not be governing for the mooring bollard, the new design rules for joint failures of penetrated CHS X-joints could be included as well, to provide some extra insights into the behavior of the structure and to ensure joint failures are not governing for the mooring bollards. The parameter study showed that this latter could be the case for relatively large brace members with a substantial wall thickness, in combination with a chord member with a smaller wall thickness.

In this research, differences have been observed in the behavior of CHS X-joints between penetrated and non-penetrated geometries, and therefore, a new set of design rules for penetrated CHS X-joints is proposed, to ensure the plastic capacity of these joints is no longer underestimated as was the case with the existing EC design rules for non-penetrated joints. Although several recommendations need to be explored in extensive follow-up research, this research may have already laid a good foundation for future guidelines and increased the insight in the behavior of penetrated CHS X-joints significantly.



## 7 REFERENCES

---

- [1] Rijkswaterstaat, "Schade aan remmingwerk bij sluizen van Hansweert. ID485509," Beeldbank, [Online]. Available: [https://beeldbank.rws.nl/MediaObject/Details/Schade\\_aan\\_remmingwerk\\_bij\\_de\\_sluizen\\_van\\_Hansweert\\_485509](https://beeldbank.rws.nl/MediaObject/Details/Schade_aan_remmingwerk_bij_de_sluizen_van_Hansweert_485509). [Accessed 22 01 2021].
- [2] Comité Européen de Normalisation, "Eurocode 3: Design of steel structures - Part 1-8: Design of joints," CEN, Brussels, 2005.
- [3] J. Wardenier, Y. Kurobane, J. Packer, G. van der Vegte and X.-L. Zhao, "Design guide for circular hollow section (CHS) joints under predominantly static loading (2nd ed).," CIDECT, Geneva, 2008.
- [4] N. Koteski and J. A. Packer, "Longitudinal plate and through plate-to-hollow structural section welded connections," *Journal of Structural Engineering*, no. 129(4), pp. 478-486, 2003.
- [5] A. P. Voth and J. A. Packer, "Branch plate-to-circular hollow structural section connections | : Experimental investigation and finite-element modeling," *Journal of Structural Engineering*, no. 138(8), pp. 995-1006, 2012.
- [6] A. P. Voth and J. A. Packer, "Branch plate-to-circular hollow structural section connections. ||: X-type parametric numerical study and design," *Journal of Structural Engineering*, no. 138(8), pp. 1007-1018, 2012.
- [7] A. Voth and J. Packer, "Circular hollow through plate connections," *Ernst & Sohn Verlag für Architektur und technische Wissenschaften GmbH & Co. KG, Berlin*, vol. 9, no. 1, pp. 16-23, 2016.
- [8] J. Wardenier, J. Kurobane, D. Packer, D. Dutta and N. Yeomans, "Design guide for circular hollow section (CHS) joints under predominantly pressure," Comité International pour le Développement, Germany, 1991.
- [9] L. Lu, G. de Winkel, Y. Yu and W. J., "Deformation limit for the ultimate strength of hollow section joints," in *6th International Symposium on Tubular Structures*, Melbourne, Australia, 1994.
- [10] G. J. Vegte and Y. Makino, "Further research on chord length and boundary conditions of CHS T- and X-joints," *Advanced steel construction*, vol. 6, no. 3, pp. 879-890, 2010.
- [11] B.-J. Choi, E.-T. Lee, J.-G. Yang and C.-K. Kang, "Axial Capacity of Circular Hollow Section T-joints using Grade HSB 600 Steel," *International Journal of Steel Structures*, vol. 12, no. 4, pp. 483-494, 2012.
- [12] Comité Européen de Normalisation, "Eurocode 3: Design of steel structures - Part 1-5: Plated structural elements," CEN, Brussels, 2005.
- [13] Dassault Systèmes Simulia Corp., Abaqus/Standard User's Manual, Version 6.14, Providence, RI, USA: Dassault Systèmes Simulia Corp., 2014.
- [14] V. Zamani, "NLgeom off on in Abaqus," Researchgate, 20 October 2017. [Online]. Available: [https://www.researchgate.net/post/NLgeom\\_off\\_on\\_in\\_Abaqus](https://www.researchgate.net/post/NLgeom_off_on_in_Abaqus). [Accessed 25 September 2020].
- [15] X.-L. Zhao, "Deformation limit and ultimate strength of welded T-joints in cold-formed RHS sections," *Elsevier*, no. 53, pp. 149-165, 2000.
- [16] British Standard Institution, "BS EN 10210:2006 Hot finished structural hollow sections of non-alloy and fine grain steels," BSI, Londen, 2006.
- [17] Comité Européen de Normalisation, "Eurocode 3: Design of steel structures - Part 1-1: General rules and rules for buildings," CEN, Brussels, 2005.
- [18] EurocodeApplied, "Eurocode 3 Table of design properties for steel tubes - Circular Hollow Sections (CHS)," EurocodeApplied, 2009. [Online]. Available: <https://eurocodeapplied.com/design/en1993/chs-design-properties>. [Accessed 21 April 2020].
- [19] TGB Staalconstructies, normsubcommissie 351 001 02, "Eurocode 3: Design of steel structures - Part 1-1:2006 Dutch national annex," TGB Staalconstructies, 2016.





## A. PYTHON SCRIPT

The below provided script is created as a basic script for penetrated CHS X-joints subjected to single-sided compression and tension ( $F_x$ ), where for compression a displacement of -100 mm is applied and for tension a displacement of 150 mm. Using 4 for loops, the geometrical parameters are varied between  $\beta = (0.2; 0.4; 0.6; 0.8)$ ,  $2\gamma = (10; 30; 50)$ ,  $2\delta = (10; 30; 50)$ . For the above mentioned load case and geometries, 72 ( $2^4 \cdot 3^3$ ) models are generated that and analysed in Abaqus and the results are plotted in an Excel sheets. For the scripts for the analysis of the non-penetrated geometries as well as the scripts for the other load cases, merely small adaptations have been made. Therefore only the basic script is provided in this appendix.

```

1  # -*- coding: mbcx -*-
2  from part import *
3  from material import *
4  from section import *
5  from assembly import *
6  from step import *
7  from interaction import *
8  from load import *
9  from mesh import *
10 from optimization import *
11 from job import *
12 from sketch import *
13 from visualization import *
14 from connectorBehavior import *
15 import os
16 import sys
17 import csv
18 import odbAccess
19 import math
20 import numpy as np
21 import xlswriter
22
23 def cosd (angle):
24     cosine = math.cos((angle)*math.pi/180)
25     return cosine
26 def sind (angle):
27     sine = math.sin((angle)*math.pi/180)
28     return sine
29
30 session.journalOptions.setValues(replayGeometry=COORDINATE,recoverGeometry=COORDINATE)
31
32 for beta in [0.2, 0.4, 0.6, 0.8]:
33     for gamma in [10.0, 30.0, 50.0]:
34         for delta in [10.0, 30.0, 50.0]:
35             for U1R in [-100, 150]:
36
37                 #parameters
38                 Mesh = 4
39                 Alpha = 12
40                 Beta = beta
41                 Gamma = gamma
42                 Delta = delta
43                 BoundaryCondition = "EncastreBC"
44
45                 d0 = 762.0
46                 t0 = (d0/Gamma)
47                 r0 = (d0-t0)/2
48                 d1 = (d0*Beta)
49                 t1 = (d1/Delta)
50                 r1 = (d1-t1)/2
51                 L0 = (Alpha/2*d0+d1)
52                 L1 = (8*d1+d0)
53
54                 #Directory
55                 VName1=str(int(Beta*10))
56                 VName2=str(int(Gamma))
57                 VName3=str(int(Delta))
58                 VName4=(U1R)
59                 Filename=('Pen_B0'+ '{0}'+ '_G'+ '{1}'+ '_D'+ '{2}'+ '_U'+ '{3}').format(VName1,
60                                     VName2, VName3, VName4)
61                 Loadpath='C:\\Temp\\Simplified model\\2 Pen - Single-sided loaded\\{0}'.
62                     format(Filename)
63                 if not os.path.exists(Loadpath):
64                     os.makedirs(Loadpath)
65                 os.chdir(Loadpath)

```



```

65 #Model
66 myModel=mdb.Model(name='Model-'+'{0}'.format(Filename))
67
68 #GEOMETRY
69 myModel.ConstrainedSketch(name=' profile ', sheetSize=200.0)
70 myModel.sketches[' profile '].CircleByCenterPerimeter(center=(0.0, 0.0),
71 point1=((r0), 0.0))
72 myModel.Part(dimensionality=THREE_D, name='Chord', type=DEFORMABLE_BODY)
73 myModel.parts['Chord'].BaseShellExtrude(depth=(L0), sketch=myModel.
74 sketches[' profile '])
75 myModel.ConstrainedSketch(name=' profile ', sheetSize=200.0)
76 myModel.sketches[' profile '].CircleByCenterPerimeter(center=(0.0, 0.0),
77 point1=((r1), 0.0))
78 myModel.Part(dimensionality=THREE_D, name='Brace', type=DEFORMABLE_BODY)
79 myModel.parts['Brace'].BaseShellExtrude(depth=(L1), sketch=myModel.
80 sketches[' profile '])
81
82 #Assembly
83 myRoot=myModel.rootAssembly
84 myRoot.DatumCsysByDefault(CARTESIAN)
85 myRoot.Instance(dependent=ON, name='Chord-1', part=myModel.parts['Chord'])
86 myRoot.Instance(dependent=ON, name='Brace-1', part=myModel.parts['Brace'])
87
88 #Translation
89 myRoot.rotate(angle=90.0, axisDirection=(-r0, 0.0, 0.0), axisPoint=(r0,
90 0.0, 0.0), instanceList=('Chord-1', ))
91 myRoot.translate(instanceList=('Chord-1', ), vector=(0.0, -(L0/2), 0.0))
92 myRoot.rotate(angle=90.0, axisDirection=(0.0, -L0, 0.0), axisPoint=(0.0,
93 L0, 0.0), instanceList=('Brace-1', ))
94 myRoot.translate(instanceList=('Brace-1', ), vector=((L1/2), 0.0, 0.0))
95
96 #Merge and cut
97 myRoot.InstanceFromBooleanMerge(domain=GEOMETRY, instances=(myRoot.
98 instances['Chord-1'], myRoot.instances['Brace-1']), keepIntersections=
99 ON, name='Joint', originalInstances=SUPPRESS)
100 myPart=myModel.parts['Joint']
101 myPart.RemoveFaces(deleteCells=False, faceList=(myPart.faces.findAt((r0, 0
102 , 0), ), ))
103 myPart.RemoveFaces(deleteCells=False, faceList=(myPart.faces.findAt((-r0,
104 0, 0), ), ))
105
106 #Material
107 myModel.Material(name='Steel')
108 myModel.materials['Steel'].Elastic(table=((210000.0, 0.3), ))
109 myModel.materials['Steel'].Plastic(table=((355.0, 0.0), (490.0, 0.06585),
110 ))
111
112 #Section
113 myModel.HomogeneousShellSection(idealization=NO_IDEALIZATION,
114 integrationRule=SIMPSON, material='Steel', name='Csec', numIntPts=5,
115 poissonDefinition=DEFAULT, preIntegrate=OFF, temperature=GRADIENT,
116 thickness=(t0), thicknessField='', thicknessModulus=None,
117 thicknessType=UNIFORM, useDensity=OFF)
118 myModel.HomogeneousShellSection(idealization=NO_IDEALIZATION,
119 integrationRule=SIMPSON, material='Steel', name='Bsec', numIntPts=5,
120 poissonDefinition=DEFAULT, preIntegrate=OFF, temperature=GRADIENT,
121 thickness=(t1), thicknessField='', thicknessModulus=None,
122 thicknessType=UNIFORM, useDensity=OFF)
123
124 #SectionAssignment
125 myPart.Set(faces=myPart.faces.findAt(((0, 0, r0), ), name='Cset')
126 myPart.SectionAssignment(offset=0.0, offsetField='', offsetType=
127 MIDDLE_SURFACE, region=myPart.sets['Cset'], sectionName='Csec',
128 thicknessAssignment=FROM_SECTION)
129 myPart.Set(faces=myPart.faces.findAt(((0, r1, 0), ), ((r0+r1, r1, 0), ),
130 ((-r0+r1), r1, 0), ), name='Bset')
131 myPart.SectionAssignment(offset=0.0, offsetField='', offsetType=
132 MIDDLE_SURFACE, region=myPart.sets['Bset'], sectionName='Bsec',
133 thicknessAssignment=FROM_SECTION)
134
135 #Planes
136 myPart.DatumAxisByPrincipalAxis(principalAxis=XAXIS) #6
137 myPart.DatumAxisByPrincipalAxis(principalAxis=YAXIS) #7
138 myPart.DatumAxisByPrincipalAxis(principalAxis=ZAXIS) #8
139
140 myPart.DatumPlaneByPrincipalPlane(offset=0.0, principalPlane=XYPLANE) #9

```

```

117 myPart.DatumPlaneByPrincipalPlane(offset=0.0, principalPlane=YZPLANE) #10
118 myPart.DatumPlaneByPrincipalPlane(offset=0.0, principalPlane=XZPLANE) #11
119
120 # Offset XZ and XY
121 C_off1 = (r0*2*math.pi/4)
122 C_off3 = (r1+5*r0)
123 C_off2 = (C_off1+C_off3)/2
124 B_off0 = (r0-(1.8-Beta)*r1)
125 B_off1 = (r0+1.5*(1.8-Beta)*r1)
126 B_off3 = (r0+5*r1)
127 B_off2 = (B_off1+B_off3)/2
128
129 #XZ
130 myPart.DatumPlaneByPrincipalPlane(offset=C_off1, principalPlane=XZPLANE)
131 #12
132 myPart.DatumPlaneByPrincipalPlane(offset=C_off2, principalPlane=XZPLANE)
133 #13
134 myPart.DatumPlaneByPrincipalPlane(offset=C_off3, principalPlane=XZPLANE)
135 #14
136 myPart.DatumPlaneByPrincipalPlane(offset=-C_off1, principalPlane=XZPLANE)
137 #15
138 myPart.DatumPlaneByPrincipalPlane(offset=-C_off2, principalPlane=XZPLANE)
139 #16
140 myPart.DatumPlaneByPrincipalPlane(offset=-C_off3, principalPlane=XZPLANE)
141 #17
142
143 #YZ
144 myPart.DatumPlaneByPrincipalPlane(offset=B_off0, principalPlane=YZPLANE)
145 #18
146 myPart.DatumPlaneByPrincipalPlane(offset=B_off1, principalPlane=YZPLANE)
147 #19
148 myPart.DatumPlaneByPrincipalPlane(offset=B_off2, principalPlane=YZPLANE)
149 #20
150 myPart.DatumPlaneByPrincipalPlane(offset=B_off3, principalPlane=YZPLANE)
151 #21
152 myPart.DatumPlaneByPrincipalPlane(offset=-B_off0, principalPlane=YZPLANE)
153 #22
154 myPart.DatumPlaneByPrincipalPlane(offset=-B_off1, principalPlane=YZPLANE)
155 #23
156 myPart.DatumPlaneByPrincipalPlane(offset=-B_off2, principalPlane=YZPLANE)
157 #24
158 myPart.DatumPlaneByPrincipalPlane(offset=-B_off3, principalPlane=YZPLANE)
159 #25
160
161 #rotation X
162 myPart.DatumPlaneByRotation(angle=45, axis=myPart.datums[6], plane=myPart.
163 datums[11]) #26
164 myPart.DatumPlaneByRotation(angle=-45, axis=myPart.datums[6], plane=myPart
165 .datums[11]) #27
166
167 #PartitionFaceByDatumPlane
168 #XZ
169 myPart.PartitionFaceByDatumPlane(datumPlane=myPart.datums[14], faces=
170 myPart.faces.findAt(((0, 0, (r0)), )))
171 myPart.PartitionFaceByDatumPlane(datumPlane=myPart.datums[13], faces=
172 myPart.faces.findAt(((0, 0, (r0)), )))
173 myPart.PartitionFaceByDatumPlane(datumPlane=myPart.datums[12], faces=
174 myPart.faces.findAt(((0, 0, (r0)), )))
175 myPart.PartitionFaceByDatumPlane(datumPlane=myPart.datums[17], faces=
176 myPart.faces.findAt(((0, 0, (r0)), )))
177 myPart.PartitionFaceByDatumPlane(datumPlane=myPart.datums[16], faces=
178 myPart.faces.findAt(((0, 0, (r0)), )))
179 myPart.PartitionFaceByDatumPlane(datumPlane=myPart.datums[15], faces=
180 myPart.faces.findAt(((0, 0, (r0)), )))
181
182 #YZ
183 myPart.PartitionFaceByDatumPlane(datumPlane=myPart.datums[21], faces=
184 myPart.faces.findAt(((r0), 0, (r1)), )))
185 myPart.PartitionFaceByDatumPlane(datumPlane=myPart.datums[20], faces=
186 myPart.faces.findAt(((r0), 0, (r1)), )))
187 myPart.PartitionFaceByDatumPlane(datumPlane=myPart.datums[19], faces=

```

```

163
164 myPart.faces.findAt(((r0), 0, (r1)), ))
165 myPart.PartitionFaceByDatumPlane(datumPlane=myPart.datums[25], faces=
166 myPart.faces.findAt(((r0), 0, (r1)), ))
167 myPart.PartitionFaceByDatumPlane(datumPlane=myPart.datums[24], faces=
168 myPart.faces.findAt(((r0), 0, (r1)), ))
169 myPart.PartitionFaceByDatumPlane(datumPlane=myPart.datums[23], faces=
170 myPart.faces.findAt(((r0), 0, (r1)), ))
171 myPart.PartitionFaceByDatumPlane(datumPlane=myPart.datums[18], faces=
172 myPart.faces.findAt(((0, 0, (r1)), ))
173 myPart.PartitionFaceByDatumPlane(datumPlane=myPart.datums[22], faces=
174 myPart.faces.findAt(((0, 0, (r1)), ))
175
176 #XZ chord
177 myPart.PartitionFaceByDatumPlane(datumPlane=myPart.datums[11], faces=
178 myPart.faces.findAt(((0, 0, r0), ), ((0, 0, -r0), ), ))
179
180 #XY chord
181 Cpart = [C_off3+10, C_off3-10, C_off1+10, C_off1-10, -(C_off3+10), -(
182 C_off3-10), -(C_off1+10), -(C_off1-10)]
183 for yy in Cpart:
184 Facepoint = (0, yy, r0)
185 myPart.PartitionFaceByDatumPlane(datumPlane=myPart.datums[9], faces=
186 myPart.faces.findAt(((Facepoint), ), ))
187
188 #YZ chord
189 for yy in Cpart:
190 for i in [1, -1]:
191 Facepoint = (0, yy, i*r0)
192 myPart.PartitionFaceByDatumPlane(datumPlane=myPart.datums[10],
193 faces=myPart.faces.findAt(((Facepoint), ), ))
194
195 #XY brace
196 Bpart = [B_off3+10, B_off3-10, B_off1+10, B_off1-10, B_off0+10, 0, -(
197 B_off3+10), -(B_off3-10), -(B_off1+10), -(B_off1-10), -(B_off0+10)]
198 for xx in Bpart:
199 Facepoint = (xx, 0, r1)
200 myPart.PartitionFaceByDatumPlane(datumPlane=myPart.datums[9], faces=
201 myPart.faces.findAt(((Facepoint), ), ))
202
203 #XZ brace
204 for xx in Bpart:
205 for i in [1, -1]:
206 Facepoint = (xx, 0, i*r1)
207 myPart.PartitionFaceByDatumPlane(datumPlane=myPart.datums[11],
208 faces=myPart.faces.findAt(((Facepoint), ), ))
209
210 #Diagonals brace
211 for xx in Bpart:
212 for angle in [135,315]:
213 Facepoint = (xx, cosd(angle)*r1, sind(angle)*r1)
214 myPart.PartitionFaceByDatumPlane(datumPlane=myPart.datums[26],
215 faces=myPart.faces.findAt(((Facepoint), ), ))
216 for angle in [45,225]:
217 Facepoint = (xx, cosd(angle)*r1, sind(angle)*r1)
218 myPart.PartitionFaceByDatumPlane(datumPlane=myPart.datums[27],
219 faces=myPart.faces.findAt(((Facepoint), ), ))
220
221 #Partition diagonals
222 for yy in [(sind(45)*r1), -(sind(45)*r1)]:
223 for a in [(45,90), (135,90), (225,270), (315,270)]:
224 p_1 = ((math.copysign(1,cosd(a[0]))*(math.sqrt((r0**2)-((cosd(a[
225 0]))*r1)**2))), yy, (sind(a[0])*r1))
226 Fc_d = (cosd(a[0])*r0, yy, sind(a[0])*r0)
227 p_2 = (0, math.copysign(C_off1,yy), sind(a[1])*r0)
228 myPart.PartitionFaceByShortestPath(faces=myPart.faces.findAt((Fc_d
229 ), ), point1=myPart.vertices.findAt((p_1), ), point2=myPart.
230 vertices.findAt((p_2), ))
231
232 #mesh
233 #Set Element type and mesh region
234 Faces_T = myPart.faces.getByBoundingBox(-L1/2, -L0/2, -r0, L1/2, L0/2, r0)

```

```

217     Faces_QUAD = myPart.faces.getByBoundingBox(-B_off1, -C_off1, -r0, B_off1,
218           C_off1, r0)
219     myPart.setElementType(elemTypes=(ElemType(elemCode=S8R, elemLibrary=
220           STANDARD), ElemType(elemCode=STRI65, elemLibrary=STANDARD)), regions
221           =(((Faces_QUAD), ), ))
222     myPart.setMeshControls(elemShape=QUAD_DOMINATED, regions=(Faces_T),
223           technique=STRUCTURED)
224     myPart.setMeshControls(elemShape=QUAD, regions=(Faces_QUAD), technique=
225           STRUCTURED)
226
227     #Seed edges
228     C_parts = 4
229     B_parts = 8
230
231     #Fine mesh
232     myPart.seedEdgeByNumber(constraint=FINER, edges=(myRoot.instances[
233           'Joint-1'].edges.getByBoundingBox(-(B_off1+10), -(C_off1+10), -(r0+10)
234           ), (B_off1+10), C_off1+10, (r0+10))), number=int(3.0*Mesh))
235
236     for yy in [(10, C_off1+10), (-(C_off1+10), -10)]:
237         for zz in [(10, r0+10), (-(r0+10), -10)]:
238             myPart.seedEdgeByNumber(constraint=FINER, edges=(myRoot.instances[
239                   'Joint-1'].edges.getByBoundingBox(-r0, yy[0], zz[0], r0, yy[1]
240                   ), zz[1])), number=int(2.5*Mesh+1.6/Beta))
241
242     for yy in [C_off1-10, -(C_off1-10)]:
243         for i in range(0, 180):
244             Edgepoint = (cosd(i)*r0, yy, sind(i)*r0)
245             myPart.seedEdgeByNumber(constraint=FINER, edges=myPart.edges.
246                   findAt(((Edgepoint), ), ), number=int(2.5*Mesh+1.6/Beta))
247
248     for ya in [85, 95, 265, 275]:
249         for i in range(C_parts):
250             Edgepoint = (cosd(ya)*r0, 0, sind(ya)*r0)
251             myPart.seedEdgeByNumber(constraint=FINER, edges=myPart.edges.
252                   findAt(((Edgepoint), ), ), number=int(2.5*Mesh+1.6/Beta))
253
254     for xx in [B_off0+10, -(B_off0+10)]:
255         for i in range(B_parts):
256             Edgepoint = (xx, sind(i*45.0)*r1, cosd(i*45.0)*r1)
257             myPart.seedEdgeByNumber(constraint=FINER, edges=myPart.edges.
258                   findAt(((Edgepoint), ), ), number=int(1.5*Mesh))
259
260     #Coarse mesh
261     for yy in [C_off3, L0/2, -C_off3, -L0/2]:
262         for i in range(C_parts):
263             Edgepoint = (cosd(i*90.0+45)*r0, yy, sind(i*90.0+45)*r0)
264             myPart.seedEdgeByNumber(constraint=FINER, edges=myPart.edges.
265                   findAt(((Edgepoint), ), ), number=2*Mesh)
266
267     for xx in [B_off3, L1/2, -B_off3, -L1/2]:
268         for i in range(B_parts):
269             Edgepoint = (xx, sind(i*45.0+22.5)*r1, cosd(i*45.0+22.5)*r1)
270             myPart.seedEdgeByNumber(constraint=FINER, edges=myPart.edges.
271                   findAt(((Edgepoint), ), ), number=1*Mesh)
272
273     for yy in [C_off3+10, -(C_off3+10)]:
274         for i in range(C_parts):
275             Edgepoint = (cosd(i*90.0)*r0, yy, sind(i*90.0)*r0)
276             myPart.seedEdgeByNumber(constraint=FINER, edges=myPart.edges.
277                   findAt(((Edgepoint), ), ), number=(Alpha/8*Mesh))
278
279     for xx in [B_off3+10, -(B_off3+10)]:
280         for i in range(B_parts):
281             Edgepoint = (xx, sind(i*45.0)*r1, cosd(i*45.0)*r1)
282             myPart.seedEdgeByNumber(constraint=FINER, edges=myPart.edges.
283                   findAt(((Edgepoint), ), ), number=int(1.5*Mesh))
284
285     #Coarse/fine mesh
286     for yy in [C_off2-10, -(C_off2-10)]:
287         for i in range(C_parts):
288             Edgepoint = (cosd(i*90.0)*r0, yy, sind(i*90.0)*r0)
289             myPart.seedEdgeByNumber(constraint=FINER, edges=myPart.edges.
290                   findAt(((Edgepoint), ), ), number=int(1.5*Mesh))
291
292     for yy in [C_off2+10, -(C_off2+10)]:

```

```

271         for i in range(C_parts):
272             Edgepoint = (cosd(i*90.0)*r0, yy, sind(i*90.0)*r0)
273             myPart.seedEdgeByNumber(constraint=FINER, edges=myPart.edges.
                findAt(((Edgepoint), ), ), number=int(1.0*Mesh))
274     for yy in [C_off2, -C_off2]:
275         for i in range(C_parts):
276             Edgepoint = (cosd(i*90.0+45.0)*r0, yy, sind(i*90.0+45.0)*r0)
277             myPart.seedEdgeByNumber(constraint=FINER, edges=myPart.edges.
                findAt(((Edgepoint), ), ), number=int(2.5*Mesh))
278
279     for i in range(B_parts):
280         Edgepoint = (0, sind(i*45.0)*r1, cosd(i*45.0)*r1)
281         myPart.seedEdgeByNumber(constraint=FINER, edges=myPart.edges.findAt(((
            Edgepoint), ), ), number=int(1.6/Beta))
282
283     for xx in [B_off2-10, -(B_off2-10)]:
284         for i in range(B_parts):
285             Edgepoint = (xx, sind(i*45.0)*r1, cosd(i*45.0)*r1)
286             myPart.seedEdgeByNumber(constraint=FINER, edges=myPart.edges.
                findAt(((Edgepoint), ), ), number=int(1.5*Mesh))
287     for xx in [B_off2+10, -(B_off2+10)]:
288         for i in range(B_parts):
289             Edgepoint = (xx, sind(i*45.0)*r1, cosd(i*45.0)*r1)
290             myPart.seedEdgeByNumber(constraint=FINER, edges=myPart.edges.
                findAt(((Edgepoint), ), ), number=int(1.0*Mesh))
291     for xx in [B_off2, -B_off2]:
292         for i in range(B_parts):
293             Edgepoint = (xx, sind(i*45.0+22.5)*r1, cosd(i*45.0+22.5)*r1)
294             myPart.seedEdgeByNumber(constraint=FINER, edges=myPart.edges.
                findAt(((Edgepoint), ), ), number=int(2.0*Mesh))
295
296     myPart.generateMesh()
297
298     #Steps
299     myModel.StaticStep(initialInc=0.001, maxInc=0.015, maxNumInc=200, name=
        'Static, General', nlgeom=ON, previous='Initial')
300
301     #Boundary conditions and loads
302     #Loads
303     myRoot.ReferencePoint(point=(L1/2, 0.0, 0.0)) #8
304     myRoot.Set(name='B_RefR', referencePoints=(myRoot.referencePoints[8], ))
305     myRoot.Set(edges=myRoot.instances['Joint-1'].edges.getByBoundingBox(L1/2,
        -L0/2, -r0, L1/2, L0/2, r0), name='B_edgesR')
306     myModel.EquallySpacedAmplitude(begin=0.0, data=(0.0, 1.0), fixedInterval=
        1.0, name='Amp-1', smooth=SOLVER_DEFAULT, timeSpan=STEP)
307     myModel.RigidBody(name='Constraint-B1', refPointRegion=myRoot.sets[
        'B_RefR'], tieRegion=myRoot.sets['B_edgesR'])
308     myModel.DisplacementBC(amplitude='Amp-1', createStepName='Static, General'
        , distributionType=UNIFORM, fieldName='', fixed=OFF, localCsys=None,
        name='BC_LoadR', region=myRoot.sets['B_RefR'], u1=U1R, u2=UNSET, u3=
        UNSET, ur1=UNSET, ur2=UNSET, ur3=UNSET)
309
310     #Bounday condition
311     myRoot.ReferencePoint(point=(0.0, L0/2, 0.0)) #11 #14
312     myRoot.Set(name='C_RefT', referencePoints=(myRoot.referencePoints[11], ))
313     myRoot.Set(edges=myRoot.instances['Joint-1'].edges.getByBoundingBox(-L1/2,
        L0/2, -r0, L1/2, L0/2, r0), name='C_edgesT')
314     myModel.RigidBody(name='Constraint-C1', refPointRegion=myRoot.sets[
        'C_RefT'], tieRegion=myRoot.sets['C_edgesT'])
315
316     myRoot.ReferencePoint(point=(0.0, -(L0/2), 0.0)) #14 #17
317     myRoot.Set(name='C_RefB', referencePoints=(myRoot.referencePoints[14], ))
318     myRoot.Set(edges=myRoot.instances['Joint-1'].edges.getByBoundingBox(-L1/2,
        -L0/2, -r0, L1/2, -L0/2, r0), name='C_edgesB')
319     myModel.RigidBody(name='Constraint-C2', refPointRegion=myRoot.sets[
        'C_RefB'], tieRegion=myRoot.sets['C_edgesB'])
320
321     if BoundaryCondition == 'PinnedBC':
322         myModel.PinnedBC(createStepName='Static, General', localCsys=None,
            name='BC_BCT', region=myRoot.sets['C_RefT'])
323         myModel.PinnedBC(createStepName='Static, General', localCsys=None,

```

```

324         name='BC_BCB', region=myRoot.sets['C_RefB'])
325     elif BoundaryCondition == 'XsymmBC':
326         myModel.XsymmBC(createStepName='Static, General', localCsys=None, name
327             ='BC_BCT', region=myRoot.sets['C_RefT'])
328         myModel.XsymmBC(createStepName='Static, General', localCsys=None, name
329             ='BC_BCB', region=myRoot.sets['C_RefB'])
330     elif BoundaryCondition == 'EncastreBC':
331         myModel.EncastreBC(createStepName='Static, General', localCsys=None,
332             name='BC_BCT', region=myRoot.sets['C_RefT'])
333         myModel.EncastreBC(createStepName='Static, General', localCsys=None,
334             name='BC_BCB', region=myRoot.sets['C_RefB'])
335
336     #HistoryOutput and FieldOutput
337     myRoot.Set(name='Node_X11', vertices=myRoot.instances['Joint-1'].vertices.
338         findAt(((r0, C_off1, 0.0), )))
339     myRoot.Set(name='Node_X12', vertices=myRoot.instances['Joint-1'].vertices.
340         findAt(((r0, C_off1, 0.0), )))
341     myRoot.Set(name='Node_X21', vertices=myRoot.instances['Joint-1'].vertices.
342         findAt(((r0, -C_off1, 0.0), )))
343     myRoot.Set(name='Node_X22', vertices=myRoot.instances['Joint-1'].vertices.
344         findAt(((r0, -C_off1, 0.0), )))
345     myRoot.Set(name='Node_Z01', vertices=myRoot.instances['Joint-1'].vertices.
346         findAt(((0.0, 0.0, r0), )))
347     myRoot.Set(name='Node_Z02', vertices=myRoot.instances['Joint-1'].vertices.
348         findAt(((0.0, 0.0, -r0), )))
349     myRoot.Set(name='Node_Z11', vertices=myRoot.instances['Joint-1'].vertices.
350         findAt(((0.0, C_off1, r0), )))
351     myRoot.Set(name='Node_Z12', vertices=myRoot.instances['Joint-1'].vertices.
352         findAt(((0.0, C_off1, -r0), )))
353     myRoot.Set(name='Node_Z21', vertices=myRoot.instances['Joint-1'].vertices.
354         findAt(((0.0, -C_off1, r0), )))
355     myRoot.Set(name='Node_Z22', vertices=myRoot.instances['Joint-1'].vertices.
356         findAt(((0.0, -C_off1, -r0), )))
357
358     del myModel.historyOutputRequests['H-Output-1']
359     myModel.HistoryOutputRequest(createStepName='Static, General', name=
360         'H-Output-BCR', rebar=EXCLUDE, region=myRoot.sets['B_RefR'],
361         sectionPoints=DEFAULT, variables=('RF1', 'U1', ))
362     myModel.HistoryOutputRequest(createStepName='Static, General', name=
363         'H-Output-Ux11', rebar=EXCLUDE, region=myRoot.sets['Node_X11'],
364         sectionPoints=DEFAULT, variables=('U1', ))
365     myModel.HistoryOutputRequest(createStepName='Static, General', name=
366         'H-Output-Ux12', rebar=EXCLUDE, region=myRoot.sets['Node_X12'],
367         sectionPoints=DEFAULT, variables=('U1', ))
368     myModel.HistoryOutputRequest(createStepName='Static, General', name=
369         'H-Output-Ux21', rebar=EXCLUDE, region=myRoot.sets['Node_X21'],
370         sectionPoints=DEFAULT, variables=('U1', ))
371     myModel.HistoryOutputRequest(createStepName='Static, General', name=
372         'H-Output-Ux22', rebar=EXCLUDE, region=myRoot.sets['Node_X22'],
373         sectionPoints=DEFAULT, variables=('U1', ))
374     myModel.HistoryOutputRequest(createStepName='Static, General', name=
375         'H-Output-Uz01', rebar=EXCLUDE, region=myRoot.sets['Node_Z01'],
376         sectionPoints=DEFAULT, variables=('U3', ))
377     myModel.HistoryOutputRequest(createStepName='Static, General', name=
378         'H-Output-Uz02', rebar=EXCLUDE, region=myRoot.sets['Node_Z02'],
379         sectionPoints=DEFAULT, variables=('U3', ))
380     myModel.HistoryOutputRequest(createStepName='Static, General', name=
381         'H-Output-Uz11', rebar=EXCLUDE, region=myRoot.sets['Node_Z11'],
382         sectionPoints=DEFAULT, variables=('U3', ))
383     myModel.HistoryOutputRequest(createStepName='Static, General', name=
384         'H-Output-Uz12', rebar=EXCLUDE, region=myRoot.sets['Node_Z12'],
385         sectionPoints=DEFAULT, variables=('U3', ))
386     myModel.HistoryOutputRequest(createStepName='Static, General', name=
387         'H-Output-Uz21', rebar=EXCLUDE, region=myRoot.sets['Node_Z21'],
388         sectionPoints=DEFAULT, variables=('U3', ))
389     myModel.HistoryOutputRequest(createStepName='Static, General', name=
390         'H-Output-Uz22', rebar=EXCLUDE, region=myRoot.sets['Node_Z22'],
391         sectionPoints=DEFAULT, variables=('U3', ))
392     myModel.HistoryOutputRequest(createStepName='Static, General', name=
393         'H-Output-ALLPD', variables=('ALLPD', ))
394     myModel.fieldOutputRequests['F-Output-1'].setValues(variables=('S', 'E',

```

```

357         'PE', 'PEEQ', 'EE', 'U'))
358
359 #job
360 mdb.Job(atTime=None, contactPrint=OFF, description='', echoPrint=OFF,
361         explicitPrecision=SINGLE, getMemoryFromAnalysis=True, historyPrint=OFF
362         , memory=90, memoryUnits=PERCENTAGE, model='Model-'+'{0}'.format(
363         Filename), modelPrint=OFF, multiprocessingMode=DEFAULT, name='Job-'+
364         '{0}'.format(Filename), nodalOutputPrecision=SINGLE, numCpus=1,
365         numGPUs=0, queue=None, resultsFormat=ODB, scratch='', type=ANALYSIS,
366         userSubroutine='', waitHours=0, waitMinutes=0)
367 mdb.jobs['Job-'+'{0}'.format(Filename)].submit(consistencyChecking=OFF)
368 mdb.jobs['Job-'+'{0}'.format(Filename)].waitForCompletion()
369
370 #Create ODB output
371 RF1, U1 = ([ for i in range (2)
372
373 Directory_odb = '{0}'.format(Loadpath)+'/'+'Job-'+'{0}'.format(Filename)+
374         '.odb'
375 open_odb = session.openOdb(name=Directory_odb)
376 odb = session.odbs[Directory_odb]
377 session.viewports['Viewport: 1'].setValues(displayedObject=open_odb)
378 frames = open_odb.steps['Static, General'].frames
379 numFrames = len(frames)
380
381 #Reaction Force
382 xy_rf = session.XYDataFromHistory(name='XY-RF1', odb=odb,
383         outputVariableName='Reaction force: RF1 PI: rootAssembly Node 1 in
384         NSET B_REFR', steps=('Static, General', ), )
385 RF1 = [abs(x[1]*10**(-3)) for x in xy_rf]
386 Max_RF1 = max(RF1)
387
388 #Displacement
389 xy_u = session.XYDataFromHistory(name='XY_U', odb=odb, outputVariableName=
390         'Spatial displacement: U1 PI: rootAssembly Node 1 in NSET B_REFR',
391         steps=('Static, General', ), )
392 U1 = [abs(x[1]) for x in xy_u]
393
394 #First Yield load
395 xy_allpd = session.XYDataFromHistory(name='XY-ALLPD', odb=odb,
396         outputVariableName='Plastic dissipation: ALLPD for Whole Model', steps
397         =('Static, General', ), )
398 Pl_diss = [x[1]*10**(-3) for x in xy_allpd]
399
400 #Deformation limit
401 xy_ux11 = session.XYDataFromHistory(name='XY-UX11', odb=odb,
402         outputVariableName='Spatial displacement: U1 PI: JOINT-1 Node 17 in
403         NSET NODE_X11', steps=('Static, General', ), )
404 xy_ux12 = session.XYDataFromHistory(name='XY-UX12', odb=odb,
405         outputVariableName='Spatial displacement: U1 PI: JOINT-1 Node 23 in
406         NSET NODE_X12', steps=('Static, General', ), )
407 xy_ux21 = session.XYDataFromHistory(name='XY-UX21', odb=odb,
408         outputVariableName='Spatial displacement: U1 PI: JOINT-1 Node 13 in
409         NSET NODE_X21', steps=('Static, General', ), )
410 xy_ux22 = session.XYDataFromHistory(name='XY-UX22', odb=odb,
411         outputVariableName='Spatial displacement: U1 PI: JOINT-1 Node 6 in
412         NSET NODE_X22', steps=('Static, General', ), )
413 xy_uz01 = session.XYDataFromHistory(name='XY-UZ01', odb=odb,
414         outputVariableName='Spatial displacement: U3 PI: JOINT-1 Node 10 in
415         NSET NODE_Z01', steps=('Static, General', ), )
416 xy_uz02 = session.XYDataFromHistory(name='XY-UZ02', odb=odb,
417         outputVariableName='Spatial displacement: U3 PI: JOINT-1 Node 3 in
418         NSET NODE_Z02', steps=('Static, General', ), )
419 xy_uz11 = session.XYDataFromHistory(name='XY-UZ11', odb=odb,
420         outputVariableName='Spatial displacement: U3 PI: JOINT-1 Node 22 in
421         NSET NODE_Z11', steps=('Static, General', ), )
422 xy_uz12 = session.XYDataFromHistory(name='XY-UZ12', odb=odb,
423         outputVariableName='Spatial displacement: U3 PI: JOINT-1 Node 16 in
424         NSET NODE_Z12', steps=('Static, General', ), )
425 xy_uz21 = session.XYDataFromHistory(name='XY-UZ21', odb=odb,
426         outputVariableName='Spatial displacement: U3 PI: JOINT-1 Node 9 in
427         NSET NODE_Z21', steps=('Static, General', ), )

```

```

396     xy_uz22 = session.XYDataFromHistory(name='XY-UZ22', odb=odb,
      outputVariableName='Spatial displacement: U3 PI: JOINT-1 Node 2 in
      NSET NODE_Z22', steps=('Static, General', ), )
397
398     Def_lim_x11 = [x[1] for x in xy_ux11]
399     Def_lim_x12 = [x[1] for x in xy_ux12]
400     Def_lim_x1 = np.zeros(len(Def_lim_x11))
401     for i in range(len(Def_lim_x11)):
402         Def_lim_x1 [i] = abs(Def_lim_x11[i]-Def_lim_x12[i])/d0*100
403
404     Def_lim_x21 = [x[1] for x in xy_ux21]
405     Def_lim_x22 = [x[1] for x in xy_ux22]
406     Def_lim_x2 = np.zeros(len(Def_lim_x21))
407     for i in range(len(Def_lim_x21)):
408         Def_lim_x2 [i] = abs(Def_lim_x21[i]-Def_lim_x22[i])/d0*100
409
410     Def_lim_z01 = [x[1] for x in xy_uz01]
411     Def_lim_z02 = [x[1] for x in xy_uz02]
412     Def_lim_z0 = np.zeros(len(Def_lim_z01))
413     for i in range(len(Def_lim_z01)):
414         Def_lim_z0 [i] = abs(Def_lim_z01[i]-Def_lim_z02[i])/d0*100
415
416     Def_lim_z11 = [x[1] for x in xy_uz11]
417     Def_lim_z12 = [x[1] for x in xy_uz12]
418     Def_lim_z1 = np.zeros(len(Def_lim_z11))
419     for i in range(len(Def_lim_z11)):
420         Def_lim_z1 [i] = abs(Def_lim_z11[i]-Def_lim_z12[i])/d0*100
421
422     Def_lim_z21 = [x[1] for x in xy_uz21]
423     Def_lim_z22 = [x[1] for x in xy_uz22]
424     Def_lim_z2 = np.zeros(len(Def_lim_z21))
425     for i in range(len(Def_lim_z21)):
426         Def_lim_z2 [i] = abs(Def_lim_z21[i]-Def_lim_z22[i])/d0*100
427
428     Def_lim = np.zeros(len(Def_lim_x1))
429     for i in range(len(Def_lim_x11)):
430         Def_lim[i] = max(Def_lim_x1[i], Def_lim_x2[i], Def_lim_z0[i],
      Def_lim_z1[i], Def_lim_z2[i])
431
432     Def_lim_reached = 0
433     Max_RF12 = 'Not reached'
434     for i in range (len(Def_lim)):
435         if Def_lim_reached == 1:
436             break
437         else:
438             if Def_lim[i] > 3.0:
439                 Def_lim_reached = 1
440                 Max_RF12 = RF1[i]
441
442     #CREATE EXCEL VALUES
443     INC=range(0, numFrames)
444
445     workbook = xlswriter.Workbook('{0}.xlsx'.format(Filename))
446     worksheet1 = workbook.add_worksheet('ABAQUSDATA')
447
448     #Write general data
449     bold = workbook.add_format({'bold': 1})
450     headings1 = ['', '{0}'.format(Filename)]
451     headings2 = ['INC', 'U1', 'RF1', 'Pl. diss.', 'Def. Lim.', 'Max RF1', 'Max
      RF12']
452     headings3 = ['(-)', '(mm)', '(kN)', '(-)', '(%)', '(kN)', '(kN)']
453     worksheet1.write_row('A1', headings1, bold)
454     worksheet1.write_row('A2', headings2, bold)
455     worksheet1.write_row('A3', headings3)
456     worksheet1.write_column(3, 0, INC)
457     worksheet1.write_column(3, 1, U1)
458     worksheet1.write_column(3, 2, RF1)
459     worksheet1.write_column(3, 3, Pl_diss)
460     worksheet1.write_column(3, 4, Def_lim)
461     worksheet1.write('F4', Max_RF1)
462     worksheet1.write('G4', Max_RF12)
463
464     workbook.close()

```



## Master's Thesis

DEPARTMENT OF THE BUILT ENVIRONMENT  
MASTER ARCHITECTURE, BUILDING AND PLANNING  
UNIT STRUCTURAL ENGINEERING & DESIGN  
CHAIR OF STEEL STRUCTURES